Rational approaches to the design of magnetocaloric materials

Batashev, I.

DOI
10.4233/uuid:0f2ee7c8-70d2-43b2-93e7-26a328ded3a9

Publication date
2022

Document Version
Final published version

Citation (APA)
Batashev, I. (2022). *Rational approaches to the design of magnetocaloric materials*. [Dissertation (TU Delft), Delft University of Technology]. https://doi.org/10.4233/uuid:0f2ee7c8-70d2-43b2-93e7-26a328ded3a9

RATIONAL APPROACHES TO THE DESIGN OF MAGNETOCALORIC MATERIALS

Ivan Batashev

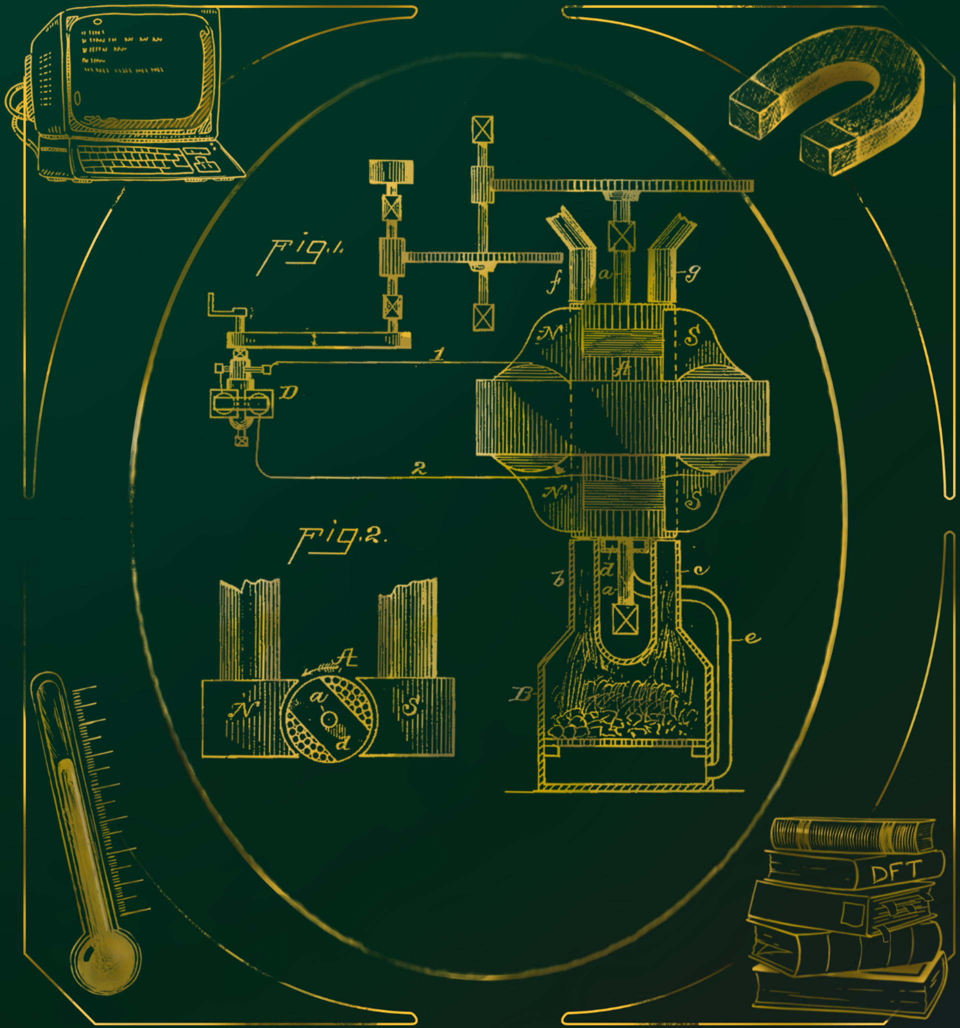

RATIONAL APPROACHES TO THE DESIGN OF MAGNETOCALORIC MATERIALS

Proefschrift

ter verkrijging van de graad van doctor
aan de Technische Universiteit Delft,
op gezag van de Rector Magnificus prof. dr.ir. T.H.J.J. van der Hagen,
voorzitter van het College voor Promoties,
in het openbaar te verdedigen op diensdag 31 mei 2022 om 12:30 uur

door

Ivan BATASHEV

Master in Physics,
Lomonosov Moscow State University, Moscow, Russia,
geboren te Moscow, Rusland.

Dit proefschrift is goedgekeurd door de

promotor: prof. dr. E. Brück
promotor: dr. ir. N.H. van Dijk

Samenstelling promotiecommissie bestaat uit:

Rector Magnificus,	voorzitter
Prof. dr. E.H. Brück	Technische Universiteit Delft, promotor
Dr. ir. N.H. van Dijk	Technische Universiteit Delft, promotor
Onafhankelijke leden:	
Prof. dr. ir. T.J.H. Vlugt	Technische Universiteit Delft
Prof. dr. C. Pappas	Technische Universiteit Delft
Prof. dr. U. Zeitler	Radboud Universiteit
Prof. dr. Y.M. Blanter	Technische Universiteit Delft
Prof. dr. ir. J.L. Kloosterman	Technische Universiteit Delft, reservelid
Overige lid:	
Dr. ir. G.A. de Wijs	Radboud Universiteit

This work originates as part of the research programme of the Foundation for Fundamental Research on Matter (FOM), and falls as of April 1, 2017 under the responsibility of Foundation for Nederlandse Wetenschappelijk Onderzoek Instituten (NWO-I), which is part of the Dutch Research Council (NWO).

Printed by: Print Service Ede

An electronic version of this dissertation is available at
`http://repository.tudelft.nl/`.

"They worked in an Institute that was dedicated above all to the problems of human happiness and the meaning of human life, and even among them, not even one knew exactly what was happiness and what precisely was the meaning of life. So they took it as a working hypothesis that happiness lays in gaining perpetually new insights into the unknown and the meaning of life was to be found in the same process."

— Arkady and Boris Strugatsky,
Monday Begins on Saturday

CONTENTS

1

INTRODUCTION

> *"Once you do know what the question actually is, you'll know what the answer means."*
>
> — Douglas Adams

Refrigeration technologies are extensively used, both for industrial and residential applications. This industry has traditionally been dominated by vapour-compression refrigeration which has seen countless adjustments and improvements since its emergence in the 19th century. Despite being a very mature technology, vapour-compression refrigeration has a fair share of drawbacks. The most prominent of them came to light with the rise of awareness for the energy and environmental impact of current technologies. Global energy demand is on the rise [1] and the number of refrigeration systems in the world is expected to triple in the next 30 years as affordable cooling becomes a global necessity [2]. The limited efficiency of vapour-compression devices in conjunction with the use of environmentally harmful refrigerants such as ozone-depleting substances (chlorofluorocarbons (CFCs)) and greenhouse gases (hydrofluorocarbons (HCFs)) makes their continued use less appealing. The ecological crisis has been addressed by the Montreal Protocol [3], and more recently by the Paris Agreement [4]. These international treaties will limit the use of vapour compression coolers and open a path for modern technologies that could offer a higher energy efficiency and lessen the environmental impact. A possible alternative cooling method that is now being extensively investigated is magnetic refrigeration. Magnetic cooling based on the magnetocaloric effect offers a possibility for eco-friendly, silent, and compact devices. [5–7]

This chapter presents a brief overview of the magnetocaloric effect, its applications, and an introduction to the most promising magnetocaloric material systems.

1.1 MAGNETOCALORIC EFFECT

THE magnetocaloric effect (MCE) can be defined as the thermal response of a magnetic material to a change in an external magnetic field. The MCE is an intrinsic property of all magnetic materials; however, the size of the effect varies for each specific material and with temperature. The origin of the magnetocaloric effect lies in the interplay between the crystal and magnetic lattices of the material. The effect is most pronounced near phase transitions, where the spin system undergoes a reconfiguration. The strength of the MCE can be quantified by the adiabatic temperature change (ΔT_{ad}) and isothermal entropy change (ΔS) for adiabatic and isothermal conditions, respectively. The magnitude of these values depends on the magnetic interactions and is typically enhanced at ferromagnetic to paramagnetic transitions due to the large difference in magnetization of the two phases.

The first reported observation of the MCE was performed by Weiss and Picard who in 1917 recorded a 0.7 K temperature change in nickel under a magnetic field of 1.5 T [8]. In the 1920s the magnetocaloric effect found its application in the field of low-temperature physics after Giauque and Debye independently proposed using the adiabatic demagnetization of paramagnetic salts to reach temperatures below 1 K [9, 10]. Since then, it remains a reliable technique in reaching extremely low temperatures (<2 K). The MCE in paramagnets however decreases with increasing temperature, making the effect unsuitable for any applications at temperatures above 20 K. The next milestone in magnetic refrigeration came in 1997 with the discovery of a giant MCE in the vicinity of room temperature (RT) by Pecharsky and Gschneidner [11]. This renewed the interest in the magnetocaloric effect and led to an extensive investigation of various material families in an attempt to discover efficient and cost-effective candidate materials for magnetic refrigeration near room temperature. This research was aimed both at the improvement of MCE materials and the development of refrigeration devices. The feasibility of such a magnetic refrigerator as a practical home appliance was demonstrated in 2015 when Haier, Astronautics and BASF presented a prototype of a magnetocaloric wine cooler [12]. In addition, the potential for other possible implementations of this effect is being actively investigated. Current applications of the RT magnetocaloric effect include magnetic refrigeration [13], waste heat conversion *via* thermomagnetic motors and thermomagnetic generators [14] and medical uses, such as magnetic hyperthermia for cancer treatment [15].

1.2 APPLICATIONS OF THE MAGNETOCALORIC EFFECT

1.2.1 MAGNETIC REFREGIRATION

MAGNETIC refrigeration (MR) is currently considered to be the primary application for the RT magnetocaloric effect. The refrigeration cycle in such devices is similar to a classic vapour compression cycle, however, the change in pressure is replaced by a change in an external magnetic field as the driving force. The typical configuration of a magnetic cooler consists of a solid-state magnetocaloric material acting as a refrigerant, a permanent magnet to create an external field, hot and cold heat exchangers and a heat transfer medium such as water with antifreeze [16]. A schematic illustration for the magnetic refrigeration cycle is shown in Fig. 1.1. The working principle is based on MCE and can be described as follows. The cycle starts at a temperature just above the magnetic transition in the absence of a magnetic field (top left corner of the diagram). Under adiabatic conditions the working material is magnetized with an external field, this results in an increase of its temperature (top right corner). Next, the heat is removed from the material *via* a heat transfer medium under isofield conditions (bottom right corner). The magnetic field is then switched off adiabatically, this cools down the working material below its initial temperature (bottom left corner). Lastly, cooled refrigerant comes in contact with the heat load and absorbs heat from it heating up and thus completing the cycle.

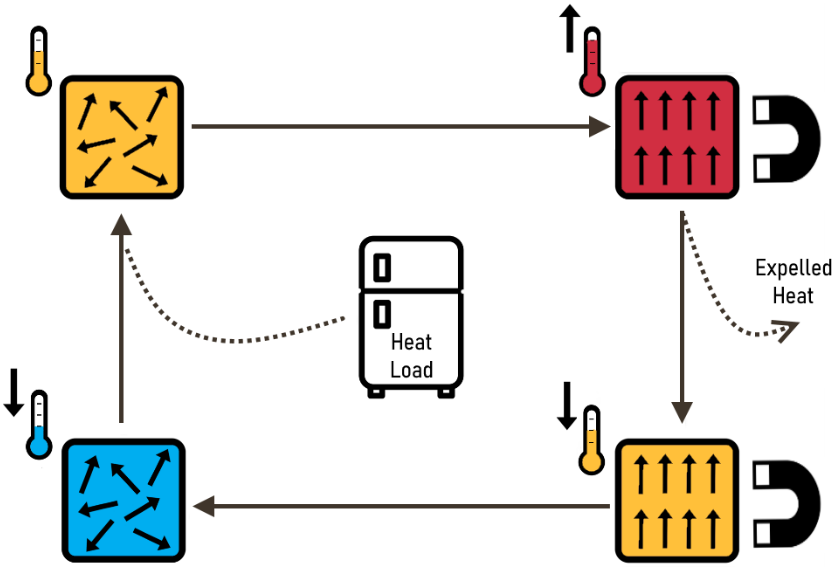

Figure 1.1: Schematic representation of magnetic refrigeration cycle.

Two major factors that significantly influence the effectiveness of the prototype devices are the magnitude of the applied field and the working temperature range of the refrigerant material. The MCE effect is most potent near the phase transition, while the temperature span of the refrigeration cycle is directly related to the ΔT_{ad} produced by the magnetocaloric material. With the minimal requirement of a 4 to 20 °C temperature span for a conventional fridge, a suitable magnetocaloric material must have a transition in the room-temperature region and produce a large enough ΔT_{ad} to support the necessary temperature range. The second requirement can be alleviated to some degree with the usage of the so-called Active Magnetic Regenerative Refrigeration cycle [17]. This cycle improves the temperature span by combining a set of magnetocaloric materials with similar ΔT_{ad} and gradually increasing transition temperatures. Due to the nature of MCE higher magnetic fields can lead to better performance. However, the costs and manufacturing complexity of high-field magnets render any benefits of such an approach negligible. The balanced cost/efficiency ratio for magnetocaloric refrigerators lies with permanent magnets that produce fields of 0.7–1 T. For this reason, the optimal candidate material has to show a high enough MCE in relatively low fields.

MR technology is still in its infancy and at the current stage of development, it still falls short of the conventional gas compression refrigerators. This is expected to be overcome with the development of higher efficiency MR systems. In fact, MR shows potential to match and overcome the performance of the current cooling technology [18], with an additional appeal of being ecologically friendly.

1.2.2 Thermomagnetic motors and generators

The reversible nature of the magnetocaloric effect allows for the creation of thermomagnetic motors and generators that could convert heat into electricity. Such devices were suggested already in the 19th century by Tesla [19] and Edison [20], but remained as concepts due to a lack of a suitable working material. A simple design of a thermomagnetic motor consists of a permanent magnet and a rotatable ring of magnetocaloric material Fig. 1.2. As part of the ring is cooled down, the material transitions into a ferromagnetic state and is attracted to the permanent magnet starting the rotation. Once the ferromagnetic part of the ring crosses the field region it warms up by a heat source, losing its magnetic order and freeing it from the grasp of the magnetic field. In this manner, a continuous rotation is possible as long as heat and cold sources are provided. The resulting torque can be harnessed and converted into electricity.

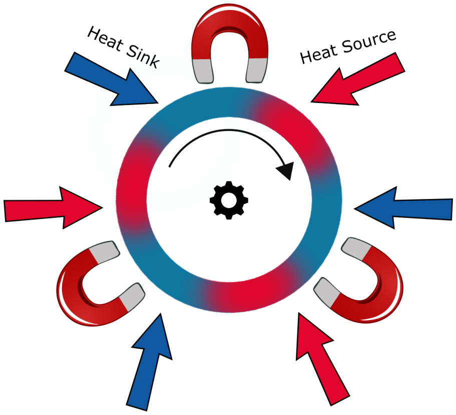

Figure 1.2: Working principle of the thermomagnetic generator.

A unique advantage of such devices lies in their working temperature. Currently, various industrial processes output a large amount of waste heat [21]. These relatively low temperatures cannot be utilized by typical heat-to-power converters, but this temperature range is perfect for devices based on RT MCE materials. Thus, thermomagnetic generators can pave the way to this yet untapped resource and provide efficient and eco-friendly power.

1.2.3 Medical applications

At the moment, two main applications for MCE in the medical field are being actively developed: controllable drug delivery to defined locations in the human body, and localized magnetic hyperthermia for cancer treatment.

Thermal therapy has proven to be an effective way to combat cancer, a major challenge of this approach is delivering the proper amount of heat to the correct part of the patient's body. High enough temperatures must be sustained for an accurate amount of time to damage the cancer cells. The temperature required to kill tumour cells lies between 40 °C and 45 °C. Overheating or heating in an incorrect area would damage healthy tissue, leading to severe consequences. For this reason, magnetocaloric materials, which can provide controlled heating *via* application or removal of the magnetic field, are a promising agent for hyperthermia treatment [22, 23].

The remote, noninvasive drug delivery to human organs or tissues is a challenging problem for which magnetocaloric materials may be a suitable solution. The delivery device should provide a controlled, reproducible, and reliable drug release. These requirements can be reached by combining magnetocaloric material with a polymer matrix carrying the drug. Upon application of magnetic field, the heat produced *via* the MCE would cause the polymer to dissolve, releasing the drug contained within [21, 24]. In the case of medical uses, the magnitude of the MCE is of less importance and the main focus is on the biocompatibility and accurate temperature range for the magnetic transition.

1.3 MAGNETOCALORIC MATERIALS

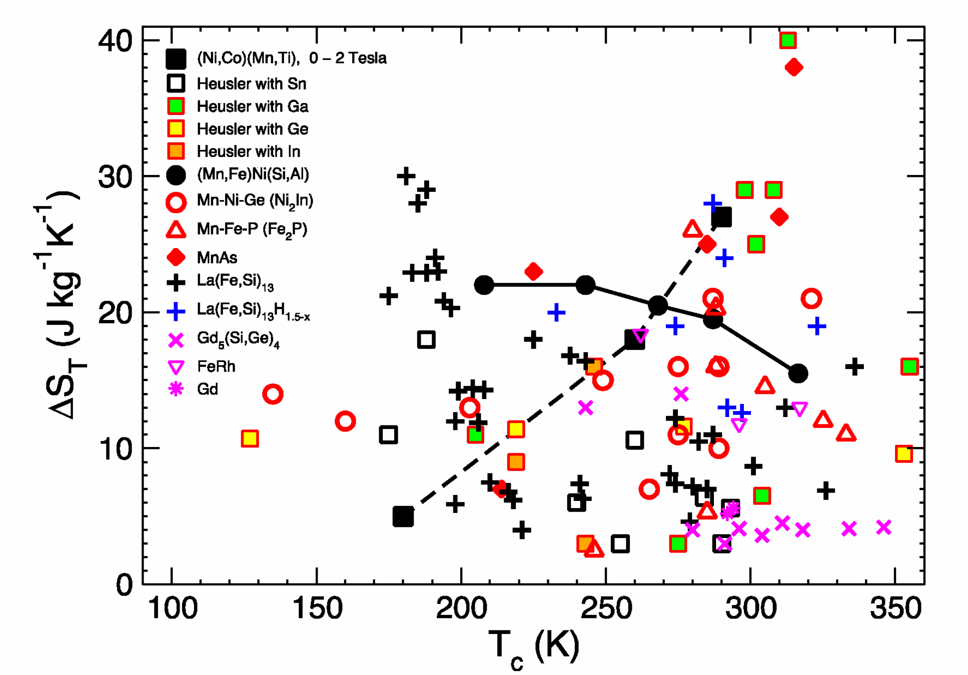

Figure 1.3: Isothermal entropy change ΔS_T (J kg^{-1} K^{-1}) at a field change of 2 T magnetic field change versus phase transition temperature T_C (K) for known materials exhibiting a GMCE [25].

TRADITIONALLY gadolinium has been used as a benchmark material when comparing the room temperature MCE performance. The discovery of $Gd_5Si_2Ge_2$ [11] that exhibits a giant magnetocaloric effect (GMCE) and shows a 50% improvement in performance over pure Gd prompted an extensive search for similar materials. This resulted in an exponential growth of reported systems. Among them are MnAs based compounds [26], MnCoGe-based alloys [27], FeRh alloys [28], Ni-Mn-Ti-based Heusler alloys [29]. The key to the GMCE in these systems lies in the first-order transition of magneto-structural or magneto-elastic type. The latter is generally preferential, as it is typically accompanied by less strain, which could cause progressive mechanical damage of the material in a cyclic operation. To improve affordability the search for new materials is focused on the low-cost compounds that can still demonstrate competitive MCE values. A major breakthrough came with the discovery of $(Mn,Fe)_2(P,As,Si)$ [30] and $La(Fe,Si)_{13}$ [31] systems, which are currently considered the best candidates for commercial room-temperature refrigeration due to the tunability of the Curie temperature over a large temperature span, abundant, non-toxic ingredients and their large MCE in low magnetic fields. The three main parameters used to compare magnetocaloric materials are ΔT_{ad}, ΔS_m and the transition temperature T_C. The design of the MR device, however, imposes further constraints on the material properties including production and material costs, mechanical stability, durability, corrosion resistance, heat conductivity, as well as environmental impact of the utilized ingredients [32–34]. Ideal magnetocaloric materials that present a balanced combination of these properties are necessary for the successful commercial implementation of magnetic cooling. This prompts continuous attempts to improve the properties of the known systems and keeps the search for new candidate materials relevant.

1.4 THESIS OUTLINE

THE main goal of the current thesis is to identify and optimize promising magnetocaloric materials. To this end an understanding of the driving force behind the giant magnetocaloric effect in known materials is necessary. For this, interpretation of the magneto-structural and magneto-elastic nature of the first-order transition is of particular interest. Knowledge of the underlying factors and requirements for a material suitable for room temperature refrigeration can be used to change our approach to the search for novel material systems.

The thesis consists of seven chapters with the following content:

Chapter 2 provides some theoretical aspects of the thermodynamic magnetocaloric effect and gives information on experimental and computational techniques utilized in the following chapters.

Chapter 3 describes an effective approach to the search for novel magnetocaloric materials based on high throughput database screening. Potential screening parameters for magnetocaloric materials are discussed and evaluated. A shortlist of promising magnetocaloric materials suggested by the screening process is presented.

Chapter 4 focuses on the $(Mn,Fe)_2(P, Si)$ system and provides an overview of possible dopants for this materials family. First-principles calculations are used to determine the site preferences and optimal lattice parameters for the substitutions with elements from the 2nd, 3rd and 4th periods. The effect of lithiation on magnetization and critical temperature and their connection to structural parameters of Fe_2P has been investigated in detail.

In **Chapter 5** two phases of the Fe-Mn-Y system are studied - $(Fe_{1-x}Mn_x)_{23}Y_6$ and less the known $(Fe_{1-x}Mn_x)_3Y$. The potential of both systems as cooling material for room-temperature refrigeration is estimated. The influence of the manganese to iron ratio is characterized.

Chapter 6 describes the structural and magnetic properties of $(Fe_{1-x}Ni_x)_5Sn_3$ compounds. Ni substitution is used to shift the magnetic transition to the room temperature range.

REFERENCES

[1] *Global Energy Review 2021*. 2021. URL: `https://www.iea.org/reports/global-energy-review-2021` (visited on 06/26/2021).

[2] *Global Cooling Prize*. URL: `https://globalcoolingprize.org/about-the-global-cooling-prize/the-need/` (visited on 06/26/2021).

[3] *Montreal Protocol*. United Nations. Jan. 1987. URL: `https://treaties.un.org/doc/publication/unts/volume%201522/volume-1522-i-26369-english.pdf` (visited on 06/26/2021).

[4] *Paris Agreement*. United Nations. Dec. 2015. URL: `https://treaties.un.org/pages/ViewDetails.aspx?src=TREATY&mtdsg_no=XXVII-7-d&chapter=27&clang=_en` (visited on 06/26/2021).

[5] A. Greco, C. Aprea, A. Maiorino, and C. Masselli. “A review of the state of the art of solid-state caloric cooling processes at room-temperature before 2019”. In: *Int. J. Refrig.* 106 (Oct. 2019), pp. 66–88. DOI: `10.1016/j.ijrefrig.2019.06.034`.

[6] O. Gutfleisch, M. A. Willard, E. Brück, C. H. Chen, S. G. Sankar, and J. P. Liu. “Magnetic Materials and Devices for the 21st Century: Stronger, Lighter, and More Energy Efficient”. In: *Adv. Mater.* 23.7 (Feb. 2011), pp. 821–842. DOI: `10.1002/adma.201002180`.

[7] V. K. Pecharsky and K. A. Gschneidner. “Advanced magnetocaloric materials: What does the future hold?” In: *Int. J. Refrig.* 29.8 (Dec. 2006), pp. 1239–1249. DOI: `10.1016/j.ijrefrig.2006.03.020`.

[8] P. Weiss and A. Piccard. “Le phénomène magnétocalorique”. In: *J. Phys. Théorique Appliquée* 7.1 (1917), pp. 103–109. DOI: `10.1051/jphystap:019170070010300`.

[9] P. Debye. “Einige Bemerkungen zur Magnetisierung bei tiefer Temperatur”. In: *Ann. Phys.* 386.25 (1926), pp. 1154–1160. DOI: `10.1002/andp.19263862517`.

[10] W. F. Giauque. “A thermodynamic treatment of certain magnetic effects. A proposed method of producing temperatures considerably below 1° absolute”. In: *J. Am. Chem. Soc.* 49.8 (Aug. 1927), pp. 1864–1870. DOI: `10.1021/ja01407a003`.

[11] V. K. Pecharsky and K. A. Gschneidner, Jr. “Giant Magnetocaloric Effect in $Gd_5(Si_2Ge_2)$”. In: *Phys. Rev. Lett.* 78.23 (June 1997), pp. 4494–4497. DOI: `10.1103/PhysRevLett.78.4494`.

[12] *Haier, Astronautics, and BASF present the first prototype of a magnetocaloric wine cooler*. URL: `https://www.basf.com/global/en/media/news-releases/2015/01/p-15-100.html` (visited on 06/26/2021).

[13] C. Aprea, A. Greco, A. Maiorino, and C. Masselli. “Magnetic refrigeration: an eco-friendly technology for the refrigeration at room temperature”. In: *J. Phys. Conf. Ser.* 655 (Nov. 2015), p. 012026. DOI: `10.1088/1742-6596/655/1/012026`.

[14] D. Champier. “Thermoelectric generators: A review of applications”. In: *Energy Convers. Manag.* 140 (May 2017), pp. 167–181. DOI: `10.1016/j.enconman.2017.02.070`.

[15] A. Tishin, Y. Spichkin, V. Zverev, and P. Egolf. “A review and new perspectives for the magnetocaloric effect: New materials and local heating and cooling inside the human body”. In: *Int. J. Refrig.* 68 (Aug. 2016), pp. 177–186. DOI: `10.1016/j.ijrefrig.2016.04.020`.

[16] K. Engelbrecht, C. Bahl, and K. Nielsen. “Experimental results for a magnetic refrigerator using three different types of magnetocaloric material regenerators”. In: *Int. J. Refrig.* 34.4 (June 2011), pp. 1132–1140. DOI: `10.1016/j.ijrefrig.2010.11.014`.

[17] S. W. Barclay J.A. *Active magnetic regenerator.* U.S. Patent 4,332,135, 1982.

[18] S. L. Russek and C. B. Zimm. “Potential for cost effective magnetocaloric air conditioning systems”. In: *Int. J. Refrig.* 29.8 (Dec. 2006), pp. 1366–1373. DOI: `10.1016/j.ijrefrig.2006.07.019`.

[19] N. Tesla. *Pyromagneto electric generator.* U.S. Patent 428,057, 1890.

[20] T. A. Edison. *Pyromagnetic generator.* U.S. Patent 476,983, 1892.

[21] H. Jouhara, N. Khordehgah, S. Almahmoud, B. Delpech, A. Chauhan, and S. A. Tassou. “Waste heat recovery technologies and applications”. In: *Therm. Sci. Eng. Prog.* 6 (June 2018), pp. 268–289. DOI: `10.1016/j.tsep.2018.04.017`.

[22] R. Iglesias-Rey, A. Vieites-Prado, B. Argibay, F. Campos, M. Bañobre-López, T. Sobrino, J. Rivas, and J. Castillo. “Magnetocaloric effect for inducing hypothermia as new therapeutic strategy for stroke: A physical approach”. In: *J. Appl. Biomed.* 15.1 (Jan. 2017), pp. 33–38. DOI: `10.1016/j.jab.2016.09.006`.

[23] A. O. Ayaş, E. Seçilmiş, and A. Ekicibil. “New application area for magnetocaloric materials: Hyperthermia method”. In: *J. Mol. Struct.* 1231 (May 2021), p. 130010. DOI: `10.1016/j.molstruc.2021.130010`.

[24] A. S. Komlev, R. R. Gimaev, and V. I. Zverev. “Smart magnetocaloric coatings for implants: Controlled drug release for targeted delivery”. In: *Phys. Open* 7 (May 2021), p. 100063. DOI: `10.1016/j.physo.2021.100063`.

[25] N. A. Zarkevich and V. I. Zverev. “Viable Materials with a Giant Magnetocaloric Effect”. In: *Crystals* 10.9 (Sept. 2020), p. 815. DOI: `10.3390/cryst10090815`.

[26] H. Wada and Y. Tanabe. “Giant magnetocaloric effect of $\mathrm{MnAs}_{1-x}\mathrm{Sb}_x$”. In: *Appl. Phys. Lett.* 79.20 (Nov. 2001), pp. 3302–3304. DOI: `10.1063/1.1419048`.

[27] C. Zhang, H. Shi, E. Ye, Y. Nie, Z. Han, and D. Wang. “Magnetostructural transition and magnetocaloric effect in MnCoGe–NiCoGe system”. In: *J. Alloys Compd.* 639 (Aug. 2015), pp. 36–39. DOI: `10.1016/j.jallcom.2015.03.118`.

[28] C. Sánchez-Valdés, R. Gimaev, M. López-Cruz, J. Sánchez Llamazares, V. Zverev, A. Tishin, A. Carvalho, D. Aguiar, Y. Mudryk, and V. Pecharsky. “The effect of cooling rate on magnetothermal properties of $Fe_{49}Rh_{51}$”. In: *J. Magn. Magn. Mater.* 498 (Mar. 2020), p. 166130. DOI: `10.1016/j.jmmm.2019.166130`.

[29] H.-L. Yan, L.-D. Wang, H.-X. Liu, X.-M. Huang, N. Jia, Z.-B. Li, B. Yang, Y.-D. Zhang, C. Esling, X. Zhao, and L. Zuo. “Giant elastocaloric effect and exceptional mechanical properties in an all-d-metal Ni–Mn–Ti alloy: Experimental and ab-initio studies”. In: *Mater. Des.* 184 (Dec. 2019), p. 108180. DOI: `10.1016/j.matdes.2019.108180`.

[30] O. Tegus, E. Brück, K. H. J. Buschow, and F. R. de Boer. “Transition-metal-based magnetic refrigerants for room-temperature applications”. In: *Nature* 415.6868 (Jan. 2002), pp. 150–152. DOI: `10.1038/415150a`.

[31] B. G. Shen, J. R. Sun, F. X. Hu, H. W. Zhang, and Z. H. Cheng. “Recent Progress in Exploring Magnetocaloric Materials”. In: *Adv. Mater.* 21.45 (Dec. 2009), pp. 4545–4564. DOI: `10.1002/adma.200901072`.

[32] E. Brück. “Developments in magnetocaloric refrigeration”. In: *J. Phys. D. Appl. Phys.* 38.23 (Dec. 2005), R381–R391. DOI: `10.1088/0022-3727/38/23/R01`.

[33] J. Lyubina. “Magnetocaloric materials for energy efficient cooling”. In: *J. Phys. D. Appl. Phys.* 50.5 (Feb. 2017), p. 053002. DOI: `10.1088/1361-6463/50/5/053002`.

[34] T. Gottschall, K. P. Skokov, M. Fries, A. Taubel, I. Radulov, F. Scheibel, D. Benke, S. Riegg, and O. Gutfleisch. “Making a Cool Choice: The Materials Library of Magnetic Refrigeration”. In: *Adv. Energy Mater.* 9.34 (Sept. 2019), p. 1901322. DOI: `10.1002/aenm.201901322`.

2

THEORETICAL ASPECTS AND EXPERIMENTAL TECHNIQUES

"They say a little knowledge is a dangerous thing, but it's not one half so bad as a lot of ignorance."

— Terry Pratchett

In this chapter, some key theoretical aspects of the magnetocaloric effect will be given. The thermodynamic background of the main quantifiers of the magnetocaloric effect - ΔS *and* ΔT_{ad} *is demonstrated. The classification of materials by the transition order is discussed. In the second part, the experimental techniques and sample preparation methods utilized during this work will be introduced.*

2.1 THERMODYNAMICS OF MAGNETOCALORIC EFFECTS

THE thermodynamic properties of a magnetic system in a magnetic field $\mu_0 H$ at the temperature T and pressure P can be described by the Gibbs free energy $G(T,P,H)$ [1–4]

$$G = U - TS + PV - \mu_0 HM \tag{2.1}$$

where U is the internal energy, V is the volume, M is the magnetization, and S represents the total entropy. The differential of the Gibbs free energy G is then:

$$dG = -SdT + VdP - Md(\mu_0 H) \tag{2.2}$$

In the case of a constant pressure it can be written through partial derivatives as:

$$dG(T,H) = \left(\frac{\partial G}{\partial T}\right)_{\mu_0 H,P} dT + \left(\frac{\partial G}{\partial \mu_0 H}\right)_{T,P} d(\mu_0 H) \tag{2.3}$$

The second derivatives are equal.

$$\left(\frac{\partial}{\partial(\mu_0 H)}\left(\frac{\partial G}{\partial T}\right)_{\mu_0 H}\right)_{T,P} = \left(\frac{\partial}{\partial T}\left(\frac{\partial G}{\partial(\mu_0 H)}\right)_{T}\right)_{\mu_0 H,P} \tag{2.4}$$

If they exist and are continuous, then the internal parameters V, M, S can be obtained in the form of partial derivatives of the Gibbs free energy.

$$V(T,P,\mu_0 H) = \left(\frac{\partial G}{\partial P}\right)_{T,\mu_0 H} \tag{2.5}$$

$$M(T,P,\mu_0 H) = -\left(\frac{\partial G}{\partial(\mu_0 H)}\right)_{T,P} \tag{2.6}$$

$$S(T,P,\mu_0 H) = -\left(\frac{\partial G}{\partial T}\right)_{P,\mu_0 H} \tag{2.7}$$

By combining equations (2.4), (2.5), (2.6), (2.7) gives the following Maxwell relation:

$$\left(\frac{\partial S}{\partial(\mu_0 H)}\right)_T = \left(\frac{\partial M}{\partial T}\right)_{\mu_0 H} \tag{2.8}$$

The total entropy change of a magnetic system is usually described as a combination of magnetic entropy (S_m), lattice entropy (S_l) and entropy of conduction electrons (S_e).

$$S(T,P,\mu_0 H) = S_m(T,P,\mu_0 H) + S_l(T,P,\mu_0 H) + S_e(T,P,\mu_0 H) \tag{2.9}$$

and its full differential in a closed system is therefore:

$$dS(T,P,\mu_0 H) = \left(\frac{\partial S}{\partial T}\right)_{\mu_0 H,P} dT + \left(\frac{\partial S}{\partial(\mu_0 H)}\right)_{T,P} d(\mu_0 H) + \left(\frac{\partial S}{\partial P}\right)_{T,\mu_0 H} dP \tag{2.10}$$

While all three contributions are dependent on the magnetic field, S_m exhibits the strongest field dependence, and therefore contributes most to the total entropy change during a variation in external magnetic field. In this case the total entropy change can be derived by integrating (2.8).

$$\Delta S(T, \mu_0 H) = \int_{\mu_0 H_0}^{\mu_0 H_1} \left(\frac{\partial M(T, \mu_0 H)}{\partial T} \right)_{\mu_0 H, P} d(\mu_0 H) \tag{2.11}$$

It is worth noting that contributions to the entropy change (2.9) cannot be separated in systems where the magnetic moments originate from itinerant electrons.
Continuing from (2.11) ΔT_{ad} can be obtained trough heat capacity $C_P(T, \mu_0 H)$:

$$C_P(T, \mu_0 H) = \left(\frac{\delta Q}{dT} \right)_{\mu_0 H, P} = \left(\frac{\partial S}{\partial T} \right)_{\mu_0 H, P} \tag{2.12}$$

In an isobaric-adiabatic process the adiabatic temperature change can be expressed through (2.8), (2.10) and (2.12):

$$dT(T, \mu_0 H) = -\frac{T}{C_P(T, \mu_0 H)} \left(\frac{\partial M(T, \mu_0 H)}{dT} \right)_{\mu_0 H, P} \tag{2.13}$$

And the total adiabatic temperature change can then be obtained through integration of (2.13):

$$\Delta T_{ad}(T, \mu_0 H) = -\int_{\mu_0 H_0}^{\mu_0 H_1} \frac{T}{C_P(T, \mu_0 H)} \left(\frac{\partial M(T, \mu_0 H)}{dT} \right)_{\mu_0 H, P} d(\mu_0 H) \tag{2.14}$$

While the Maxwell relation appears as an effective way to estimate entropy change, several conditions must be fulfilled for it to be accurate: the system must be homogeneous, remain in thermodynamic equilibrium and have a continuous first derivative of the Gibbs free energy [5, 6].

The two parameters, ΔS and ΔT_{ad}, derived above are a common way to quantify the magnetocaloric effect. The most suitable candidate would combine a maximum magnetic entropy change ΔS and a maximum adiabatic temperature change ΔT_{ad} with low hysteresis. ΔS effectively determines the cooling capacity, while ΔT_{ad} estimates the temperature span produced by the change in magnetic field. As can be seen from (2.11) and (2.14), the magnetocaloric effect would be most pronounced for a large $(\partial M/\partial T)_{\mu_0 H, P}$. This maximum occurs near the magnetic ordering temperature.

When considering the potential of a magnetocaloric material the nature of the magnetic transition plays an important role. First order phase transitions exhibit a significant discontinuous change in magnetization and therefore show great potential for MCE. The discontinuity in lattice parameters opens the possibility for magneto-elastic transitions. The combination of elastic and magnetic contributions can add up to a larger entropy change during such a transition. The latent heat accompanying the first order magnetic transition (FOMT), however, is typically accompanied by large hysteresis. The continuous second order magnetic transition (SOMT) on the other hand does not have hysteresis, but lacks the magnitude and sharpness of FOMT. To combine the advantages of both types of

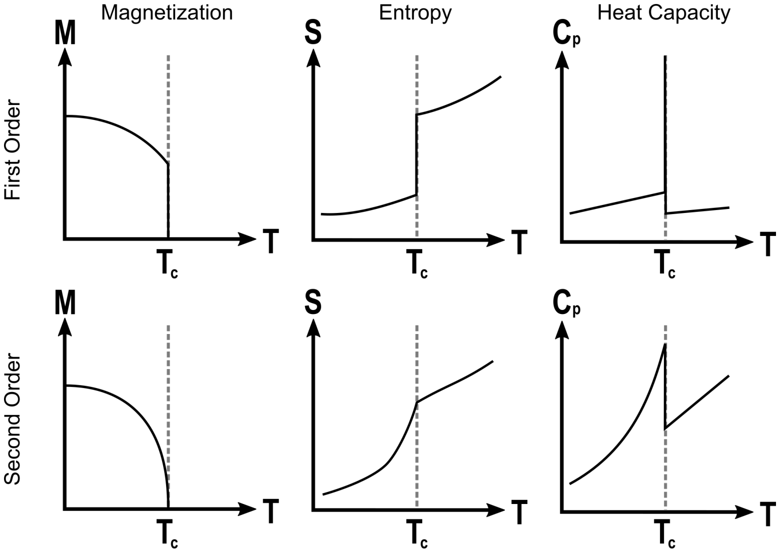

Figure 2.1: Schematic temperature dependence of the magnetization, entropy, and heat capacity according to the classification of magnetic phase transitions.

transitions a material that exhibits a critical nature of the transition is needed. In this case, the latent heat is low while, high magnetization change is maintained.

Additionally, the nature of the transition must be taken into consideration when ΔT_{ad} and ΔS are calculated. By definition, the FOMT has a discontinuity in the first derivative of the Gibbs free energy, which makes the application of Maxwell relations questionable. Despite this (2.11) is generally used for both types of transitions due to the fact that the FOMT shows a finite transition width in experiments. An alternative way to obtain the entropy change through the Clausius-Clapeyron relations has been suggested in [7].

There is a number of ways to determine the magnetocaloric effect using ΔT_{ad} and ΔS and estimate the magnetocaloric performance of a material [8, 9]. The most common techniques are based on an indirect measurement due to the widespread availability of commercial magnetometers and calorimeters. Direct measurements of the temperature change are technically more reliable, but typically require home-built experimental setups [10]. The variety of options creates a certain degree of ambiguity and hinders comparing the performance of different material families. Several parameters have been suggested as a universal metric for evaluating the MCE performance [11], but ΔS currently remains the most common way to report the magnetocaloric performance in literature.

2.2 SAMPLE SYNTHESIS

2.2.1 ARC-MELTING

ARC-MELTING is a process in which ingots of the desired stoichiometry are produced from pure elements or alloys in a protective argon atmosphere, using the discharge of an electrical arc as a heat source for the melting process. Arc-melting serves as a

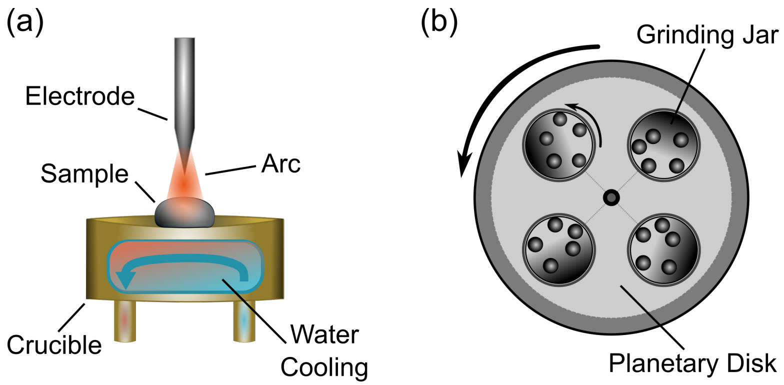

Figure 2.2: Schematic drawing of arc-melter (a), planetary ball mill (b).

reliable method for the synthesis of high purity alloys. An in-house arc-melting setup was used during sample preparations. A detailed description is available in [12]. A schematic illustration of the technique is shown in figure 2.2. In order to discharge the electrical arc, a DC power supply applies a low voltage (< 20 V) between two electrodes with the current from 100 A to 150 A. A water-cooled needle made out of tungsten serves as the cathode. The extremely high melting point of tungsten guarantees that it can safely bear the temperatures that are reached during the arc melting process. The anode is a copper crucible that holds the starting materials. To prevent the crucible from melting and to cool down the molten sample water cooling is connected to the crucible. As electrons travel from the crucible to the needle they lose their energy in the sample and heat it up. To avoid burning during the melting process, the air is pumped out from the working chamber to a 1×10^{-7} mbar vacuum. The chamber is then filled with argon, which acts as ionizing gas for the electrical arc. When the cathode is close enough to the crucible, ionization of the argon gas can be initialized by an RF pulse leading to a discharge of the electric arc. Once starting materials are molten and the arc is switched off the sample rapidly cools down, as the majority of heat is dissipated through the crucible. This may lead to a difference in cooling rate between the upper and lower parts of the sample and may cause inhomogeneities. To mediate this effect the melting cycle is repeated several times and the sample is turned over each time. A typical sample produced with this method is a ~5 g button.

2.2.2 BALL MILLING

BALL milling is a technique used for grinding and mechanical alloying of materials. Among many types of ball mills, planetary ball mills are most commonly used for lab-scale production of samples. In this mill type, the jars with material and grinding balls are placed on the planetary disk. As the disc rotates in one direction the grinding jars rotate around their axis in the opposite direction. High energy collisions between materials, balls and jar walls are used to mix and powderize the sample. The Fe_2PLi samples described in chapter 5 were prepared by ball milling using a Fritsch Pulverisette 5. The starting materials were placed inside a ball milling jar (80 mL) with 15 steel balls (10 mm diameter) and sealed in vacuum. Ball milling of 10 hours was applied through sequences of 15 minute milling at 350 rpm followed by a 10 minute break. The obtained powder was then pressed uniaxially into pellets.

2.2.3 HEAT TREATMENT

DUE to segregation, phases with another stoichiometry than the desired one are also formed during the synthesis process. This is most prevalent in cases when the desired phase lies close to competing ones in the phase diagram of the alloy. In this case, a heat treatment can be used to reduce secondary phases and homogenize the sample. For the heat treatment, as-prepared samples are placed in a vertical oven for a specific time and annealing temperature, which is based on the phase diagram of the binary alloy. To protect the samples from oxidation, they are first sealed in quartz ampoules with an argon atmosphere of 200 mbar. To preserve the high-temperature phase after annealing, the sample is cooled rapidly by quenching it into water.

2.3 SAMPLE CHARACTERIZATION

2.3.1 POWDER X-RAY DIFFRACTION

THE crystal structure of a material can be characterized through X-ray diffraction (XRD). X-ray diffraction patterns of the polycrystalline samples were obtained on PANalytical X-pert Pro diffractometer using Cu-Kα radiation at room temperature and operating at 45 kV and 40 mA. Patterns were recorded in the 2θ range from 10° to 100° with steps of 0.08°. The patterns were analyzed by Rietveld refinement using the FullProf package [13]. For each sample, the lattice parameters and the fraction of impurity phases were determined.

2.3.2 MAGNETIZATION MEASUREMENTS

THE majority of magnetization measurements was performed on a superconducting quantum interference device (SQUID), which offers excellent sensitivity for magnetic characterization of the samples. The SQUID Magnetic Property Measurement System (MPMS) magnetometer of Quantum Design (5S and XL models) used in this work supports a temperature range between 1.7 and 400 K and magnetic fields up to 5 T. For the measurements each sample is ground to powder and placed in a gelatine capsule. The typical sample mass is 2 mg. The capsule is then mounted in a plastic straw. The diamagnetic contribution of the sample holder is negligible compared to the relatively strong magnetic signal of the samples.

Two types of measurements were performed. The isofield magnetization curves ($M_B(T)$) were obtained in field upon heating from 5 to 370 K with a sweep rate of 2 K/min. These were performed both in a high field (1 T) and a low field (0.01 T). Low field measurements were used to determine the transition temperature. For the isothermal magnetization curves ($M_T(B)$) the samples were measured in fields ranging from 1 to 5 T in increments of 0.2 T at a temperature of 5 K.

Magnetic entropy change ΔS_M was calculated from $M_B(T)$ curves for both a field change of 0–1 T and a field change of 0–1.5 T in steps of 0.15 T.

For the samples with transition temperatures outside the temperature range of the SQUID-MPMS the Physical Property Measurement System(PPMS) Versalab of QuantumDesign was used instead. The Vibrating Sample Magnetometer (VSM) can be equipped with an oven and therefore offers two temperature ranges for continuous measurements from 5 to 300 K and from 300 to 650 K. Only the $M_B(T)$ curves were measured with the PPMS VSM. The samples were measured in field, heating from 300 to 650 K, both in high field (1 T) and in low field (0.01 T).

2.4 DENSITY FUNCTIONAL THEORY CALCULATIONS

THE various material properties of the compounds are the result of their electronic structure. Therefore, the ability to predict and understand the electronic structure would allow, to a large degree, to predict and quantify these properties.

Attempts to make such a methodology began in the early 20th century, soon after the discovery of the Schrödinger equation. The first approach introduced by Slater and Fock utilized a combination of Hartree's self-consistent field method and Schrödinger equation to obtain solutions for wavefunctions and energies for atoms and molecules [14]. While this method became the first successful realization of *ab-initio* modelling of electronic properties, its usefulness was limited as it neglects electron correlations and requires tremendous computational costs. In the 1960s another method was proposed by Hohenberg, Kohn [15] and Sham [16]. They introduced two theorems that laid the basis for density functional theory (DFT). The first theorem shows that the properties of a many-electron system are unambiguously determined by the electron density $n(\mathbf{r})$. The second defines an energy functional for the system ($E[n(\mathbf{r})]$) and demonstrates that the ground-state electron density corresponds to a minimum of this functional.

$$E[n(\mathbf{r})] = T_s[n(\mathbf{r})] + \int v_{ext}(\mathbf{r})n(\mathbf{r})d\mathbf{r} + E_{Hartree}[n(\mathbf{r})] + E_{xc}[n(\mathbf{r})] \qquad (2.15)$$

Where $T_s[n(\mathbf{r})]$ is the functional of the kinetic energy of non-interacting electrons, $v(\mathbf{r})_{ext}$ is the external potential acting on the interacting system and $E_{Hartree}[n(\mathbf{r})]$ is the Hartree energy. $E_{xc}[n(\mathbf{r})]$ is the exchange correlation energy and represents all other interactions between the electrons.

The exchange correlation energy can be approximated in a number of ways. The one used in this work is the generalized gradient approximation of Perdew–Burke–Ernzerhof (PBE) [17]. In short, DFT is an efficient method to obtain an approximate solution to the Schrödinger equation of a many-body system. It simplifies solving the many-body problem to a problem of minimization of the electron density functional. This method is realized within the Viena *ab-initio* simulation package (VASP) [18, 19]. In a self-consistent cycle, the Kohn-Sham equation is solved until the convergence criteria are met and the final solution is reached. The ion-electron interactions are described *via* the projector augmented-wave (PAW) method [17, 20]. VASP was used in this work to investigate the structural, magnetic and electronic properties of the materials.

Specific details for all calculations are provided in the relevant chapters.

REFERENCES

[1] J. Maxwell. *Theory of heat.* Longmans, Green, and Company: London, UK, 1872.

[2] M. Kuz'min and A. Tishin. "Magnetocaloric effect. Part 1: An introduction to various aspects of theory and practice". In: *Cryogenics (Guildf).* 32.6 (Jan. 1992), pp. 545–558. DOI: `10.1016/0011-2275(92)90041-8`.

[3] A. Tishin and Y. Spichkin. *The magnetocaloric effect and its applications.* Bristol Philadelphia, 2003.

[4] R. A. Swalin and S. A. Rice. "Thermodynamics of Solids". In: *Phys. Today* 16.1 (Jan. 1963), pp. 72–74. DOI: `10.1063/1.3050727`.

[5] J. Amaral and V. Amaral. "On estimating the magnetocaloric effect from magnetization measurements". In: *J. Magn. Magn. Mater.* 322.9-12 (May 2010), pp. 1552–1557. DOI: `10.1016/j.jmmm.2009.06.013`.

[6] L. Tocado, E. Palacios, and R. Burriel. "Entropy determinations and magnetocaloric parameters in systems with first-order transitions: Study of MnAs". In: *J. Appl. Phys.* 105.9 (May 2009), p. 093918. DOI: `10.1063/1.3093880`.

[7] M. Balli, D. Fruchart, D. Gignoux, and R. Zach. "The "colossal" magnetocaloric effect in $Mn_{1-x}Fe_xAs$: What are we really measuring?" In: *Appl. Phys. Lett.* 95.7 (Aug. 2009), p. 072509. DOI: `10.1063/1.3194144`.

[8] V. K. Pecharsky and K. A. Gschneidner. "Magnetocaloric effect from indirect measurements: Magnetization and heat capacity". In: *J. Appl. Phys.* 86.1 (July 1999), pp. 565–575. DOI: `10.1063/1.370767`.

[9] H. Neves Bez, H. Yibole, A. Pathak, Y. Mudryk, and V. Pecharsky. "Best practices in evaluation of the magnetocaloric effect from bulk magnetization measurements". In: *J. Magn. Magn. Mater.* 458 (July 2018), pp. 301–309. DOI: `10.1016/j.jmmm.2018.03.020`.

[10] A. Giguère, M. Foldeaki, B. Ravi Gopal, R. Chahine, T. K. Bose, A. Frydman, and J. A. Barclay. "Direct Measurement of the "Giant" Adiabatic Temperature Change in $Gd_5Si_2Ge_2$". In: *Phys. Rev. Lett.* 83.11 (Sept. 1999), pp. 2262–2265. DOI: `10.1103/PhysRevLett.83.2262`.

[11] L. D. Griffith, Y. Mudryk, J. Slaughter, and V. K. Pecharsky. "Material-based figure of merit for caloric materials". In: *J. Appl. Phys.* 123.3 (Jan. 2018), p. 034902. DOI: `10.1063/1.5004173`.

[12] M. Boeije. "Electron density studies on magnetic systems". PhD thesis. TU Delft, 2017.

[13] J. Rodríguez-Carvajal. "Recent advances in magnetic structure determination by neutron powder diffraction". In: *Phys. B Condens. Matter* 192.1-2 (Oct. 1993), pp. 55–69. DOI: `10.1016/0921-4526(93)90108-I`.

[14] J. C. Slater. “Note on Hartree’s Method”. In: *Phys. Rev.* 35.2 (Jan. 1930), pp. 210–211. DOI: `10.1103/PhysRev.35.210.2`.

[15] P. Hohenberg and W. Kohn. “Inhomogeneous Electron Gas”. In: *Phys. Rev.* 136.3B (Nov. 1964), B864–B871. DOI: `10.1103/PhysRev.136.B864`.

[16] W. Kohn and L. J. Sham. “Self-Consistent Equations Including Exchange and Correlation Effects”. In: *Phys. Rev.* 140.4A (Nov. 1965), A1133–A1138. DOI: `10.1103/PhysRev.140.A1133`.

[17] J. P. Perdew, K. Burke, and M. Ernzerhof. “Generalized Gradient Approximation Made Simple”. In: *Phys. Rev. Lett.* 77.18 (Oct. 1996), pp. 3865–3868. DOI: `10.1103/PhysRevLett.77.3865`.

[18] G. Kresse and J. Hafner. “Ab initio molecular dynamics for liquid metals”. In: *Phys. Rev. B* 47.1 (Jan. 1993), pp. 558–561. DOI: `10.1103/PhysRevB.47.558`.

[19] G. Kresse and J. Furthmüller. “Efficiency of ab-initio total energy calculations for metals and semiconductors using a plane-wave basis set”. In: *Comput. Mater. Sci.* 6.1 (July 1996), pp. 15–50. DOI: `10.1016/0927-0256(96)00008-0`.

[20] G. Kresse and D. Joubert. “From ultrasoft pseudopotentials to the projector augmented-wave method”. In: *Phys. Rev. B* 59.3 (Jan. 1999), pp. 1758–1775. DOI: `10.1103/PhysRevB.59.1758`.

3

COMPUTATIONAL SCREENING OF MAGNETOCALORIC MATERIALS

"There are always enough facts – it's imagination that's lacking."

— Dmitri Blokhintsev

In this chapter, an effective approach to the screening of magnetocaloric materials based on the information obtained from crystallographic databases is demonstrated. To identify systems of interest several screening parameters were developed using properties of various well-known MCE materials as a reference. Along with magnetic properties, other factors important for practical applications are taken into consideration including price, availability and toxicity of candidate materials. Combining these criteria an algorithm for the screening process is suggested. It utilizes information readily available in databases and additional ab-initio calculations. A step-by-step application of initial screening parameters to sort out unsuitable materials before performing more computationally heavy assessments allows fast processing of a large number of candidates. This results in a shortlist of promising compounds ranked by their potential, which can serve as a guide for experimental research.

3.1 COMPUTER-ASSISTED SEARCH FOR NEW MATERIALS

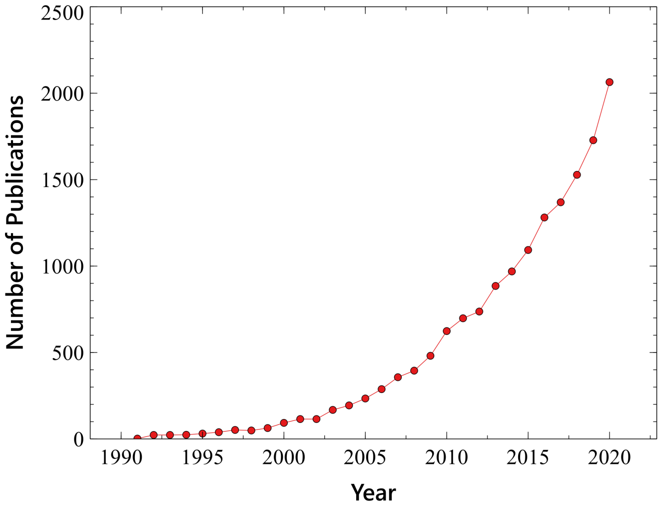

Figure 3.1: Annual number of publications with titles, abstracts or keywords mentioning "computational screening". Data obtained from the Web of Science.

THE conventional strategy to material discovery is largely based on trial-and-error experiments, typically based on empirical structure-property relationships. This approach requires a significant investment of time and resources, yet the effort spent on investigating a candidate material, quite often does not produce the desired results. The development of computational methods and ease of access to years of accumulated knowledge in the form of material databases has resulted in the birth of new material discovery paradigms. The fast-paced improvement of computational power and widespread availability of computing resources has made these new methods, also known as *in silico* studies a convenient tool for many scientists. The use of computers allows for relatively fast and inexpensive tests compared to the usual experimental approach. Common *in silico* cases are machine learning, database mining and high-throughput computations.

Recently, high-throughput screening (HTS), usually based on DFT calculations, has been successfully applied in a variety of research fields. Examples include, but are not limited to: electrocatalysts [1], cathode materials for batteries [2], thermoelectric materials [3], stainless steels [4], permanent magnets [5, 6] and other types of functional magnetic materials as reviewed in [7]. Following the popularity of HTS, several codebases for high-throughput computations were developed. Noticeable examples are Atomate [8] and AiiDA [9]. These toolboxes replace manual monitoring of individual computational jobs with workflows that automatically perform calculations for thousands of compounds and evaluate results. Such calculations resulted in information about thousands of compounds. The necessity to organize this information naturally led to the creation of open-access computational databases *e.g.* Materials Project [10] AFLOWlib [11] and OQMD [12].

Similarly, machine learning has been gaining popularity and found applications in material science. For instance, it was used to investigate mechanical properties of steels

[13] and search for rare-earth free permanent magnets [14]. Algorithms are trained to find patterns and correlations in datasets and to make the best decisions and predictions based on that analysis. This allows to reduce the complexity of data and find connections and underlying trends that may not be immediately obvious to the researcher relying on conventional wisdom. The requirement for this method is a large number of examples, both positive and negative, to perform the initial training. Models become more accurate the more data they have access to.

Lastly, data mining is most often used in combination with either of the two approaches discussed above as a preparatory step. It relies on parsing various material databases according to specific parameters. The choice of such parameters is crucial, as they can only be based on the information contained in the database, but have to accurately enough distinguish the subgroup of materials of interest. It also serves as a statistical tool that can highlight commonalities among groups of compounds that remained unnoticed when individual materials were investigated. Data mining was used to identify potential materials for radiation detectors [15], batteries [16] and to analyze the performance of Sm-Co-based permanent magnets [17].

3.2 *IN SILICO* METHODS APPLIED TO MAGNETOCALORIC MATERIALS

When it comes to magnetocaloric materials, the application of *in silico* computational methods has only started recently. Nevertheless, some studies demonstrate promising results of such an approach to the development and discovery of magnetocaloric materials.

The general approach to the HTS of caloric (including magnetocaloric) materials was first described by Zarkevich *et al.* [18], as a part of the CaloriCool consortium. The consortium aims to accelerate the discovery of novel caloric materials by creating a database of compounds that are likely to have high-performance caloric properties. To this end, several steps are proposed. First, by scraping information from literature and known phase diagrams, materials with non-critical, non-toxic elements are collected. A series of rough estimates follows. Material cost is gauged by the price of constituent elements. Only diffusionless transformation transitions are considered to be of interest. Therefore, compositions of different phases are compared to check if both phases have the same composition and diffusional phase transformations are discarded. The potential magnetization is judged based on atomic magnetic moments calculated from the number of unpaired electrons. After initial estimates, a subset of materials is produced and then DFT calculations are performed to obtain the electronic properties. This information can then be used for further screening. Eventually, the remaining candidates can be fabricated and investigated. The CaloriCool initiative provides a fundamental approach to the search for caloric materials, yet it is not focused on the MCE. Consequently, at the moment, it does not include sufficiently precise screening criteria to distinguish the most promising magnetocaloric candidates after the initial rough screening is performed.

Several works describe the application of machine learning to study the MCE. Zhang *et al.* [19] investigated the Curie temperature T_C and magnetic entropy change ΔS for magnetic field changes of 2 and 5 T for the $\mathrm{La(Fe,Si)_{13}}$ material family. The predictions are based solely on composition. 141 data points gathered from experimental results create the full dataset. Part of it was used for training (80%) and the rest (20%) for testing the obtained model. Results indicate a high degree of predictive accuracy. The authors suggest that by including additional parameters, for example, lattice parameters and saturation magnetization, the predictive ability of their model can be further improved. In a similar work, [20, 21], ΔS for 5 T a field change was predicted based on structural parameters and composition for lanthanum manganites. This model is based on 74 (in the earlier report) and 113 (in the latter one) experimental measurements and demonstrates how a bigger dataset improves the training quality. Yet another report [22] describes how the MCE performance in the $Mn_xFe_{2-x}P_{1-y}Si_yB_z$ system can be estimated from composition ratios. The model predicts Curie temperature, thermal hysteresis, and magnetic entropy change and is trained on 465 experimental points. Based on the results the authors suggest an optimal metal/non-metal ratio of 1.95 and optimal fractions in ranges of $1.10 \leq x(\mathrm{Mn}) \leq 1.30$ and $0.075 \leq z(\mathrm{B}) \leq 0.080$ at $y(\mathrm{Si}) = 0.33$.

While machine learning seems to perform well within single-family compounds it becomes less accurate once we consider it for a large scale search of completely new materials. The main reason being the lack of a balanced starting dataset. While there is a large number of known materials to show a relatively small MCE, there are very few positive examples with a large MCE. Therefore, currently training a highly accurate model is challenging. Nevertheless, a successful example of the application of machine learning for the search of completely new magnetocaloric systems is demonstrated in [23]. Here, literature reports describing various magnetocaloric materials were parsed to build a large dataset with values of ΔS for 1644 magnetocaloric materials. Chemical composition and the applied field change were used as features to forecast ΔS. After training and testing, the model was applied to another 818 magnetic materials for which the MCE has not been reported yet. The model predicted several materials to exhibit a decent entropy change. Among them, HoB_2 displayed the highest $\Delta S = 16.3\,\mathrm{J\,kg^{-1}\,K^{-1}}$. After the samples were prepared, the experimental value turned out to be $40.1\,\mathrm{J\,kg^{-1}\,K^{-1}}$ at the transition temperature of 15 K. Despite a large difference between predicted and measured values the model successfully identified a previously unknown system with a considerable MCE. Machine learning can be further used to search for transition temperatures in a suitable range, as demonstrated in [24]. In this study, Curie temperatures were predicted for ferromagnets in general, with an accuracy of about 50 K, only based on composition.

Efforts have been made to come up with criteria based on electronic and structural information that can represent the magnetocaloric performance. These criteria are necessary to narrow down the list of candidates during the computational screening. Unlike other physical properties like band gaps, absorption energies for catalysts, or thermoelectric properties, the characterization of magnetocaloric properties (*e.g.* ΔS) solely based on DFT offers a unique challenge.

The first step in the development of such a criterion was made by Bocarsly *et al.* [25, 26]. In their work the authors propose to link entropy change to a parameter that represents lattice deformation between a magnetic and a non-magnetic state. This is based on the connection of the magneto-volume coupling to first-order phase transitions. The proposed numerical parameter Σ_M represents the degree of lattice deformation between the DFT-optimized non-magnetic and magnetic unit cells. From the transformation matrix P between magnetic and non-magnetic structures the Lagrangian strain tensor η is derived

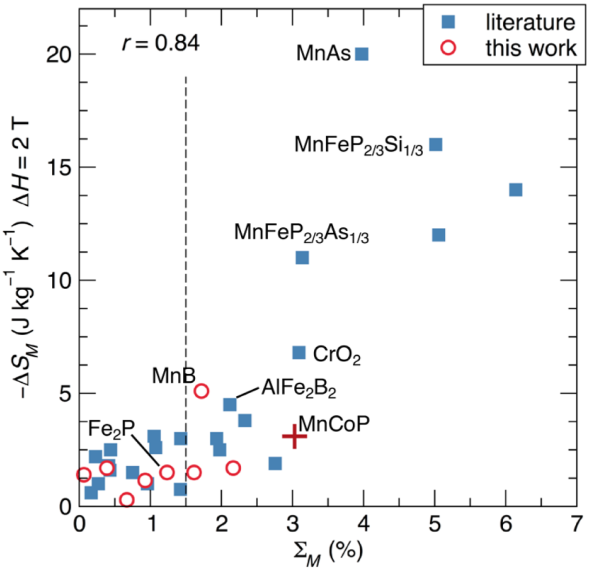

Figure 3.2: Comparison of the magnetic deformation, Σ_M, and experimental entropy change ΔS under an applied magnetic field from 0 to 2 T [25].

as:

$$\eta = \frac{1}{2}\left(P^T P - I\right) \tag{3.1}$$

And Σ_M is the root-mean-square of its eigenvalues as a percentage:

$$\Sigma_M = \frac{1}{3}\sqrt{\eta_1^2 + \eta_2^2 + \eta_3^2} \times 100\% \tag{3.2}$$

To test this parameter a dataset of 33 materials was used with reported ΔS values for a field change of 2 T. The magnetic entropy change ΔS_M as a function of magnetic deformation Σ_M is plotted in Figure 3.2. A correlation between the entropy change and the magnetic deformation can be observed with Pearson's $r = 0.84$. The linear trend appears to hold better for materials with low values of ΔS, and the ones with high ΔS deviate stronger from the linear response. Possibly, this simply is because there are not enough materials with high performance in the dataset to give a conclusive picture. Even though the initial idea aimed to identify first-order materials, Σ_M seems to also apply to second-order materials. Bocarsly *et al.* suggest using a magnetic deformation criterion with a cut off point of 1.5% and consider any material exhibiting a higher Σ_M a viable candidate.

To compliment Σ_M Tantillo [27] proposed an additional parameter based on the density of states (DOS). The idea comes from an earlier report [28], which describes that GMCE materials have sharp peaks in the DOS close to the Fermi energy. The difficulty lies in finding a way to identify these peaks and assess their sharpness to create a simple quantitative parameter. The proposed solution named "DOS ratio" ρ_d is the product of three parameters. First, assuming that the Fermi energy is between adjacent peaks of opposite spin polarization, the difference in amplitude of the peaks d_p is calculated. Next, the difference in energies at which peaks are observed s_E is measured. Finally, to estimate sharpness, the average curvature of the peaks c_{avg} is taken. For these calculations, only the range of ±1.5 eV from the Fermi energy is considered.

$$\rho_d = d_p^{\alpha_1} s_E^{\alpha_2} c_{avg}^{\alpha_3} \tag{3.3}$$

Based on the dataset of Bocarsly [25] this parameter shows accuracy similar to Σ_M discussed earlier. Results of linear regression modeling to predict ΔS are judged by the mean square error: for Σ_M it amounts to 11.1 $\mathrm{J\,kg^{-1}\,K^{-1}}$ and for ρ_d to 13.8 $\mathrm{J\,kg^{-1}\,K^{-1}}$. It is indicated that using these two parameters together further improves the predictive accuracy.

The entropy change can also be estimated from first-principles calculations more directly, as shown by Vieira *et al.* [29]. They propose to use the entropy difference between the magnetic phases as an approximation for experimental ΔS. However, the transition itself and the field contribution are not included. The entropy in each phase is calculated as a sum of three independent contributions: the electronic, magnetic and lattice entropy. In this case coupling (typically strong for magnetocaloric materials) between lattice and magnetic degrees of freedom is ignored. Consequently, their contribution is overcounted in the final sum. This approximation is still relatively accurate, but comes with a certain degree of complexity, needed to get reliable estimations for the different contributions. The authors review several ways to calculate each one and suggest the options that provide the highest precision. The electronic contribution is obtained from the DOS by the mixing entropy of occupied and unoccupied states:

$$\Delta S_{ele} = -k_B \int D(\varepsilon)[([1-f(\varepsilon,T)])\ln(1-f(\varepsilon,T)) + f(\varepsilon,T)\ln(f(\varepsilon,T))]\,d\varepsilon \tag{3.4}$$

where $D(\varepsilon)$ is the DOS, f is the Fermi-Dirac distribution and k_B is the Boltzmann constant. The magnetic entropy is calculated *via* the magnon density of states (MDOS) from the adiabatic magnon spectrum. MDOS is in turn computed from the adiabatic magnon spectrum based on exchange parameters acquired from DFT.

$$\Delta S_{mag} = k_B \int_0^{\infty} g(\varepsilon)[(1+n(\varepsilon,T))\ln(1+n(\varepsilon,T)) - n(\varepsilon,T)\ln(n(\varepsilon,T))]d\varepsilon \tag{3.5}$$

where $g(\varepsilon)$ is the MDOS and n is the Bose-Einstein distribution. The lattice entropy variation is derived from the vibrational density of states (VDOS) determined by calculating the phonon dispersion. The expression for S_{lat} is the same as (3.5), with $D(\varepsilon)$ replaced by VDOS. FeRh was used as a test case and demonstrated sufficiently accurate results (calculated $\Delta S_{calc} = 24.8\,\mathrm{J\,kg^{-1}\,K^{-1}}$ vs experimental $\Delta S_{exp} = 17\,\mathrm{J\,kg^{-1}\,K^{-1}}$), but further validation is needed on a wider range of materials before this parameter can be reliably used. The calculation is computationally rather heavy but can be applied at later stages of the screening process, once the remaining number of candidates is low.

3.3 SCREENING PARAMETERS FOR MCE

ONE of the main challenges in screening is finding out what features make materials exhibit qualities of interest and represent these features as quantitative criteria. The basic idea is to look at known MCE materials and figure out the common points. The interest in magnetic cooling devices has led to an intensive search for well-performing magnetocaloric materials. Yet, only a few materials systems are found suitable for commercial applications. Just three have been integrated into prototype devices – pure Gd, $(Mn,Fe)_2(P,As,Si)$ and $La(Fe,Si)_{13}$. What makes these unique are the perfect combination of all the essential characteristics of a good magnetocaloric material. These are:

- Non-toxic and non-critical
- Low porosity
- Corrosion-resistance and mechanical stability
- Retains MCE in powder/microbead form
- High thermal conductivity
- Large ΔT_{ad} and ΔS_M
- Suitable transition temperature
- Low manufacturing costs and ease of preparation/production

To find a similar material we need to incorporate as many of these requirements as possible into screening parameters. As discussed before the two main metrics (ΔS_M and ΔT_{ad}) cannot be directly obtained from DFT. To complicate things more, several different physical mechanisms behind high values of ΔS_M and ΔT_{ad} have been reported.

For our screening routine, we came up with a set of parameters that can be divided into two categories: “sieves” that have thresholds that a material must meet to pass the screening and “flags”. Flags refer to properties that do not have strict limits, but serve as an additional positive indicator. Below all the parameters are discussed in the order of increasing computational difficulty.

Chemical composition serves as the very basic parameter. We divided all elements in the periodic table into two categories. A “**blacklist**” which contains elements that must not be present in the composition and a “**whitelist**” from which at least one element must be present. This can be seen in Fig. 3.3. Elements in the whitelist are the primary source of magnetism and are found in all known non-rare-earth based magnetocaloric compounds. The elements populating the blacklist are either expensive (Re, Os, Ir, Pt, Au, In, Cs), radioactive (Tc, Po, Np, U, Pu, Th), hazardous (Be, As, Cd, Ba, Hg, Tl, Pb, Ac) or belong to noble gases (He, Ne, Ar, Kr, Xe). All elements from 7th period are also excluded. Note, that rare-earths(RE) are not kept out despite their high costs, as the final composition may still be a viable candidate as long as the RE content is low enough.

We do however calculate the composition **ratio between RE and non-RE elements** and use it as a flag. Compounds with a lower percentage of RE elements would be given more priority when evaluating the screening results. Preferably it should be kept below 50%, but it may vary depending on the specific RE element.

Another flag, in a way connected to the previous one, is the rough **price estimate** in EUR/kg. It is calculated by taking the market price for each element in the formula and summing it up according to the weight ratio. This does not include the price of preparing

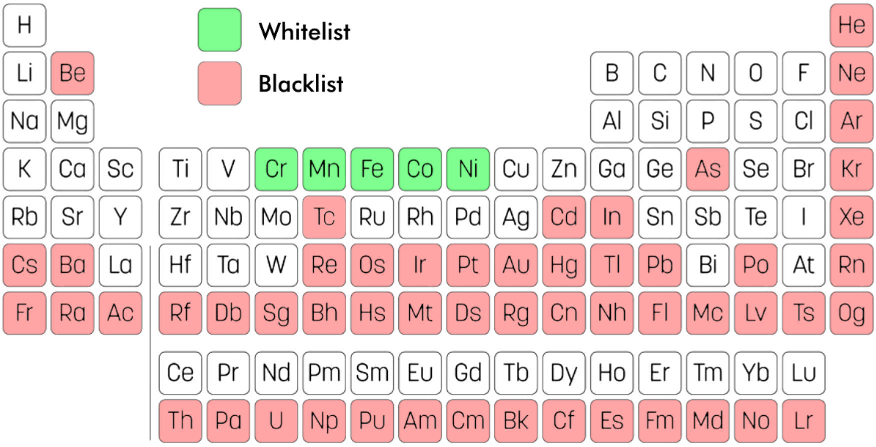

Figure 3.3: Suggested rules of element choice for MCE materials. Suitable composition can contain any "non-red" elements as long as at least one of the "green" elements is included.

the compound, and can also sometimes be an overestimation since occasionally alloys can be used in the synthesis instead of just pure elements.

For the material to have a significant MCE it has to be sufficiently magnetic. We can roughly estimate this simply by checking the composition for the elements that can bear magnetic moments. If the **ratio of magnetically active to inactive atoms** in the composition is high enough one can expect a decent magnetization. The cut off point is set at 50% and any material below this threshold is discarded. For this estimate the following elements are considered as magnetically active: Ti, V, Cr, Mn, Fe, Co, Ni, Nb, Mo, Ru, Rh, Pd, Ce, Pr, Nd, Sm, Eu, Gd, Tb, Dy, Ho, Er, Tm, Yb.

Similarly, the percentage of oxygen in the composition is calculated. The **oxygen content** is used as a parameter as the majority of the known magnetocaloric materials belong to metallic and intermetallic compounds. Some manganites are known to exhibit a large entropy change, but it is usually accompanied by relatively low ΔT_{ad}. In the current work, we have set the limit to 0%, partly for the reason that we believe that our main screening parameter – the magneto-elastic coupling is ill-suited for oxide materials, which usually have magnetism originating from the indirect exchange and are less sensitive to structural deformations.

Another flag that can highlight materials of interest is the **number of polymorphs** known for a certain composition. This number is acquired by counting the crystal structures (space groups) reported for one chemical formula in the database. A bigger number may indicate structural instabilities and transitions (*e.g.* Heusler alloys).

Certain structural features may be preferential for MCE such as the **number of unique magnetic sites** (sub-lattices). This is calculated as the number of distinct Wyckoff positions occupied by magnetic elements and disregarding their multiplicity. Generally, a bigger number corresponds to a more complicated magnetic structure and the possibility of

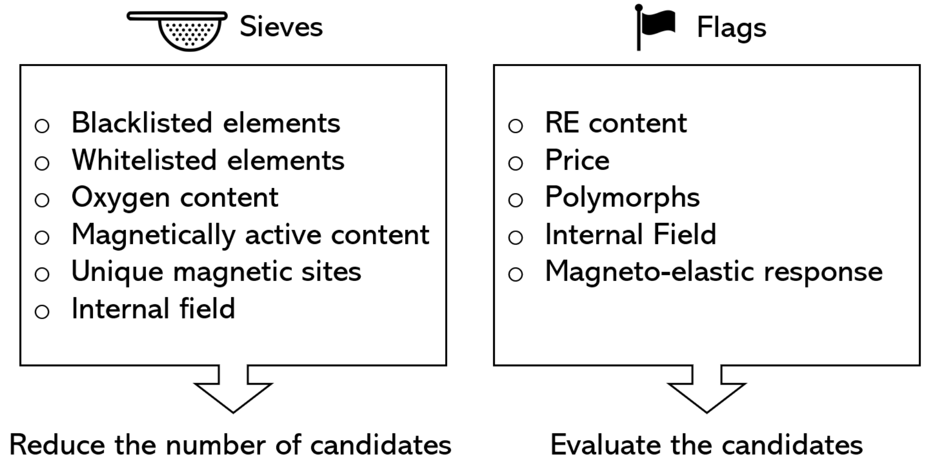

Figure 3.4: Types and purposes of the parameters for MCE screening

interesting interactions. Multiple inequivalent crystallographic sites enhance the chance of a large magneto-elastic coupling and the proximity to structural or electronic instabilities. At least 2 unique magnetic sites must be present to pass the screening.

One of the important parameters for the magnetocaloric performance is the magnetization in the FM phase. It can be directly evaluated with DFT through the magnetic moments. As a metric of magnetization, we suggest the **internal magnetic field** $\mu_0 M_s$ (in tesla), which is effectively the normalization of magnetic moment to volume.

$$\mu_0 M_s = \mu_0 \frac{\mu_s}{V} \tag{3.6}$$

where μ_0 is vacuum permeability, V is the volume of the cell used in the DFT calculation, μ_s is the calculated total moment per cell. Based on the values for known materials the cut off point is set at 0.45 T. Materials with lower internal fields are unlikely to produce a large enough MCE for practical applications. On the other hand, compounds with the highest values should be favoured.

The magneto-elastic response (γ_M), our proxy of choice for ΔS_M, is the final screening parameter. It is described in detail in the next section (3 . 4). While we have not set a strict minimal acceptance value, from our observations $\gamma_M \geq 8$ is recommended.

3.4 MAGNETO-ELASTIC RESPONSE — A COMPUTATIONAL PROXY FOR ΔS

A strong magneto-elastic coupling is a signature of a promising MCE material. In an earlier DFT study for a range of materials, Bocarsly [25] compared the non-magnetic and magnetic state and their relative influence on the volume change and unit cell distortion, characterised by the parameter Σ_M (%). For our criterion, we adopt the opposite approach: change the lattice parameters and see how the response in the magnetic moments is.

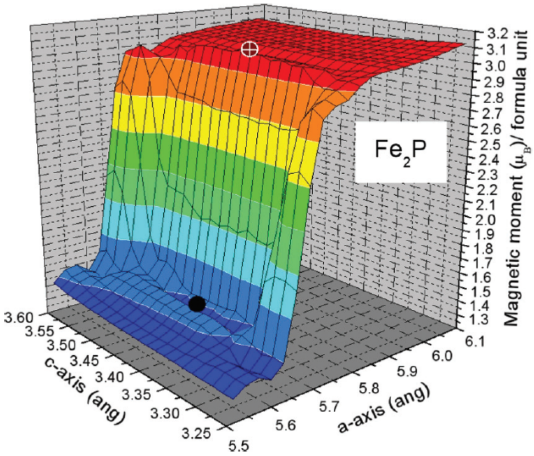

Figure 3.5: Total magnetic moment per formula unit as a function of lattice parameters a and c for Fe$_2$P. White and black dots indicate high and low magnetization states respectively. [30].

Magnetocaloric materials (first-order in particular) tend to exhibit a sharp change between two magnetic states when one or several lattice parameters are varied. For example Fe$_2$P-based materials show this behaviour for the a lattice parameter, as illustrated in Fig. 3.5. Along the c parameter the moment remains stable. A step in magnetization close to the equilibrium lattice parameter may indicate a magnetic instability and can be tied to the magnetocaloric performance. If a switch between magnetic states occurs near the transition, it will be accompanied by a lattice change and concomitant latent heat boosting the entropy change. As such, a strong magneto-elastic response may serve as an indicator of the first-order transition.

The magnetic response to deformation in lattice parameter l can be expressed as:

$$\gamma_l = \frac{\dfrac{\mu - \mu'}{\mu}}{\dfrac{l - l'}{l}} \tag{3.7}$$

Here μ is the total moment before deformation, μ' — after deformation and l' is the deformed lattice parameter l. The dimensionless parameter γ_l therefore represents the relative change in moment due to a relative change in lattice parameter.

To probe the magneto-elastic coupling for all lattice directions a fixed change in unit cell volume is applied by individually changing the independent lattice parameters (Fig. 3.6). During this process, the symmetry is preserved (*e.g* for cubic symmetry only one deformation is performed, but two for hexagonal). This results in a set of deformations in all non-symmetry equivalent directions. For each one γ_l is calculated. The overall magneto-elastic response is then estimated through the root mean square of responses to individual lattice deformations:

$$\gamma_M = \sqrt{\gamma_a^2 + \gamma_b^2 + \gamma_c^2} \tag{3.8}$$

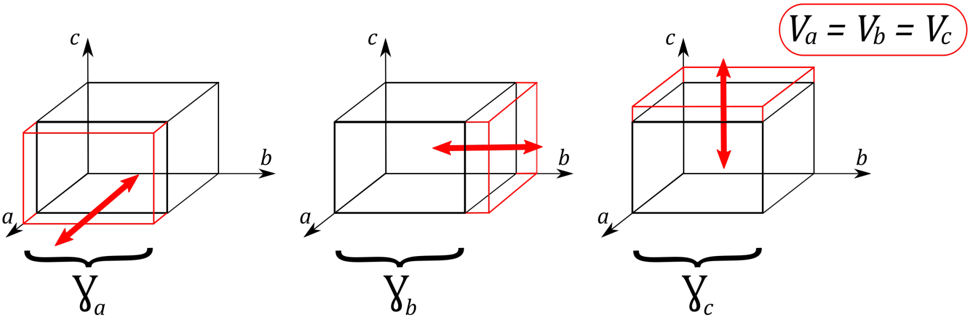

Figure 3.6: Schematic illustration of the applied deformations to compute γ_M for an orthorhombic lattice.

Additionally, the same approach is applied to the volumetric deformation. All lattice parameters are scaled simultaneously and the magnetic response is described with (3.7), where i and i' are replaced by V and V'. This produces an extra parameter to characterize the material in question. A weak isotropic and a strong anisotropic effect is favoured for cyclic applications.

Technical details of the calculation process of γ_M along with Python code can be found in appendix A.

Figure 3.7 shows the predictive capabilities of γ_M tested on a variety of known MCE materials. The dataset used for this plot is presented in table 3.1. The overall trend is apparent: materials with large MCE exhibit large values of γ_M. The correlation between a calculated number, such as γ_M and and actual MCE performance measured as ΔS can be estimated in several ways. Bocarsly *et al.* [25] applied Pearson's correlation (linear regression). While it is certainly useful to highlight the linear relationship observed for Σ_M, r is not an optimal metric for comparing such models due to a number of drawbacks. It is inappropriate for non-linear models; r depends on sample size and is extremely sensitive to outliers, especially in case of discontinuous or unbalanced distributions. It may not display meaningful fits in the case of unequal variability, when the least precise information may influence statistical estimate the most. The situation can be somewhat improved by using a weighted linear regression instead.

Several of the problems discussed above apply to the currently available data for the known magnetocaloric materials. While choosing the reference materials we attempted to provide a somewhat balanced set with values of ΔS spread equally over the whole range. Still, many known materials have ΔS in a similar range of 1–3 $\mathrm{J\,kg^{-1}\,K^{-1}}$ and substantially fewer demonstrate high values. To circumvent some of the pitfalls, Tantillo [27] suggests using the mean square error (*MSE*) instead of r. One of the advantages is that the *MSE* has the same units as the square of the target value so the degree of the model's accuracy is easier to understand. It is also applicable for non-linear dependencies. However, the *MSE* can get pronounced when the compared values are of significantly different magnitudes.

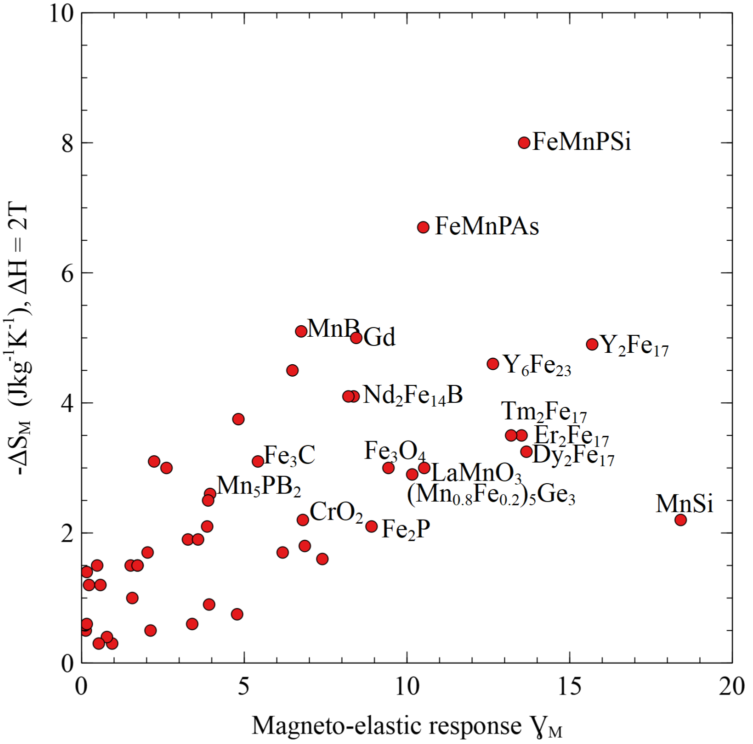

Figure 3.7: Comparison of the magneto-elastic response, γ_M, and experimental entropy change ΔS_M under an applied magnetic field change from 0 to 2 T.

To avoid this, a normalized mean square error should be used instead ($NMSE$):

$$NMSE = \frac{MSE}{\sigma^2} = \frac{\sum_{i=1}^{N}(P_i - O_i)^2}{N\sigma^2} \tag{3.9}$$

where P_i and O_i are the predicted and observed values, respectively, N is the total number of observations and σ is the standard deviation of the observed values:

$$\sigma = \sqrt{\frac{\sum_{i=1}^{N}(O_i - \overline{O})^2}{N}} \tag{3.10}$$

where $\overline{O}$ is the mean of the observed values.

An even better choice would be Spearman's correlation ρ. We expect that larger values of γ_M indicate larger ΔS_M. Fittingly, Spearman's correlation shows weather two properties are related as a monotonous function and it is far less influenced by the outliers. Spearman's correlation is obtained by calculating Pearson's correlation on the ranked values of the data. Ranking (from low to high) is defined by assigning a rank of 1 to the lowest value, 2 to the next lowest, *etc.*:

$$\rho = \frac{cov(R(P), R(O))}{\sigma_{R(P)}\sigma_{R(O)}} \tag{3.11}$$

where P and O are the predicted and observed values respectively, $cov(R(P), R(O))$ is the covariance of the rank variables and $\sigma_{R(P)}, \sigma_{R(O)}$ are the standard deviations of the rank variables.

Using these statistical tools on the data presented in in table 3.1 we get the following: r=0.77, ρ=0.78 and $NMSE$=6.63 $(\mathrm{J\,kg^{-1}\,K^{-1}})^2$.

γ_M successfully highlights materials with a GMCE and generally follows the linear trend across a variety of crystal systems and elemental compositions. The primary intention for the γ_M metric was to compare different systems, but it may serve just as effectively when investigating a single material family (*e.g* effect of different dopants on performance). This can be seen from the results for Fe_2P, FeMnPAs and FeMnPSi, where the progressive improvement of ΔS_M is properly represented by the γ_M values. The same applies to the (Ca,Nd)MnO_3 system.

The material with the largest deviation from the predictions, MnSi, is a useful example for two reasons. First, it gives awareness that γ_M alone may not be sufficient to characterize all magnetocaloric materials. The reason for the deviation from the trend in this case seems to lie with the fairly complicated magnetic structure of MnSi. Simply attempting to model it as a FM material apparently gives an overestimation of γ_M. MnSi is in fact a weakly first-order material [31], and γ_M reflects this. But due to the competition between FM, helical and PM phases, the first-order transition is easily suppressed by an applied magnetic field and overtaken by the second-order transition. Since such behaviour is not considered in our model, the prediction becomes inaccurate. This case is also an illustration of the proper choice of statistical parameters discussed earlier. It is not surprising that γ_M does not work on all types of magnetocaloric materials, yet for a significant group the correlation can be found. By removing this one point from the dataset r would grow to 0.82, which is not quite an accurate illustration of how well γ_M performs. On the other hand, ρ=0.79 is less influenced by the absence of a single exception in the dataset.

For the screening, the suggested acceptance limit for γ_M is ≥8.0. High values of γ_M are not a guarantee of a proportionally large ΔS, but do point to interesting material families. On the other hand, candidates with a low γ_M are far less likely to show a GMCE.

Table 3.1: Materials used for the comparison of the magneto-elastic response γ_M and the maximal isothermal entropy change ΔS_M upon application of a magnetic field of 2 T

Compound	γ_M	ΔS_M for $\Delta\mu_0 H$ = 2 T, $(\mathrm{J\,kg^{-1}\,K^{-1}})$	ref.
Fe_2P	8.91	2.1	[32]
FeMnPAs	10.5	6.7	[33]
FeMnPSi	13.6	8	[34]
YFe_2	0.13	0.5	[35]
Y_6Fe_{23}	12.64	4.6	[36]

(continued on next page)

Compound	γ_M	ΔS_M for $\Delta\mu_0 H = 2\,\mathrm{T}$, $(\mathrm{J\,kg^{-1}\,K^{-1}})$	ref.
Y_2Fe_{17}	15.69	4.9	[37]
Tm_2Fe_{17}	13.2	3.5	[38]
Dy_2Fe_{17}	13.67	3.25	[39]
Er_2Fe_{17}	13.52	3.5	[39]
$(Nd_{0.5}Pr_{0.5})Fe_{14}B$	8.36	4.1	[40]
$Nd_2Fe_{14}B$	8.2	4.1	[40]
$MnNi_2Ga$	1.72	1.5	[33]
$MnNi_2Sb$	0.11	0.58	[41]
$MnNi_2Sn$	0.58	1.2	[42]
MnNiSb	0.48	1.5	[42]
MnCoP	2.23	3.1	[42]
MnCoGe	2.61	3	[43]
Gd	8.44	5	[44]
Ni	0.16	1.4	[42]
CrO_2	6.8	2.2	[45]
Fe_5Si_3	1.56	1	[46]
Mn_5Ge_3	4.82	3.75	[47]
$(Mn_{0.8}Fe_{0.2})_5Ge_3$	10.16	2.9	[48]
$SrRuO_3$	3.4	0.6	[49]
$LaMnO_3$	10.53	3	[50]
La_2MnNiO_6	3.92	0.9	[50]
$(La_{0.75}Sr_{0.25})MnO_3$	0.23	1.2	[51]
$(Ca_{0.5}Nd)_{0.5}MnO_3$	0.94	0.3	[52]
$(Ca_{0.33}Nd_{0.66})MnO_3$	1.51	1.5	[52]
$(Ca_{0.25}Nd_{0.75})MnO_3$	3.86	2.1	[52]
Dy_2MnCoO_6	0.78	0.4	[53]
Gd_2MnCoO_6	2.12	0.5	[54]
$AlNi_2BO_5$	2.03	1.7	[55]
$HoMn_2O_5$	3.27	1.9	[56]
Fe_3O_4	9.43	3	[57]
$MnFe_2Si$	0.16	0.6	[58]
Fe_2MnGa	6.48	4.5	[59]
Mn_3AlC	7.4	1.6	[60]
MnP	6.86	1.8	[61]
MnB	6.75	5.1	[42]
FeB	6.18	1.7	[42]
MnSi	18.41	2.2	[31]
Mn_5PB_2	3.95	2.6	[62]
Mn_3GaC	3.89	2.5	[60]
Mn_3Sn2	3.58	1.9	[63]
MnFeGe	4.78	0.75	[43]
Fe_3C	5.42	3.1	[64]

(continued on next page)

Compound	γ_M	ΔS_M for $\Delta\mu_0 H = 2\,\mathrm{T}$, $(\mathrm{J\,kg^{-1}\,K^{-1}})$	ref.
$FeRu_2Sn$	0.53	0.3	[42]

3.5 Review of the material databases

The larger the starting dataset, the higher, the chances are to find a novel magnetocaloric material. Nevertheless, the choice of the source should be made with caution. The ease of access and the amount of information are of importance. For example, if the database already contains information about magnetism or phase stability, it can be used directly during screening, without any additional computational effort. Some databases offer a dedicated application programming interface (API), which significantly simplifies data acquisition and allows for complicated queries. The quality of the data is also of importance and well-curated commercial databases may prove to be more reliable. Table 3.2 provides a brief comparison of the largest material databases that are currently available. They can typically be divided into experimental ones, which contain reports from measurements, and computational databases that have been acquired from *ab-initio* calculations. The computational databases are often fully or partly based on experimental ones, but may also have data purely from modelling.

Commonly, experimental databases are not built with data mining in mind and are used for material identification instead. This makes it harder to add them to the screening process. On the other hand, this is well-compensated by the quality and reliability of data. All materials found in experimental databases can be manufactured and specific details are usually provided in the literature. Pearson's Crystal Data [65] is the largest commercial database, containing thousands of crystal structures. While it offers accurate information for a large number of materials, the proprietary software used to access it is unsuitable for automated data mining. For this reason, it was excluded from the current workflow. The high number of entries in the Crystallography Open Database (COD) [66] comes from a combination of inorganic and organic materials. The latter are of little use for MCE screening. This free database is open for access and uploads, but may potentially contain less reliable data. The Inorganic Crystal Structure Database (ICSD) [67] is another commercial experimental database (it also contains a minority of calculated compounds). Many computational databases are based on it to various degrees. The ICSD lacks a convenient API, but does offer the basic functionality to automatically sieve through it, based on certain parameters (composition, structure type, *etc.*).

Computational databases are well-suited for screening, both due to the convenience of access and a certain amount of pre-supplied information (*e.g.* magnetic properties). This occasionally comes at the cost of accuracy, yet these databases are constantly being updated and improved. AFLOWLIB [11, 68] is by far the largest available database, with over 3 million structures. This computational database is populated by iterating over ~1100 crystallographic prototypes and applying various possible combinations of elements to them. The resulting compounds are then modelled with DFT. This technique allows to predict many materials, but does not guarantee a high accuracy (or, in fact, the stability of the material). This is evident from Fig. 3.8. Magnetic moments reported in AFLOWLIB are significantly overestimated compared to experimental reports and our own calculations. Open Quantum Material Database (OQMD) [12] follows a similar approach to modelling of

Table 3.2: Overview of material databases.

	Databases	**# entries**	**Available information**	**Data mining capabilities**
Experimental	Pearson's CD	350,000	Structural data (CIF files)	-
	COD	402,604	Structural data (CIF files)	Database as a whole available for download
	ICSD	242,828	Structural data (unformatted)	Data can be queried through SQL commands. Custom scripts are required.
Computational	AFLOWLIB	3,541,633	Structural data (proprietary format) Magnetic moment Electronic properties	Intelligent query and download through AFLOWLIB RESTful API (python)
	MP	86,680	Structural data (VASP files) Magnetic moment Electronic properties Elastic tensors Phase stability	Intelligent query and download through Materials API (python)
	OQMD	815,654	Structural data (VASP files) Magnetic moment Electronic properties Phase stability	Intelligent query and download through OQMD RESTful API (python)
	JARVIS	55,286	Structural data (VASP files) Magnetic moment Electronic properties Elastic tensors	Intelligent query and download through JARVIS-API (python)

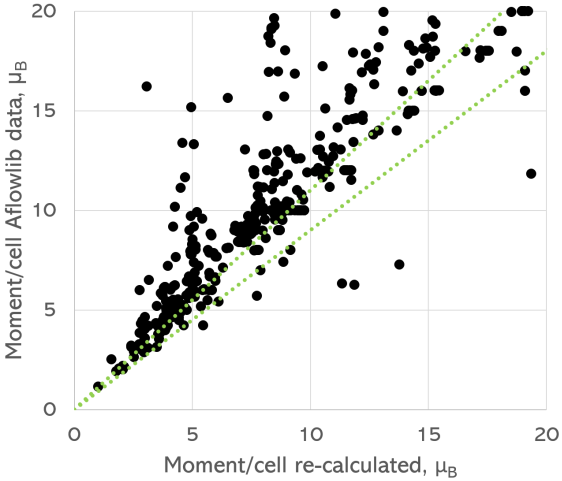

Figure 3.8: Comparison of the magnetic magnetic moments as-reported in AFLOWLIB and after an optimized calculation. Performed for 700 random structures from the database. Green doted lines indicate a 10% deviation.

the materials and shares similar disadvantages. Conversely, the Materials Project (MP) [10] is based on ICSD and curated user-generated results. It also provides a user-friendly API and many electronic (*e.g.* DOS) properties for each entry. Joint Automated Repository for Various Integrated Simulations (JARVIS) [69] created by NIST is effectively a subset of MP, but it compliments the original by adding more properties (like modelled XRD patterns) and a higher quality of calculations.

More than one database can be used for screening, as long as data are converted to the same standard and duplicate entries are handled properly. For the screening results reported in this work, MP and COD have been used as sources. At the time of writing the support for Aflowlib and ICSD has been fully implemented and the screening process is ongoing.

3.6 High-throughput workflow

Our approach combines the data mining of the structural databases with high-throughput computations to identify previously unrecognized materials for MCE applications. We suggest a workflow as displayed in Fig. 3.9 to sieve through thousands of materials reported in the material databases and single out the materials that can potentially exhibit a MCE, as well as provide a metric according to which the candidates can be compared. The proper order in which screening parameters are applied is important to reduce the overall time and effort of the process. The screening process starts with the selection of the databases. For the current example — MP and COD totalling 489,284 materials. By using the search tools offered by the databases and filtering by elements according to our “whitelist” and “blacklist” criteria the number is instantly reduced by 80%. At this stage, a local data table is populated with basic information available from the databases (composition, space group, unit cell volume, lattice parameters, literature references, *etc.*) –

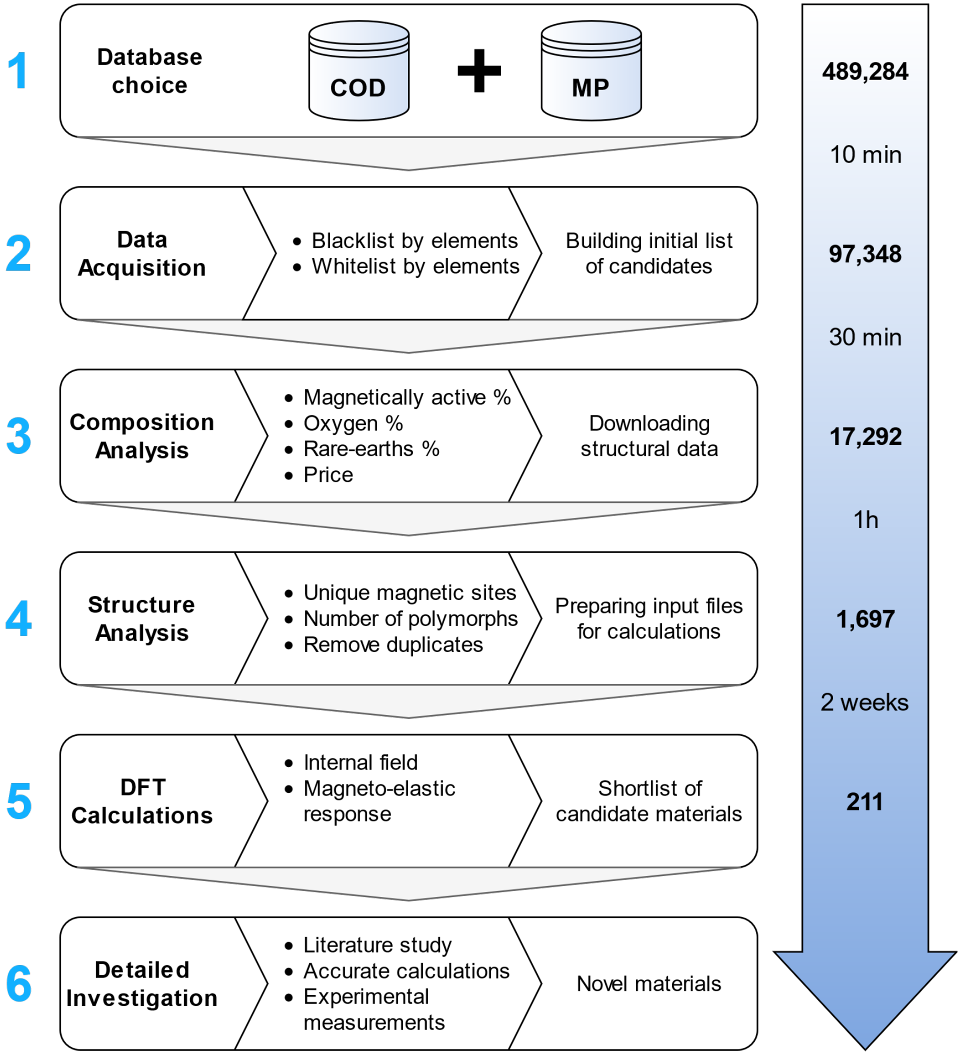

Figure 3.9: Scheme of the screening process.

any additional information that can be helpful for later analysis. Some variations in the data formatting from different databases are converted to uniform standards for ease of comparison. Next, the necessary information for further screening is gained by analyzing the chemical composition. After applying criteria based on the composition the list of candidates is reduced to just 4% of the starting number. At this stage, structure files are gathered from the databases and analysed. This step involves parsing a large number of individual files and requires more processing power, but nevertheless can be performed on a personal computer. Since databases inevitably contain a number of duplicate entries (usually due to different experimental or computational parameters applied to the same material) it is preferable to remove the chemically and structurally identical materials. The removal of duplicates comes at such a late step since it requires structural information for a proper comparison. With a sufficiently low number of the remaining candidates, DFT calculations can be employed to gather electronic and magnetic information. A set of checks for the high throughput calculations has been set up to guarantee that for each material all necessary computations are performed and reach sufficient accuracy. A routine has been developed to automatically run computations in batches and handle errors and attempt restarts. Once the computations are complete the two parameters – γ_M and internal field – that we use as main metrics for MCE can be deduced. Based on the above a shortlist of materials is generated. For each candidate, all the properties obtained during screening are stored to be used during the hands-on human investigation. As a final remark: while it is useful to have as many materials with good performance as possible, in practice, the candidates from the shortlist have to be manually investigated and prepared. Therefore, after the screening is finished the shortlist should not be overly long — well within a couple of hundred materials. This can be enforced by setting stricter criteria (internal field and γ_M) or adding more of them. The flexibility of the computational toolset makes it possible to easily build in additional screening parameters to further adjust or refine the search process. With the criteria discussed in 3 . 3, the final number comes to just 211 materials. If compounds are grouped into families of similar materials by ignoring slight variations in compositions the number is lowered to just 39 systems.

3.7 Computational details

For all materials, static calculations were performed with structures acquired from the databases, no additional structural optimization is performed. k-grids were automatically generated with the smallest allowed spacing between k-points of $0.5\,\text{Å}^{-1}$. The k-space integrations were performed with the Methfessel-Paxton method [70] of the second order with a smearing width of 0.2 eV and using the real space projectors. For total energies, the tolerance was set at 10 µeV. For each composition the kinetic energy cutoff was chosen as 1.3 times the highest default cutoff energy among individual constituent elements. For all compounds FM ordering is assumed. Initial magnetic moments, default cutoff energies and valence electrons for all individual elements used in the calculations can be found in appendix B.

3.8 Results and Discussion

The shortlist of materials is presented in table 3.3. The presence of known magnetocaloric materials (Fe_2P, Mn_5Si_3, MnPd, Y_2Fe17) in the shortlist demonstrates that our parameters of choice properly highlight candidates with MCE. Choosing which materials should be manufactured for further study requires quite a bit of decision making that has to be performed by a human expert. All the relevant information to help with this is saved during the screening process. For evaluation of the results at a glance, several types of plots can be used. The two parameters – internal field and γ_M that were used for screening can both be applied as a performance rating scale. By plotting the internal field against γ_M (Fig. 3.10) the most interesting candidates would be found in the top right corner.

A major improvement to the screening process would be the addition of computed

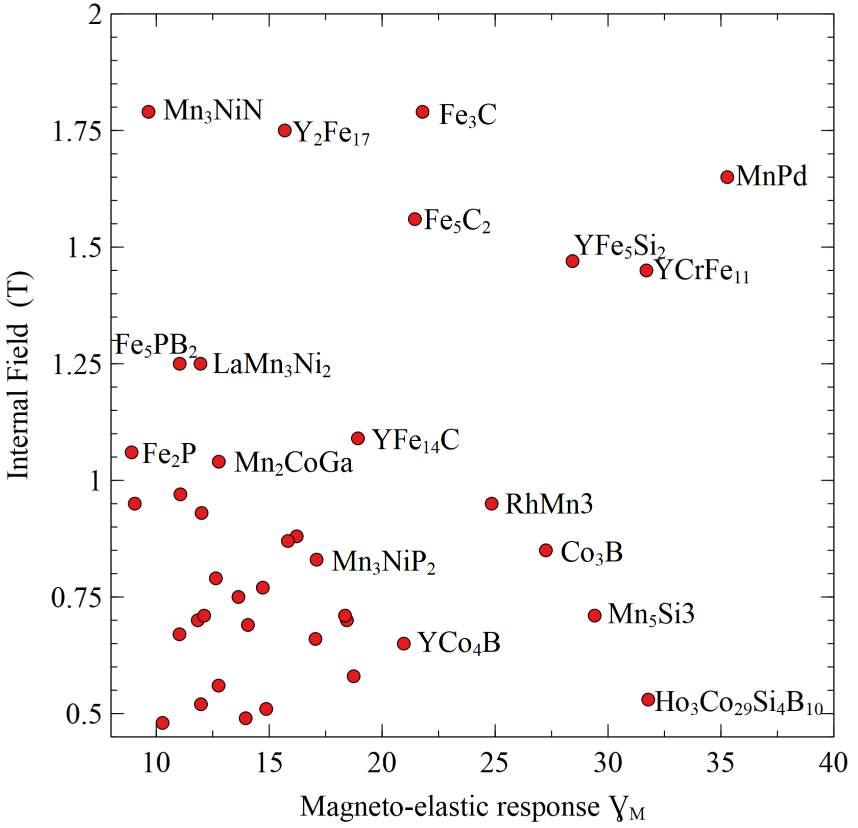

Figure 3.10: Evaluation plot for the final selection of candidates.

transition temperatures. To a certain extent information about the transition temperatures can be extracted from literature, but for many materials, it has not been reported yet or the sources report contradictory values. If this data is available another pair of evaluation plots can be used T_t vs γ_M and T_t vs the internal field. Here, materials with high γ_M and internal fields in the temperature range of interest would be selected. As the databases contain only specific reported structures, one can expect that the properties of the candidate can be further improved by adjusting the composition.

The current approach does have a couple of apparent drawbacks. Unfortunately, there is no easy way to guess the magnetic structure just from the chemical formula and crystal lattice. The method to do this exists and is discussed in [71]. But it involves a large number of additional calculations for each system, making it impractical for screening. For all our calculations we assume FM ordering, which is not for all materials correct. This assumption, therefore, leads to the presence of some false positives in the shortlist and we can expect materials with different types of magnetic transitions that are unlikely to contribute to a MCE among the results. For example, Y_6Mn_{23} found in the shortlist is known to have AFM order [72]. To mitigate this, the shortlist of candidates has to be investigated further, either through experiments or through calculations. Secondly, the screening parameter, γ_M is tailored to detect a magneto-elastic coupling. If the origin of MCE comes from electronic reconfiguration like in Eu_2In [73], the current parameter would not be of much use. Magnetocaloric materials with a similar mechanism will likely escape the search process, unless a suitable screening parameter is added to the process.

Despite this, even with the current setup computational screening makes it possible to sieve through thousands of known compounds without the need to perform time-consuming measurements and therefore can play an important role in guiding the search for novel magnetocaloric materials.

3.9 Conclusions

In silico methods offer a new way to discover and study materials. In this chapter, we describe an efficient workflow for a computer-assisted search for the new magnetocaloric materials. It relies heavily on readily available data from crystallographic databases. We suggest a number of criteria to distinguish materials that can have the potential for near room temperature refrigeration based solely on composition and structural information.

To predict the magnetocaloric performance we introduce a new computational metric – the magneto-elastic response γ_M. The magneto-elastic response is obtained for each candidate by modelling the magnetic moment of the material across a range of deformations. This parameter shows a good correlation with the ΔS_m measured in known magnetocaloric materials.

The flexibility of the computational toolset makes it possible to easily build in additional screening parameters to further adjust or refine the search process. A combination of fast initial screening based on database information with more accurate, computationally heavy assessments allows us to quickly process a large number of candidates and achieve a high accuracy of predictions for the final candidates.

The application of our workflow based on the information gathered from two crystallographic databases resulted in a list of materials with properties suitable for room temperature refrigeration.

Table 3.3: Materials suggested by the screening process.

Compound	lattice	Internal field, T	γ_M
$Mn_{17}Si_2C_4$	monoclinic	0.70	18.44
Fe_5C_2	monoclinic	1.56	21.45
Mn_3NiP_2	orthorhombic	0.83	17.10
$MnCrB_2$	orthorhombic	0.66	17.05
$YCrFe_{11}$	orthorhombic	1.45	31.70
$Mn_{23}(BC_2)_2$	orthorhombic	0.58	18.74
RhMnGe	orthorhombic	0.97	11.07
Mn_5CuN_4	orthorhombic	0.69	14.06
Mn_7GeN_6	orthorhombic	0.77	14.72

(continued on next page)

Compound	lattice	Internal field, T	γ_M
Fe_3C	orthorhombic	1.79	21.79
$Nb_2Mn_9Ge_8$	orthorhombic	0.93	12.01
Co_3B	orthorhombic	0.85	27.25
$ErFe_6Sn_6$	orthorhombic	0.67	11.03
Mn_5Si_3	orthorhombic	0.71	29.41
$Y(Fe_5Si)_2$	orthorhombic	1.47	28.43
Mn_5Si_2	tetragonal	0.56	12.76
MnPd	tetragonal	1.65	35.28
$Ho_3Co_{29}Si_4B_{10}$	tetragonal	0.53	31.78
$Y_2Fe_{14}C$	tetragonal	1.09	18.93
Fe_5B_2P	tetragonal	1.25	11.04
Fe_7Mo_6	trigonal	0.52	11.98
$TbCo_2$	trigonal	0.48	10.28
$Yb_2Mn_{12}P_7$	hexagonal	0.88	16.22
Fe_2P	hexagonal	1.06	8.91
CrNiP	hexagonal	0.51	14.87
$LaMn_3Ni_2$	hexagonal	1.25	11.96
YCo_4B	hexagonal	0.65	20.96
Fe_2Ti	hexagonal	0.87	15.83
$TmMn_2$	hexagonal	0.49	13.96
Y_2Fe17	hexagonal	1.75	15.69
MnNiSi	hexagonal	0.75	13.64
MnCoSi	hexagonal	0.95	9.05
$RhMn_3$	cubic	0.95	24.85
Co3Ti	cubic	0.71	18.36
MnCoGa2	cubic	0.70	11.84
Y_6Mn_{23}	cubic	0.79	12.64
$HoMn_2$	cubic	0.71	12.12
Mn_3NiN	cubic	1.79	9.66
Mn_2CoGa	cubic	1.04	12.77

REFERENCES

[1] J. Greeley, T. F. Jaramillo, J. Bonde, I. Chorkendorff, and J. K. Nørskov. "Computational high-throughput screening of electrocatalytic materials for hydrogen evolution". In: *Nat. Mater.* 5.11 (Nov. 2006), pp. 909–913. DOI: `10.1038/nmat1752`.

[2] G. Ceder, Y.-M. Chiang, D. R. Sadoway, M. K. Aydinol, Y.-I. Jang, and B. Huang. "Identification of cathode materials for lithium batteries guided by first-principles calculations". In: *Nature* 392.6677 (Apr. 1998), pp. 694–696. DOI: `10.1038/33647`.

[3] R. Li, X. Li, L. Xi, J. Yang, D. J. Singh, and W. Zhang. "High-Throughput Screening for Advanced Thermoelectric Materials: Diamond-Like ABX_2 Compounds". In: *ACS Appl. Mater. Interfaces* 11.28 (July 2019), pp. 24859–24866. DOI: `10.1021/acsami.9b01196`.

[4] L. Vitos, P. A. Korzhavyi, and B. Johansson. "Stainless steel optimization from quantum mechanical calculations". In: *Nat. Mater.* 2.1 (Jan. 2003), pp. 25–28. DOI: `10.1038/nmat790`.

[5] D. Goll, R. Loeffler, J. Herbst, R. Karimi, and G. Schneider. "High-throughput search for new permanent magnet materials". In: *J. Phys. Condens. Matter* 26.6 (Feb. 2014), p. 064208. DOI: `10.1088/0953-8984/26/6/064208`.

[6] A. Vishina, O. Y. Vekilova, T. Björkman, A. Bergman, H. C. Herper, and O. Eriksson. "High-throughput and data-mining approach to predict new rare-earth free permanent magnets". In: *Phys. Rev. B* 101.9 (Mar. 2020), p. 094407. DOI: `10.1103/PhysRevB.101.094407`.

[7] H. Zhang. "High-throughput Design of Magnetic Materials". In: *Electron. Struct.* (Sept. 2020). DOI: `10.1088/2516-1075/abbb25`.

[8] K. Mathew, J. H. Montoya, A. Faghaninia, S. Dwarakanath, M. Aykol, H. Tang, I.-h. Chu, T. Smidt, B. Bocklund, M. Horton, J. Dagdelen, B. Wood, Z.-K. Liu, J. Neaton, S. P. Ong, K. Persson, and A. Jain. "Atomate: A high-level interface to generate, execute, and analyze computational materials science workflows". In: *Comput. Mater. Sci.* 139 (Nov. 2017), pp. 140–152. DOI: `10.1016/j.commatsci.2017.07.030`.

[9] S. P. Huber, S. Zoupanos, M. Uhrin, L. Talirz, L. Kahle, R. Häuselmann, D. Gresch, T. Müller, A. V. Yakutovich, C. W. Andersen, F. F. Ramirez, C. S. Adorf, F. Gargiulo, S. Kumbhar, E. Passaro, C. Johnston, A. Merkys, A. Cepellotti, N. Mounet, N. Marzari, B. Kozinsky, and G. Pizzi. "AiiDA 1.0, a scalable computational infrastructure for automated reproducible workflows and data provenance". In: *Sci. Data* 7.1 (Dec. 2020), p. 300. DOI: `10.1038/s41597-020-00638-4`.

[10] A. Jain, S. P. Ong, G. Hautier, W. Chen, W. D. Richards, S. Dacek, S. Cholia, D. Gunter, D. Skinner, G. Ceder, and K. A. Persson. "Commentary: The Materials Project: A materials genome approach to accelerating materials innovation". In: *APL Mater.* 1.1 (July 2013), p. 011002. DOI: `10.1063/1.4812323`.

[11] S. Curtarolo, W. Setyawan, S. Wang, J. Xue, K. Yang, R. H. Taylor, L. J. Nelson, G. L. Hart, S. Sanvito, M. Buongiorno-Nardelli, N. Mingo, and O. Levy. "AFLOWLIB.ORG: A distributed materials properties repository from high-throughput ab initio calculations". In: *Comput. Mater. Sci.* 58 (June 2012), pp. 227–235. DOI: `10.1016/j.commatsci.2012.02.002`.

[12] S. Kirklin, J. E. Saal, B. Meredig, A. Thompson, J. W. Doak, M. Aykol, S. Rühl, and C. Wolverton. "The Open Quantum Materials Database (OQMD): assessing the accuracy of DFT formation energies". In: *npj Comput. Mater.* 1.1 (Dec. 2015), p. 15010. DOI: `10.1038/npjcompumats.2015.10`.

[13] J. Xiong, T. Zhang, and S. Shi. "Machine learning of mechanical properties of steels". In: *Sci. China Technol. Sci.* 63.7 (July 2020), pp. 1247–1255. DOI: `10.1007/s11431-020-1599-5`.

[14] A. G. Kusne, T. Gao, A. Mehta, L. Ke, M. C. Nguyen, K.-M. Ho, V. Antropov, C.-Z. Wang, M. J. Kramer, C. Long, and I. Takeuchi. "On-the-fly machine-learning for high-throughput experiments: search for rare-earth-free permanent magnets". In: *Sci. Rep.* 4.1 (May 2015), p. 6367. DOI: `10.1038/srep06367`.

[15] C. Ortiz, O. Eriksson, and M. Klintenberg. "Data mining and accelerated electronic structure theory as a tool in the search for new functional materials". In: *Comput. Mater. Sci.* 44.4 (Feb. 2009), pp. 1042–1049. DOI: `10.1016/j.commatsci.2008.07.016`.

[16] L. Ghadbeigi, T. D. Sparks, J. K. Harada, and B. R. Lettiere. "Data-mining approach for battery materials". In: *2015 IEEE Conf. Technol. Sustain.* IEEE, July 2015, pp. 239–244. DOI: `10.1109/SusTech.2015.7314353`.

[17] D. Liu, K. Guo, F. Tang, F. Mao, X. Liu, C. Hou, H. Wang, H. Lu, and X. Song. "Selecting Doping Elements by Data Mining for Advanced Magnets". In: *Chem. Mater.* 31.24 (Dec. 2019), pp. 10117–10125. DOI: `10.1021/acs.chemmater.9b03379`.

[18] N. A. Zarkevich, D. D. Johnson, and V. K. Pecharsky. "High-throughput search for caloric materials: the CaloriCool approach". In: *J. Phys. D. Appl. Phys.* 51.2 (Jan. 2018), p. 024002. DOI: `10.1088/1361-6463/aa9bd0`.

[19] B. Zhang, X.-Q. Zheng, T.-Y. Zhao, F.-X. Hu, J.-R. Sun, and B.-G. Shen. "Machine learning technique for prediction of magnetocaloric effect in La(Fe,Si/Al)$_{13}$ -based materials". In: *Chinese Phys. B* 27.6 (June 2018), p. 067503. DOI: `10.1088/1674-1056/27/6/067503`.

[20] Y. Zhang and X. Xu. "Machine learning the magnetocaloric effect in manganites from compositions and structural parameters". In: *AIP Adv.* 10.3 (Mar. 2020), p. 035220. DOI: `10.1063/1.5144241`.

[21] Y. Zhang and X. Xu. "Machine learning the magnetocaloric effect in manganites from lattice parameters". In: *Appl. Phys. A* 126.5 (May 2020), p. 341. DOI: `10.1007/s00339-020-03503-8`.

[22] D. Tu, J. Yan, Y. Xie, J. Li, S. Feng, M. Xia, J. Li, and A. P. Leung. "Accelerated design for magnetocaloric performance in Mn-Fe-P-Si compounds using machine learning". In: *J. Mater. Sci. Technol.* 96 (Jan. 2022), pp. 241–247. DOI: `10.1016/j.jmst.2021.03.082`.

[23] P. B. de Castro, K. Terashima, T. D. Yamamoto, Z. Hou, S. Iwasaki, R. Matsumoto, S. Adachi, Y. Saito, P. Song, H. Takeya, and Y. Takano. "Machine-learning-guided discovery of the gigantic magnetocaloric effect in HoB_2 near the hydrogen liquefaction temperature". In: *NPG Asia Mater.* 12.1 (Dec. 2020), p. 35. DOI: `10.1038/s41427-020-0214-y`.

[24] J. Nelson and S. Sanvito. "Predicting the Curie temperature of ferromagnets using machine learning". In: *Phys. Rev. Mater.* 3.10 (Oct. 2019), p. 104405. DOI: `10.1103/PhysRevMaterials.3.104405`.

[25] J. D. Bocarsly, E. E. Levin, C. A. C. Garcia, K. Schwennicke, S. D. Wilson, and R. Seshadri. "A Simple Computational Proxy for Screening Magnetocaloric Compounds". In: *Chem. Mater.* 29.4 (Feb. 2017), pp. 1613–1622. DOI: `10.1021/acs.chemmater.6b04729`.

[26] C. A. C. Garcia, J. D. Bocarsly, and R. Seshadri. "Computational screening of magnetocaloric alloys". In: *Phys. Rev. Mater.* 4.2 (Feb. 2020), p. 024402. DOI: `10.1103/PhysRevMaterials.4.024402`.

[27] A. Tantillo. "Optimization of Materials for Magnetic Refrigeration and Thermomagnetic Power Generation". PhD thesis. The City University of New York, 2021.

[28] H. Yamada and T. Goto. "Itinerant-electron metamagnetism and giant magnetocaloric effect". In: *Phys. Rev. B* 68.18 (Nov. 2003), p. 184417. DOI: `10.1103/PhysRevB.68.184417`.

[29] R. M. Vieira, O. Eriksson, A. Bergman, and H. Herper. "High-throughput compatible approach for entropy estimation in magnetocaloric materials: FeRh as a test case". In: *J. Alloys Compd.* 857 (Mar. 2021), p. 157811. DOI: `10.1016/j.jallcom.2020.157811`.

[30] Z. Gercsi, E. K. Delczeg-Czirjak, L. Vitos, A. S. Wills, A. Daoud-Aladine, and K. G. Sandeman. "Magnetoelastic effects in doped Fe_2P". In: *Phys. Rev. B* 88.2 (July 2013), p. 024417. DOI: `10.1103/PhysRevB.88.024417`.

[31] P. Arora, M. K. Chattopadhyay, and S. B. Roy. "Magnetocaloric effect in MnSi". In: *Appl. Phys. Lett.* 91.6 (Aug. 2007), p. 062508. DOI: `10.1063/1.2768005`.

[32] L. Caron, M. Hudl, V. Höglin, N. H. Dung, C. P. Gomez, M. Sahlberg, E. Brück, Y. Andersson, and P. Nordblad. "Magnetocrystalline anisotropy and the magnetocaloric effect in Fe_2P". In: *Phys. Rev. B - Condens. Matter Mater. Phys.* 88.9 (Sept. 2013), p. 094440. DOI: `10.1103/PhysRevB.88.094440`. arXiv: `1307.2784`.

[33] O. Tegus, E. Brück, L. Zhang, Dagula, K. H. Buschow, and F. R. De Boer. "Magnetic-phase transitions and magnetocaloric effects". In: *Phys. B Condens. Matter* 319.1-4 (July 2002), pp. 174–192. DOI: `10.1016/S0921-4526(02)01119-5`.

[34] K. Katagiri, K. Nakamura, and H. Wada. "Magnetocaloric properties and magnetic refrigerant capacity of $MnFeP_{1-x}Si_x$". In: *J. Alloys Compd.* 553 (Mar. 2013), pp. 286–290. DOI: `10.1016/j.jallcom.2012.11.127`.

[35] N. A. De Oliveira. "Magnetocaloric effect in systems of itinerant electrons: Application to Fe, Co, Ni, YFe_2 and YFe_3 compounds". In: *J. Alloys Compd.* 403.1-2 (Nov. 2005), pp. 45–48. DOI: `10.1016/j.jallcom.2005.05.014`.

[36] B. R. Hansen. "Materials for Room Temperature Magnetic Refrigeration". PhD thesis. Technical University of Denmark, 2010.

[37] J. L. Sánchez Llamazares, P. Álvarez-Alonso, C. F. Sánchez-Valdés, P. J. Ibarra-Gaytán, J. A. Blanco, and P. Gorria. "Investigating the magnetic entropy change in single-phase Y_2Fe_{17} melt-spun ribbons". In: *Curr. Appl. Phys.* 16.9 (Sept. 2016), pp. 963–968. DOI: `10.1016/j.cap.2016.05.013`.

[38] A. G. Kuchin, W. Iwasieczko, and S. P. Platonov. "The magnetocaloric effect in R_2Fe_{17} intermetallics with different types of magnetic phase transition". In: *Low Temp. Phys.* 41.12 (Dec. 2015), pp. 985–989. DOI: `10.1063/1.4938182`.

[39] A. Nagy, S. H. Aly, S. Yehia, and T. Hammad. "Thermomagnetic Properties and Magnetocaloric Effect of $R_2Fe_{17}C$ (R=Dy, Nd, Tb, Gd, Pr, Ho, Er) Compounds". In: *Int. J. Comput. Phys. Ser.* 1.1 (Mar. 2018), pp. 268–278. DOI: `10.29167/A1I1P268-278`.

[40] I. Tereshina, T. Kaminskaya, L. Ivanov, G. Politova, H. Drulis, D. Gorbunov, M. Paukov, E. Tereshina-Chitrova, and A. Andreev. "Structural, magnetic and magnetocaloric properties of $NdPrFe_{14}B$ and its hydrides". In: *J. Phys. Conf. Ser.* Vol. 1389. 1. IOP Publishing, 2019, p. 12094. DOI: `10.1088/1742-6596/1389/1/012094`.

[41] E. E. Levin, J. D. Bocarsly, K. E. Wyckoff, T. M. Pollock, and R. Seshadri. "Tuning the magnetocaloric response in half-Heusler/Heusler $MnNi_{1+x}Sb$ solid solutions". In: *Phys. Rev. Mater.* 1.7 (Dec. 2017), p. 075003. DOI: `10.1103/PhysRevMaterials.1.075003`.

[42] J. D. Bocarsly, E. E. Levin, C. A. Garcia, K. Schwennicke, S. D. Wilson, and R. Seshadri. "A Simple Computational Proxy for Screening Magnetocaloric Compounds". In: *Chem. Mater.* 29.4 (Feb. 2017), pp. 1613–1622. DOI: `10.1021/acs.chemmater.6b04729`.

[43] S. Lin, O. Tegus, E. Brück, W. Dagula, T. Gortenmulder, and K. Buschow. "Structural and Magnetic Properties of $MnFe_{1-x}Co_xGe$ Compounds". In: *IEEE Trans. Magn.* 42.11 (Nov. 2006), pp. 3776–3778. DOI: `10.1109/TMAG.2006.884516`.

[44] S. Y. Dan'kov, A. Tishin, V. Pecharsky, and K. Gschneidner. "Magnetic phase transitions and the magnetothermal properties of gadolinium". In: *Phys. Rev. B - Condens. Matter Mater. Phys.* 57.6 (Feb. 1998), pp. 3478–3490. DOI: `10.1103/PhysRevB.57.3478`.

[45] X. Zhang, Y. Chen, L. Lü, and Z. Li. "A potential oxide for magnetic refrigeration application: CrO_2 particles". In: *J. Phys. Condens. Matter* 18.44 (Nov. 2006), pp. 559–566. DOI: `10.1088/0953-8984/18/44/L01`.

[46] Songlin, Dagula, O. Tegus, E. Brück, J. C. Klaasse, F. R. De Boer, and K. H. Buschow. "Magnetic phase transition and magnetocaloric effect in $Mn_{5-x}Fe_xSi_3$". In: *J. Alloys Compd.* 334.1-2 (Feb. 2002), pp. 249–252. DOI: `10.1016/S0925-8388(01)01776-5`.

[47] S. Songlin, D. Dagula, O. Tegus, E. Brück, F. R. De Boer, and K. H. Buschow. "Magnetic and magnetocaloric properties of $Mn_5Ge_{3-x}Sb_x$". In: *J. Alloys Compd.* 337.1-2 (May 2002), pp. 269–271. DOI: `10.1016/S0925-8388(01)01935-1`.

[48] M. Halder, S. M. Yusuf, and A. K. Nigam. "Magnetocaloric effect and its implementation in critical behavior study of $Mn_4FeGe_{3-x}Si_x$ intermetallic compounds". In: *J. Appl. Phys.* 110.11 (Dec. 2011), p. 113915. DOI: `10.1063/1.3669390`.

[49] A. Mackenzie, J. Bruin, R. Borzi, A. Rost, and S. Grigera. "Quantum criticality and the formation of a putative electronic liquid crystal in $Sr_3Ru_2O_7$". In: *Phys. C Supercond.* 481 (Nov. 2012), pp. 207–214. DOI: `10.1016/j.physc.2012.04.018`.

[50] M. Balli, P. Fournier, S. Jandl, and M. M. Gospodinov. "A study of the phase transition and magnetocaloric effect in multiferroic La_2MnNiO_6 single crystals". In: *J. Appl. Phys.* Vol. 115. 17. American Institute of Physics Inc., May 2014, p. 173904. DOI: `10.1063/1.4874943`.

[51] Z. B. Guo, W. Yang, Y. T. Shen, and Y. W. Du. "Magnetic entropy change in $La_{0.75}Ca_{0.25-x}Sr_xMnO_3$ perovskites". In: *Solid State Commun.* 105.2 (Jan. 1998), pp. 89–92. DOI: `10.1016/S0038-1098(97)10064-3`.

[52] A. Beiranvand, J. Tikkanen, J. Rautakoski, H. Huhtinen, and P. Paturi. "Estimates of the magnetocaloric effect in (Nd,Ca)MnO_3 and (Gd,Ca)MnO_3 based on magnetic transition entropies". In: *Mater. Res. Express* 4.3 (Mar. 2017), p. 036101. DOI: `10.1088/2053-1591/aa5fc9`.

[53] C. Ganeshraj, R. Pradheesh, and P. N. Santhosh. "Structural, magnetic, transport and magnetocaloric properties of metamagnetic $DyMn_{0.5}Co_{0.5}O_3$". In: *J. Appl. Phys.* Vol. 111. 7. American Institute of PhysicsAIP, Apr. 2012, 07A914. DOI: `10.1063/1.3672067`.

[54] J. Y. Moon, M. K. Kim, Y. J. Choi, and N. Lee. "Giant Anisotropic Magnetocaloric Effect in Double-perovskite Gd_2CoMnO_6 Single Crystals". In: *Sci. Rep.* 7.1 (Dec. 2017), p. 16099. DOI: `10.1038/s41598-017-16416-z`.

[55] J. Kumar, D. J. Mukkattukavil, A. Bhattacharyya, and S. Nair. "Investigations of the heterometallic ludwigite Ni_2AlBO_5". In: *J. Phys. Condens. Matter* 32.6 (Feb. 2020), p. 065601. DOI: `10.1088/1361-648X/ab4f5c`.

[56] H. Ge, X. Q. Zhang, Y. J. Ke, J. L. Jin, Z. X. Liao, and Z. H. Cheng. "Large reversible magnetocaloric effect in HoMn2O5". In: *Chinese Phys. B* 22.5 (May 2013), pp. 57502–057502. DOI: `10.1088/1674-1056/22/5/057502`.

[57] M. Bohra and S. C. Sahoo. "Large magnetocaloric effect at Verwey point in nanocrystalline Fe_3O_4 thin films". In: *J. Alloys Compd.* 699 (Mar. 2017), pp. 1118–1121. DOI: `10.1016/j.jallcom.2017.01.013`.

[58] I. Anikina. "The magnetocaloric effect $MnFe_2Si$ alloy, doped Cr and Fe". MA thesis. Russia: Ural Federal University, 2015.

[59] C. Yegin. “Magneto-Thermo-Mechanical Response and Magneto-Caloric Effect in Magnetic Shape Memory Alloys”. PhD thesis. 2012.

[60] P. Tong, B.-S. Wang, and Y.-P. Sun. “Mn-based antiperovskite functional materials: Review of research”. In: *Chinese Phys. B* 22.6 (June 2013), p. 067501. DOI: `10.1088/1674-1056/22/6/067501`.

[61] R. A. Booth and S. A. Majetich. “Crystallographic orientation and the magnetocaloric effect in MnP”. In: *J. Appl. Phys.* 105.7 (Apr. 2009), 07A926. DOI: `10.1063/1.3072022`.

[62] Z. G. Xie, D. Y. Geng, and Z. D. Zhang. “Reversible room-temperature magnetocaloric effect in Mn_5PB_2”. In: *Appl. Phys. Lett.* 97.20 (Nov. 2010), p. 202504. DOI: `10.1063/1.3518064`.

[63] Q. Recour, T. Mazet, and B. Malaman. “Magnetocaloric properties of Mn_3Sn_2 from heat capacity measurements”. In: *J. Appl. Phys.* 105.3 (Feb. 2009), p. 033905. DOI: `10.1063/1.3074093`.

[64] B. Kaeswurm, K. Friemert, M. Gürsoy, K. Skokov, and O. Gutfleisch. “Direct measurement of the magnetocaloric effect in cementite”. In: *J. Magn. Magn. Mater.* 410 (July 2016), pp. 105–108. DOI: `10.1016/j.jmmm.2016.02.080`.

[65] P. Villars and K. Cenzual. *Pearson’s Crystal Data: Crystal Structure Database for Inorganic Compounds.*

[66] S. Gražulis, D. Chateigner, R. T. Downs, A. F. T. Yokochi, M. Quirós, L. Lutterotti, E. Manakova, J. Butkus, P. Moeck, and A. Le Bail. “Crystallography Open Database – an open-access collection of crystal structures”. In: *J. Appl. Crystallogr.* 42.4 (Aug. 2009), pp. 726–729. DOI: `10.1107/S0021889809016690`.

[67] G. Bergerhoff, R. Hundt, R. Sievers, and I. D. Brown. “The inorganic crystal structure data base”. In: *J. Chem. Inf. Comput. Sci.* 23.2 (May 1983), pp. 66–69. DOI: `10.1021/ci00038a003`.

[68] C. E. Calderon, J. J. Plata, C. Toher, C. Oses, O. Levy, M. Fornari, A. Natan, M. J. Mehl, G. Hart, M. Buongiorno Nardelli, and S. Curtarolo. “The AFLOW standard for high-throughput materials science calculations”. In: *Comput. Mater. Sci.* 108 (Oct. 2015), pp. 233–238. DOI: `10.1016/j.commatsci.2015.07.019`.

[69] K. Choudhary, K. F. Garrity, A. C. E. Reid, B. DeCost, A. J. Biacchi, A. R. Hight Walker, Z. Trautt, J. Hattrick-Simpers, A. G. Kusne, A. Centrone, A. Davydov, J. Jiang, R. Pachter, G. Cheon, E. Reed, A. Agrawal, X. Qian, V. Sharma, H. Zhuang, S. V. Kalinin, B. G. Sumpter, G. Pilania, P. Acar, S. Mandal, K. Haule, D. Vanderbilt, K. Rabe, and F. Tavazza. “The joint automated repository for various integrated simulations (JARVIS) for data-driven materials design”. In: *npj Comput. Mater.* 6.1 (Dec. 2020), p. 173. DOI: `10.1038/s41524-020-00440-1`.

[70] M. Methfessel and A. T. Paxton. “High-precision sampling for Brillouin-zone integration in metals”. In: *Phys. Rev. B* 40.6 (Aug. 1989), pp. 3616–3621. DOI: `10.1103/PhysRevB.40.3616`.

[71] M. K. Horton, J. H. Montoya, M. Liu, and K. A. Persson. “High-throughput prediction of the ground-state collinear magnetic order of inorganic materials using Density Functional Theory”. In: *npj Comput. Mater.* 5.1 (Dec. 2019), p. 64. DOI: `10.1038/s41524-019-0199-7`.

[72] S. Kilcoyne and M. Telling. “Magnetic order in $Y_6(Mn_{1-x}Fe_x)_{23}$”. In: *J. Magn. Magn. Mater.* 140-144 (Feb. 1995), pp. 871–872. DOI: `10.1016/0304-8853(94)00838-8`.

[73] F. Guillou, A. K. Pathak, D. Paudyal, Y. Mudryk, F. Wilhelm, A. Rogalev, and V. K. Pecharsky. “Non-hysteretic first-order phase transition with large latent heat and giant low-field magnetocaloric effect”. In: *Nat. Commun.* 9.1 (Dec. 2018), p. 2925. DOI: `10.1038/s41467-018-05268-4`.

4

EFFECT OF DOPING ON (FE,MN)(P,SI) COMPOUNDS

"I almost wish I hadn't gone down that rabbit-hole — and yet — and yet — it's rather curious, you know, this sort of life!"

— Lewis Carroll

The physical properties of the extensively studied Fe_2P *material family, well-known for its promising magnetocaloric qualities, are greatly influenced by the unit-cell parameters of this hexagonal system. This sensitivity of the various magnetocaloric properties to structural parameters is particularly important for developing a material suitable for room-temperature magnetic refrigeration. In this chapter, various potential dopants for (Fe,Mn)(P,Si) compounds are studied by means of first-principles calculations. Detailed investigation of the effects of Li doping on the magnetic properties of the material reveals a strong correlation between changes in structural parameters induced by the introduction of Li and magnetic transition temperatures.*

4.1 Introduction

Many theoretical and experimental studies on Fe_2P based compounds were reported over the past decades [1–3]. These materials remain, along with $La(Fe,Co,Si)_{13}$ and $La(Fe,Mn,Si)_{13}H$, among the most promising candidates for room temperature magnetic refrigeration. Among the definite advantages of the Fe_2P family are a small hysteresis, a large adiabatic temperature change and a high magnetic entropy change, as well as the possibility to tune the ferromagnetic (FM) to paramagnetic (PM) transition temperature by varying the composition of the material [4, 5].

The ability to fine-tune T_C is especially important for practical applications, both for cooling and energy conversion purposes. The magnetic and magnetocaloric properties of these materials are heavily influenced by the lattice parameters [6].

Fe_2P exhibits mixed magnetism [7]. Recent measurements indicate magnetic moments of $2.05\,\mu_B$ and $0.8\,\mu_B$ at 10 K [8]. The exchange interaction varies greatly for different Fe-Fe pairs, depending on the distances between the respective atoms. This, in combination with the fact that the strongly magnetic sublattice enhances the weaker magnetic sublattice, leads to a large sensitivity of the magnetism to structural changes.

A variety of dopants have been investigated, both with experimental and computational techniques (Tab. 4.1), with the aim to optimize the performance for magnetocaloric applications. Notably, substitutions and additions of elements such as Si, As, B [9–11] allow to control T_C in this material system, while maintaining the optimal magnetization. These theoretical and experimental studies show that a decrease in the c/a ratio causes an upward shift of T_C.

Table 4.1: List of dopants for Fe_2P-based materials with reported results of theoretical calculations or experimental measurements.

Dopant	Theory (DFT)	Experiment
Co	$Mn_1Fe_{1-x}Co_xP_{0.5}Si_{0.5}$ [12]	$Mn_1Fe_{0.95-z}Ni_zP_{0.51}Si_{0.45}B_{0.04}$ [13]
Cu	$Mn_1Fe_{1-x}Cu_xP_{0.5}Si_{0.5}$ [12]	–
Ni	$Mn_1Fe_{1-x}Ni_xP_{0.5}Si_{0.5}$ [12]	$Mn_1Fe_{0.95-z}Ni_zP_{0.51}Si_{0.45}B_{0.04}$ [13]
Cr	$Mn_1Fe_{1-x}Cr_xP_{0.5}Si_{0.5}$ [12]	–
B	$Mn_1Fe_1P_{0.66-y}B_ySi_{0.33}$ [12] $Fe_2P_{1-x}B_x$ [11]	$Mn_1Fe_1P_{0.5}Si_{0.5}B_z$ [14] $Fe_2P_{1-z}B_z$ [15]
N	–	$Mn_{1.25}Fe_{0.7}P_{0.5}Si_{0.5}N_z$ [16]
C	–	$Mn_{1.15}Fe_{0.78}P_{0.5}Si_{0.5}C_z$ [17]
V	–	$Mn_{1.2-x}V_xFe_{0.75}P_{0.5}Si_{0.5}$ [18]
Ga	$Fe_2P_{1-x}Ga_x$ [19]	–
Ge	$Fe_2P_{1-x}Ge_x$ [19]	$Mn_xFe_{2-x}P_{1-y}Ge_y$ [20]
Si	$Fe_2P_{1-x}Si_x$ [11]	$Fe_2P_{1-x}Si_x$ [21]
As	$Fe_2P_{1-x}As_x$ [11]	$Fe_2P_{1-x}As_x$ [22]

In this work, a number of elements from the first four periods are examined as potential dopants for Fe_2P and $MnFeP_{0.66}Si_{0.33}$ based compounds. Doping possibility, site preferences and changes to magnetization and structure are obtained with *ab-initio* calculations. In the second part of this chapter the effect of Li doping on structure, magnetization and Curie temperature are investigated in detail.

4.2 Computational and experimental details

The DFT calculations described in 2.4 were performed with VASP package. The k-space integrations were performed with the Methfessel-Paxton method [23] of second order with a smearing width of 0.05 eV. The lattice parameters and atomic positions were relaxed for a force convergence tolerance of 0.1 meV Å^{-1}, while for total energies the tolerance was 1 μeV. For each dopant, the kinetic energy cutoff was chosen as 1.3 times the highest default cutoff energy among individual constituent elements. Initial magnetic moments, default cutoff energies and valence electrons for all individual elements used in the calculations can be found in appendix B.

The undoped unit cell of Fe_2P consists of three formula units with lattice parameters $a = 5.811$ Å and $c = 3.419$ Å, as obtained after optimization (in agreement with the experimental values $a = 5.867$ Å and $c = 3.458$ Å, as reported in Ref. [24]). For $MnFeP_{0.66}Si_{0.33}$ the starting unit cell after optimization had $a = 6.115$ Å and $c = 3.264$ Å, which is also sufficiently close to experimental results from [25]($a = 6.166$ Å and $c = 3.290$ Å). Experimental reports generally assume a random distriburion of Si and P over the 1b and 2c positions, but for the sake of simplicity for our supercell all Si atoms were put on 1b site and all P on the 2c site.

In order to study the effect of doping on Fe_2P and $MnFeP_{0.66}Si_{0.33}$, a $2 \times 2 \times 2$ supercell was utilized. One dopant atom was introduced to the supercell on various Wyckoff positions. For $MnFeP_{0.66}Si_{0.33}$, once the site preference was determined, the subsequent doping atoms were distributed semi-randomly on the preferred site for a doping range from 0% to 16% in steps of 2%.

For Li doping this range was extended to 25 %. To investigate the lithiation process, it was modelled in the following way: a set of computations was performed with a single Li atom placed on various possible atomic positions in the supercell, comparing the resulting energies to determine the optimal position at each step of the process.

To obtain T_C it is necessary to model the PM state. For this a smaller $2 \times 2 \times 1$ supercell was doubled along the z direction, again making a $2 \times 2 \times 2$ supercell, but this time an antiparallel magnetic ordering was imposed: the moments inside each $2 \times 2 \times 1$ layer were aligned in the same direction, whereas the moments in adjacent $2 \times 2 \times 1$ layers were opposite (Fig. C.1). Thus one has alternating spin-up and spin-down blocks along the c direction forming an AFM structure with a total magnetic moment of zero. Such an approximation is deemed reasonable for Fe_2P in [12]. This specific AFM supercell was chosen as the one with the lowest energy after a set of energy calculations for various AFM configurations. Experimental data for this system shows that the Fe moment decreases as temperature increases to above T_C [26, 27]. Therefore, we consider AFM structures with low magnetic moments as most reasonable approximation of the PM state. Tested structures include a $2 \times 2 \times 2$ supercell with an antiparallel alignment between unit cells in the a-direction, in checkerboard pattern (both within the ab-plane and across the c-direction) and possible periodicities of the antiparallel alignment along c-direction in a $1 \times 2 \times 4$ supercell.

The size of supercell determines the number of Fe atoms available for substitutions and consequently the precision of the doping steps. The choice of a $2 \times 2 \times 2$ supercell with antiparallel layers (c-direction) therefore leads to a bigger step in Li doping (4 %), as spin-up and spin-down layers must have the same atomic composition, only with an opposite direction for the magnetic moments.

For the experimental samples lithiation was performed by combining Fe_2P compound with lithium in a ball mill. Samples then underwent heat treatment at 1100 °C for 2 hours and at 850 °C for another 20 hours, followed by quenching. Structural information was obtained from room temperature neutron diffraction. The incoherent scattering of Li and also the magnetic contribution of the sample are neglected from the neutron refinement. Curie temperatures were estimated with a differential scanning calorimeter (DSC, TAInstrument Q2000).

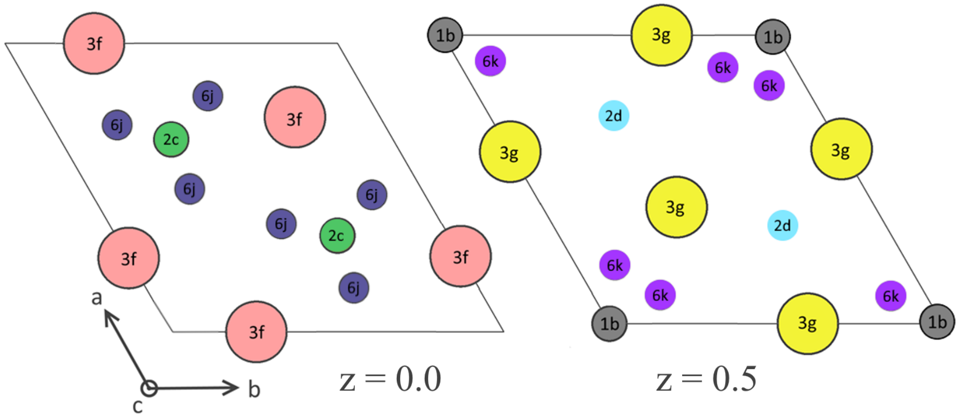

Figure 4.1: Schematic representation of Wyckoff positions in Fe_2P unit cell at two different vertical positions ($z = 0$ and $z = 1/2$).

4.3 RESULTS AND DISCUSSION

4.3.1 EFFECT OF DOPING ON (FE,MN)(P,SI) COMPOUNDS

WHile quite a number of elements were already considered as doping candidates for Fe_2P material family, currently available information is inconsistent due to a variety of starting materials and techniques employed. In this section, we utilize DFT calculations to provide a guide to dopants and an overview of trends they share once introduced to the base compound. To investigate doping possibilities and site preferences the formation energies were calculated. For this, one dopant atom was placed on either of the four possible crystallographic sites of the Fe_2P unit cell or on interstitial positions. The interstitial positions were included to account for the scenario reported for boron atoms in the case of MnFe(P,As,B) [14, 28]. Three such interstitial positions were considered ($6k$, $6j$ and $2d$). The energy cost E_f of forming the doped compound is calculated as the difference between the energies of the doped (E_{doped}) and pure (E_{pure}) compounds minus the chemical potential of the dopant atom (μ_{dopant}) plus the chemical potential of the atom s that dopant substitutes for (μ_s), if applicable. So it is

$$E_f = E_{\text{doped}} + \mu_s - \left(E_{\text{pure}} + \mu_{\text{dopant}}\right) \tag{4.1}$$

in case of a substitution and

$$E_f = E_{\mathrm{doped}} - E_{\mathrm{pure}} - \mu_{\mathrm{dopant}} \tag{4.2}$$

for interstitial additions. The lowest formation energy corresponds to the preferred doping site. All calculated values are presented in appendix C and the results are graphically illustrated in Fig. 4.2

For $\mathrm{MnFeP_{0.66}Si_{0.33}}$ there is an unsurprising tendency for $3d$ metals to replace manganese and for some (Co, Ni, Cr, V) replacing iron has an equal chance. Non-magnetic elements generally prefer to either replace P/Si or occupy interstitial positions. The exact choice seems to correspond to the atomic size of the dopant. Larger elements (Ga, Ge, S, As) tend to be placed at the $2c$ site as it allows for smaller deformation of the crystal cell. On the other hand, atoms with smaller sizes (B, F) prefer the $1b$ site over the $2c$ and even smaller ones (C, N) are incorporated interstitially. An interesting case is the alkali metals: Li (and K for $\mathrm{Fe_2P}$) tend to substitute on the $3g$ position, despite the fact that it does not carry a magnetic moment.

Most of these considerations also apply when pure $\mathrm{Fe_2P}$ is used as a starting material. However, without Mn occupying the $3g$ site, vanadium and chromium show a stronger preference for the $3g$ position. Some elements (K, Al) can now enter the structure, while C, F can no longer do so. This implies that choice of dopant may also be affected by the Fe/Mn and P/Si ratios.

Predictably, the introduction of dopants on the Fe/Mn sites strongly influences the magnetic properties (Fig. 4.3(a)). None of the dopants in the current selection of elements can compare to manganese in terms of the magnetization as the total moment linearly decreases with increasing doping content. For all of the elements that prefer the $3g$ position, the doped compound remains stable over the whole investigated range with the sole exception of Li for which only up to 12% Mn can be substituted. Small amounts of these dopants can be used to control lattice parameters(Fig. 4.3(b)), however, in most cases, similar results can be achieved through variations in Fe/Mn and P/Si ratios without significant loss of magnetization [29]. Lithium shows an opposite trend compared to other $3g$ substitutes – a significant volume expansion and a decrease in c/a ratio is found.

Non-metal substitution have a less pronounced effect on the total magnetic moment (Fig. 4.3(c)). B, F and S have a much stricter doping limit compared to other elements. A possible explanation for the unique moment enhancement observed for F doping lies with the shortening of the intralayer Fe($3f$)-Fe($3f$) distance, which contributes towards a stronger exchange interaction. Fluorine is also the only element that increases the c/a ratio, albeit only slightly. Unfortunately, just a meagre amount of about 4% can be added to the system. Galium has the largest effect on the structural parameters and almost no influence on the magnetization. It greatly decreases c/a, which in $\mathrm{Fe_2P}$-based materials often translates into an increase in T_C. A recent report [19] also indicates that Ga, similarly to B, can improve the mechanical stability of the material.

Interstitial additions are represented by C and N. The lowest formation energy corresponds to the occupation of the $6j$ site for both elements. Yet $6k$ and $2d$ (as well as an option of substitution on $1b$ site for N) are also an option, as their formation energies are only marginally higher. In practice, the final choice depends on the preparation method and the exact stoichiometry [16, 17]. A case when both interstitial and substitutional routes are

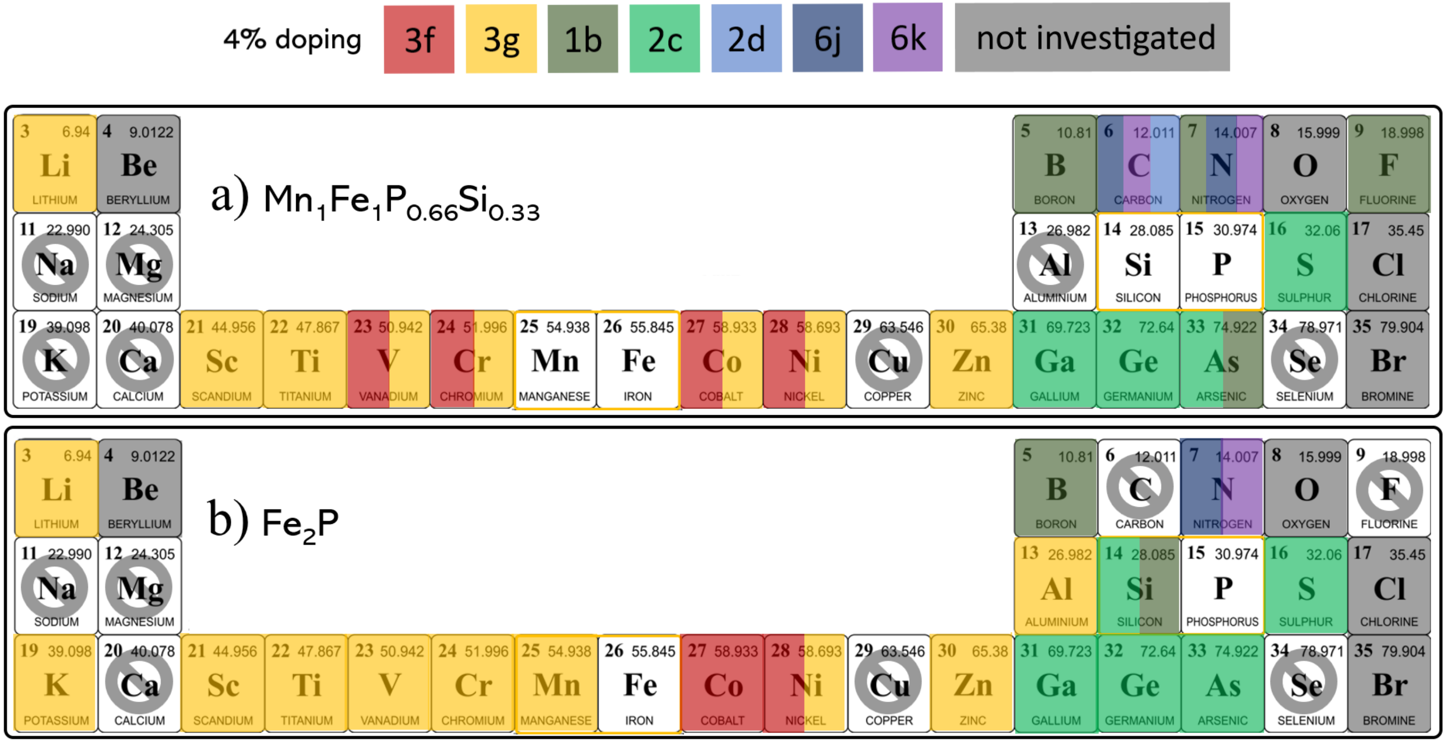

Figure 4.2: Table of doping preferences for $Mn_1Fe_1P_{0.66}Si_{0.33}$ (a) and Fe_2P (b). Colour indicates the most probable Wyckoff position in the crystal structure for each element. Multiple colours are assigned whenever the formation energies are close in values. Elements for which the doped compound is unstable are marked with stop sign.

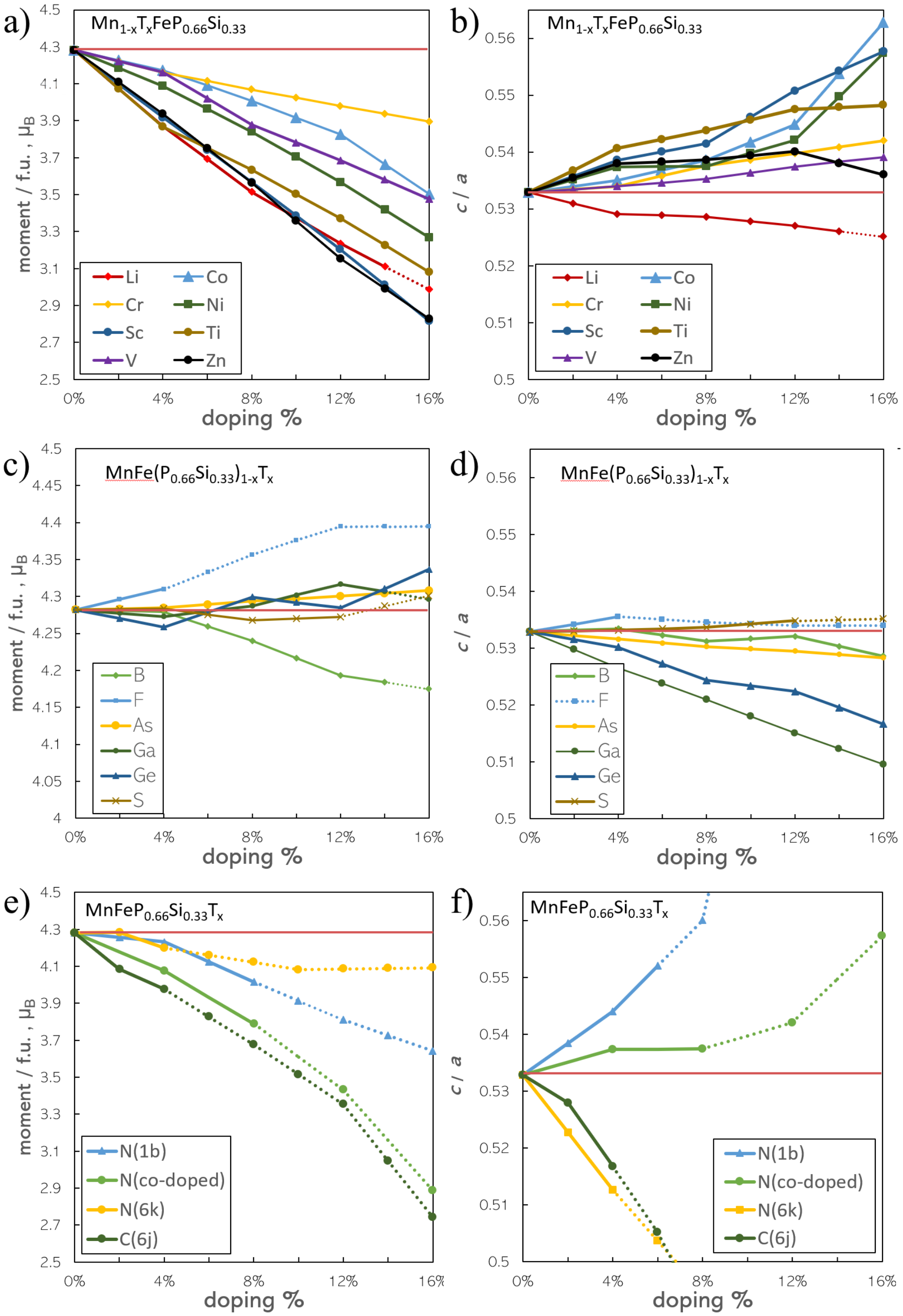

Figure 4.3: Dependence of the magnetic moment per formula unit (a, c, e) and *c*/*a* ratio (b, d, f) on the doping content for various doping elements. Lines are a guide to the eye. Dotted segments of the lines signify ranges with unstable compositions. Red horizontal lines mark the properties of the pure compound.

realized simultaneously is also possible. From the results of our calculations (Fig. 4.3(f)) it is found that the type of doping process will greatly influence the impact on the structural and magnetic parameters. For N substituting P/Si on the 1*b* site will increase the *c*/*a* ratio, whereas occupying an interstitial position will decrease *c*/*a*. The structure is least deformed when both doping routes occur simultaneously. This also allows for the largest amount of N to be incorporated in the material.

4.3.2 Lithiation of the Fe2P-based magnetocaloric materials

Li belongs to a yet unexplored group of possible dopant elements - alkali metals and exhibits an unusual behaviour upon introduction to Fe_2P. In this section, Li doping is investigated in more detail. According to the results obtained after full structural relaxation (Table C.1) lithium prefers to occupy the 3*g* positions replacing iron. A preference for the 3*g* positions is maintained for the whole range of Li doping. This is likely due to the large size of the Li atom, as the 3*g* site has the biggest distances to neighbouring atoms, allowing for the inclusion of lithium with the smallest deformation of the unit cell. As can be seen from Fig. 4.4, during lithiation subsequent replacements occur for atoms that already have Li as their neighbour in the same plane.

The evident non-random nature of the substitutions has several consequences: firstly, the tendency to prefer positions on the same 3*g* plane affects the magnetic interactions of the compound during lithiation, as will be described in detail in the following. Secondly, the formation of Li clusters leads to destabilization of the Fe_2P structure, thereby limiting the maximum amount of lithium that could be introduced in the system. According to the calculations, it is favourable for Li to enter Fe_2P, replacing up to 25 % of the iron atoms (for higher concentrations E_f becomes positive). This, however, is only valid if no secondary phases are taken into account. $Fe_{2-x}Li_xP$ is likely to decompose into tetragonal Fe_3P and LiP at even lower Li content with some other possibilities as described in Ref. [30].

The process of lithiation is accompanied by an overall decrease in the magnetization as the iron atoms on the 3*g* positions, which carry the biggest moment of about $2.23\mu_B$, are replaced by non-magnetic Li atoms. The remaining Fe atoms on the 3*g* positions have their average moment progressively lowered to 1.99 μ_B. The average moment on the 3*f* position is gradually decreasing from 0.83 μ_B to 0.66 μ_B, as the 3*g* sublattice is disrupted. This can be explained by the fact that lithiation creates a non-magnetic buffer between the magnetic sublattices and effectively weakens the corresponding exchange interactions responsible for the mixed magnetism.

Preliminary experimental results indicate that small amounts of Li cause a sharp increase in the Curie temperature both for Fe_2P and for $(Fe, Mn)_2(P, Si)$ (Tab. 4.2). In order to verify this observation and estimate the transition temperature at different stages of lithiation the approach described in [31, 32] was used. The mean-field approximation allows evaluation of the critical temperature by the (positive) total energy difference ΔE between the disordered state and the ordered ferromagnetic state. This energy difference is obtained by calculating total energies for the system in the AFM (E_{AFM}) and the FM (E_{FM}) state. Thus we calculate T_C as

$$T_C = \frac{2}{3(1-n)}\frac{\Delta E}{k_B} = \frac{2}{3(1-n)}\frac{(-E_{FM}+E_{AFM})}{k_B} \tag{4.3}$$

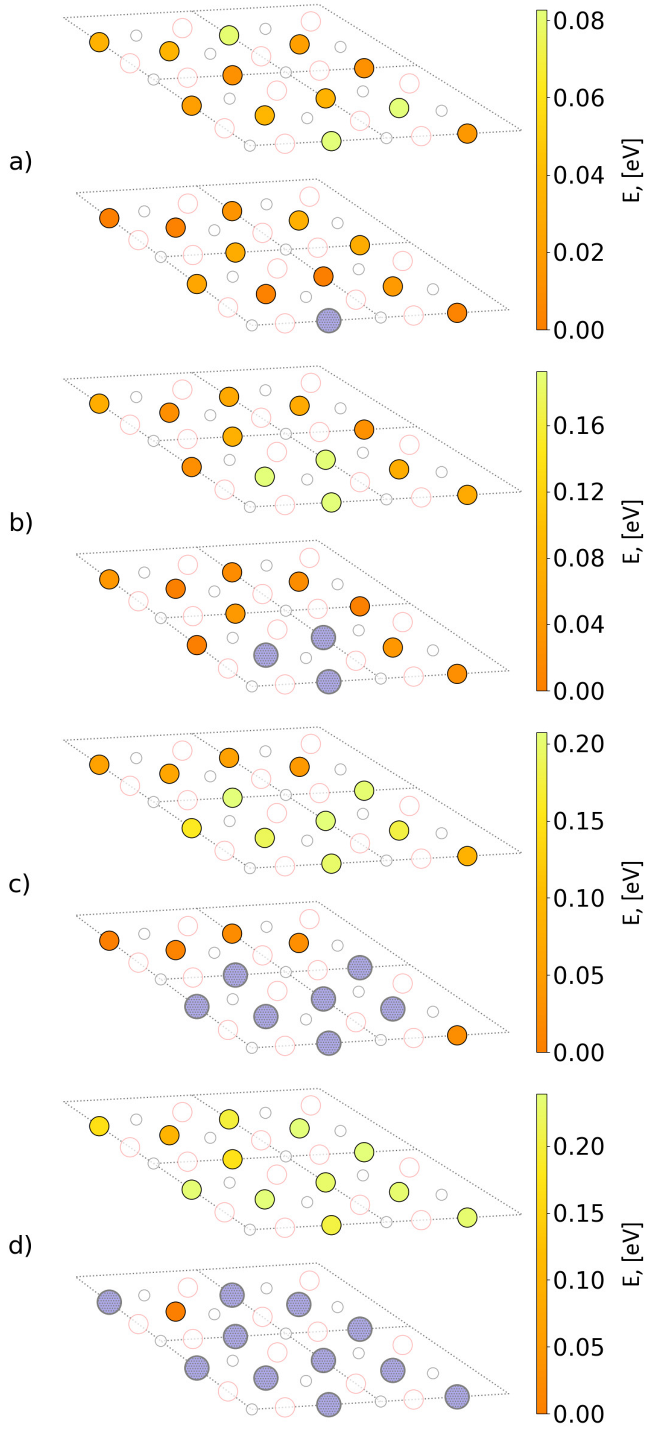

Figure 4.4: Progress of lithiation for the 3g position in $Fe_{2-x}Li_xP$ shown for substitutions of 2(a), 4(b), 8(c) and 12(d) Fe atoms by Li. The colourmap indicates the energy of the substitution for this doping step. Energies are relative to the energy of the most preferred position (dark orange) at each step. Li atoms are marked with lilac circles. The structural deformation is not depicted for simplicity.

Table 4.2: Structural parameters and transition temperatures of experimental samples. Composition denotes element ratio as loaded into the ball mill.

Composition	Li_1Fe_2P			Fe_2P	
T_C (K)	473			216	
Phase	$Fe_{2-x}Li_xP$	Fe	Li	Fe_2P	Fe_3P
Fraction (%)	46(1)	17(1)	36(2)	94(1)	5.5(2)
Lattice parameters					
a (Å)	5.863(1)	2.847(1)	2.869(7)	5.8614(1)	8.958(3)
c (Å)	3.452(1)	–	–	3.4522(1)	4.754(2)
c/a	0.588(1)	–	–	0.589(1)	–
Li site occupation					
$3f$	0.000(0)	–	–	–	–
$3g$	0.059(3)	–	–	–	–
Li content x (%)	2.97	–	–	–	–
Fitting parameters					
Rp (%)	8.93			7.19	
wRp (%)	11.6			9.98	
χ^2 (%)	27.3			9.97	

where n is the concentration of the non-magnetic elements. This simplified approach was used as a fast method to qualitatively estimate the effect of lithiation on T_C. Furthermore, due to the presence of two magnetic sites and the gradual introduction of Li, which disrupts crystal and magnetic symmetry of the system, the commonly used method to calculate T_C by mapping energies onto an effective Hamiltonian becomes rather cumbersome to utilize. Even with this approximation, the resulting Curie temperature for Fe_2P of 236 K lies quite close to the experimental value of 217 K [22]. This indicates a reasonably good balance between computational effort and the obtained result for this method. While this mean field formulation shows reasonable agreement for certain systems [32, 33], it is known to lead to significant errors in the calculated T_C for systems with short-range exchange interactions strongly diluted with non-magnetic elements [34]. In the case of $Fe_{2-x}Li_xP$, technically 25 % (half of the $3g$ positions occupied in $2 \times 2 \times 1$ supercell) substitution is still above the percolation threshold, but the preference of Li for clustering discussed above, together with the fact that the $3g$ sublattice plays a major role in forming magnetic ordering in this system makes the T_C obtained for high percentages of Li less reliable and likely to be overestimated. The calculated values of T_C for different amounts of Li are presented in Fig. 4.5. The introduction of Li causes a sharp linear increase in T_C, which continues until a maximum T_C of about 900 K is reached when 16.7 % of the iron atoms are replaced by Li. For higher Li substitutions T_C slowly decreases. Thus, Li substitutions show the largest increase in T_C among all substitutions reported for this compound [11] with a rate of approximately 45 K/at.%

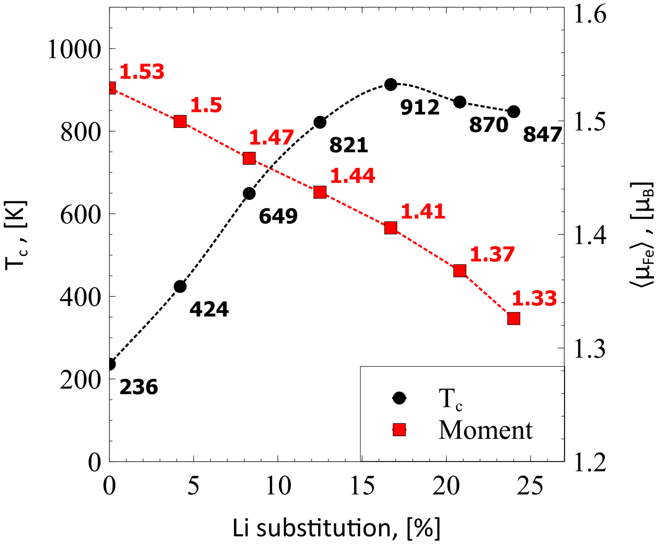

Figure 4.5: Dependence of the critical temperature T_C and average magnetic moment of Fe on both sites as a function of the lithium content. Lines are a guide to the eye.

The change in lattice parameters as a result of the lithiation is presented in Table 4.3. An increase in lattice parameter *a* and a decrease in *c* leads to a decrease in the c/a ratio, while the volume of the unit cell exhibits a slight increase (Fig. 4.6). The changes in the unit cell volume are rather small since the deformations in the *ab* plane and along the *c* axis partially compensate for each other. As presented earlier, in the later stages of the lithiation the Li atoms occupy most of the positions in one of the 3*g* sublayers in the supercell, and therefore the last few substitutions no longer cause further deformations. As a result, the calculated values for the *a* parameter remain practically constant in these later stages.

Table 4.3: Structural parameters and average magnetic moments of Fe on the 3*g* and 3*f* sites during the lithiation of Fe_2P.

Li (at.%)	a (Å)	c (Å)	V (Å^3)	c/a	$\langle\mu_{3g}\rangle$ (μ_B)	$\langle\mu_{3f}\rangle$ (μ_B)
0	5.81	3.42	99.98	0.588	2.23	0.83
4.2	5.83	3.42	100.23	0.586	2.17	0.83
8.3	5.85	3.41	100.46	0.583	2.13	0.81
12.5	5.85	3.40	100.71	0.580	2.10	0.78
16.7	5.88	3.39	100.99	0.577	2.06	0.75
20.8	5.88	3.38	101.35	0.575	2.02	0.71
24	5.88	3.36	101.53	0.571	1.99	0.66

Both an increase in volume and a reduction in the c/a ratio were previously reported as factors that lead to a higher critical temperature in Fe_2P-based materials [11], and $Fe_{2-x}Li_xP$ appears to follow this trend. This effect is further studied in [35], where a heavy dependence

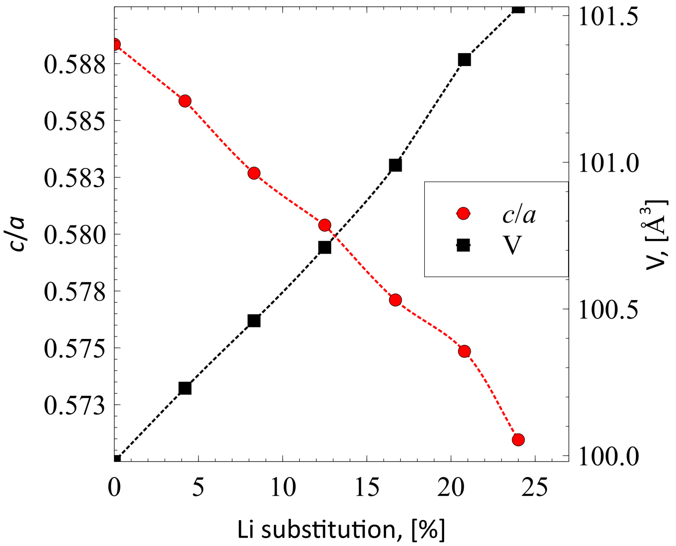

Figure 4.6: Dependence of the c/a ratio and the unit cell volume V on the lithium content. Lines are a guide to the eye.

of the metamagnetic transition of $3f$ species on the local environment is demonstrated. The variation in the Curie temperature is primarily controlled by the change in c/a ratio and the main source of this variation in the case of $Fe_{2-x}Li_xP$ can be linked to the distance between magnetic sublattices. The exchange parameters in this system greatly decrease with the distance as shown in [36]. Among them, the parameters for interlayer $3g$-$3f$ and $3g$-$3g$ interactions are most affected by structural changes. As Li replaces Fe on the $3g$ position, the decrease in c parameter leads to the enhancement of the interlayer interactions which, in turn, causes an increase in T_C. As seen from Figs. 4.5 and 4.7 for a moderate lithiation, the changes in critical temperature can be correlated directly to the variation in the c/a ratio.

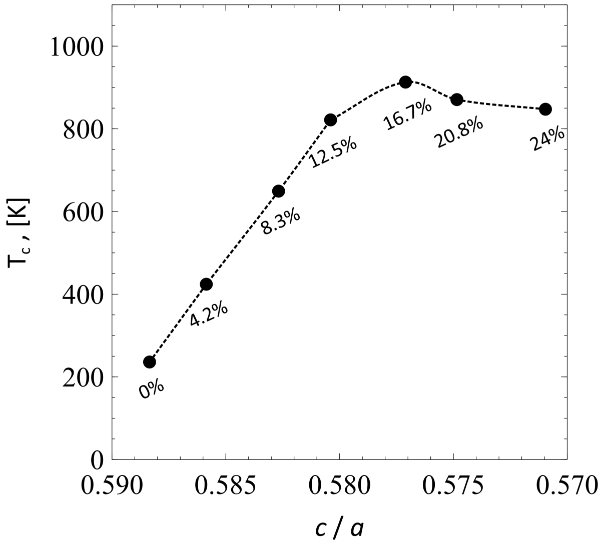

Figure 4.7: Dependence of the critical temperature on the c/a ratio. The lithium content is labelled for each point. Lines are a guide to the eye.

4.4 CONCLUSIONS

In this chapter, first-principles calculations were utilized to investigate the dopants in Fe_2P-based materials. We determine the site preferences for the substitutions with elements from 2nd, 3rd and 4th periods and study the effect of these substitutions on the structural and magnetic properties for different amounts of each dopant element.

The effect of lithium doping on the magnetic and structural properties of Fe_2P is studied in further detail. It is found that Li partially substitutes Fe on the $3g$ site. For $Fe_{2-x}Li_xP$ we present the development of the Curie temperature and the magnetic moments on the Fe sites as a function of the Li content. Since Li prefers the $3g$ positions a relatively large magnetic moment is lost on each substitution, causing an overall reduction in the magnetization. The formation of Li clusters at higher doping contents further disrupts the magnetic structure. At the same time even a small amount of lithium doping leads to a drastic increase in T_C. This is primarily the result of structural changes, in the c/a ratio in particular, as the c parameter decreases with increasing Li content, whereas the a parameter increases.

REFERENCES

[1] D. T. Cam Thanh, E. Brück, N. T. Trung, J. C. P. Klaasse, K. H. J. Buschow, Z. Q. Ou, O. Tegus, and L. Caron. "Structure, magnetism, and magnetocaloric properties of $MnFeP_{1-x}Si_x$ compounds". In: *J. Appl. Phys.* 103.7 (Apr. 2008), 07B318. DOI: `10.1063/1.2836958`.

[2] E. Brück, M. Ilyn, A. Tishin, and O. Tegus. "Magnetocaloric effects in $MnFeP_{1-x}As_x$-based compounds". In: *J. Magn. Magn. Mater.* 290-291 (Apr. 2005), pp. 8–13. DOI: `10.1016/j.jmmm.2004.11.152`.

[3] H. Yamada and K. Terao. "First-Order Transition of Fe_2P and Anti-Metamagnetic Transition". In: *Phase Transitions* 75.1-2 (Jan. 2002), pp. 231–242. DOI: `10.1080/01411590290023120`.

[4] N. H. Dung, L. Zhang, Z. Q. Ou, and E. Brück. "Magnetoelastic coupling and magnetocaloric effect in hexagonal Mn-Fe-P-Si compounds". In: *Scr. Mater.* 67.12 (Dec. 2012), pp. 975–978. DOI: `10.1016/j.scriptamat.2012.08.036`.

[5] X. F. Miao, L. Caron, P. Roy, N. H. Dung, L. Zhang, W. A. Kockelmann, R. A. de Groot, N. H. van Dijk, and E. Brück. "Tuning the phase transition in transition-metal-based magnetocaloric compounds". In: *Phys. Rev. B* 89.17 (May 2014), p. 174429. DOI: `10.1103/PhysRevB.89.174429`.

[6] Z. Ou, L. Caron, N. Dung, L. Zhang, and E. Brück. "Interstitial boron in MnFe(P,As) giant-magnetocaloric alloy". In: *Results Phys.* 2 (2012), pp. 110–113. DOI: `10.1016/j.rinp.2012.09.005`.

[7] N. H. Dung, Z. Q. Ou, L. Caron, L. Zhang, D. T. C. Thanh, G. A. de Wijs, R. A. de Groot, K. H. J. Buschow, and E. Brück. "Mixed Magnetism for Refrigeration and Energy Conversion". In: *Adv. Energy Mater.* 1.6 (Nov. 2011), pp. 1215–1219. DOI: `10.1002/aenm.201100252`.

[8] J. Cedervall, M. S. Andersson, E. K. Delczeg-Czirjak, D. Iu şan, M. Pereiro, P. Roy, T. Ericsson, L. Häggström, W. Lohstroh, H. Mutka, M. Sahlberg, P. Nordblad, and P. P. Deen. "Magnetocaloric effect in Fe_2P: Magnetic and phonon degrees of freedom". In: *Phys. Rev. B* 99 (17 May 2019), p. 174437. DOI: `10.1103/PhysRevB.99.174437`.

[9] E. K. Delczeg-Czirjak, L. Delczeg, M. P. J. Punkkinen, B. Johansson, O. Eriksson, and L. Vitos. "Ab initio study of structural and magnetic properties of Si-doped Fe_2P". In: *Phys. Rev. B* 82.8 (Aug. 2010), p. 085103. DOI: `10.1103/PhysRevB.82.085103`.

[10] Z. Dechang, T. Zhucai, Z. Zhigang, Z. Xichun, L. Zhongwu, and Y. Hongya. *Patent CN102881393A*. 2013.

[11] E. K. Delczeg-Czirjak, Z. Gercsi, L. Bergqvist, O. Eriksson, L. Szunyogh, P. Nordblad, B. Johansson, and L. Vitos. “Magnetic exchange interactions in B-, Si-, and As-doped Fe_2P from first-principles theory”. In: *Phys. Rev. B* 85.22 (June 2012), p. 224435. DOI: `10.1103/PhysRevB.85.224435`.

[12] P. Roy, E. Torun, and R. A. de Groot. “Effect of doping and elastic properties in $(Mn,Fe)_2(Si,P)$”. In: *Phys. Rev. B* 93.9 (Mar. 2016), p. 94110. DOI: `10.1103/PhysRevB.93.094110`.

[13] N. Thang, N. Dijk, and E. Brück. “Tuneable Giant Magnetocaloric Effect in $(Mn,Fe)_2(P,Si)$ Materials by Co-B and Ni-B Co-Doping”. In: *Materials (Basel).* 10.1 (Dec. 2016), p. 14. DOI: `10.3390/ma10010014`.

[14] F. Guillou, H. Yibole, G. Porcari, and E. Brück. “Boron addition in MnFe(P,Si) magnetocaloric materials: interstitial vs . substitutional scenarii”. In: *Phys. Status Solidi* 11.5-6 (May 2014), pp. 1007–1010. DOI: `10.1002/pssc.201300569`.

[15] P. Jernberg, A. Yousif, L. Häggström, and Y. Andersson. “A Mössbauer study of $Fe_2P_{1-x}Si_x$ ($x \leq 0.35$)”. In: *J. Solid State Chem.* 53.3 (July 1984), pp. 313–322. DOI: `10.1016/0022-4596(84)90108-7`.

[16] N. Thang, X. Miao, N. van Dijk, and E. Brück. “Structural and magnetocaloric properties of $(Mn,Fe)_2(P,Si)$ materials with added nitrogen”. In: *J. Alloys Compd.* 670 (June 2016), pp. 123–127. DOI: `10.1016/j.jallcom.2016.02.014`.

[17] Q. Zhou, Z. G. Zheng, Z. G. Qiu, Y. Hong, Y. Mozharivskyj, and D. C. Zeng. “Effect of Carbon Doping on the Structure and Magnetocaloric Properties of $Mn_{1.15}Fe_{0.80}P_{0.50}Si_{0.50}$ Compounds”. In: *J. Supercond. Nov. Magn.* 32.12 (Dec. 2019), pp. 3987–3994. DOI: `10.1007/s10948-019-05184-8`.

[18] J. Lai, B. Huang, X. Miao, N. Van Thang, X. You, M. Maschek, L. van Eijck, D. Zeng, N. van Dijk, and E. Brück. “Combined effect of annealing temperature and vanadium substitution for mangetocaloric $Mn_{1.2-x}V_xFe_{0.75}P_{0.5}Si_{0.5}$ alloys”. In: *J. Alloys Compd.* 803 (Sept. 2019), pp. 671–677. DOI: `10.1016/j.jallcom.2019.06.239`.

[19] S. Ma, B. Wurentuya, X. Wu, Y. Jiang, O. Tegus, P. Guan, and B. Narsu. “*Ab-initio* mechanical and thermal properties of $FeMnP_{1-x}Ga_x$ compounds as refrigerant for room-temperature magnetic refrigeration”. In: *RSC Adv.* 7.44 (2017), pp. 27454–27463. DOI: `10.1039/C7RA04274D`.

[20] J. Leitão, M. van der Haar, A. Lefering, and E. Brück. “Magnetic and magnetocaloric exploration of Fe rich $(Mn,Fe)_2(P,Ge)$”. In: *J. Magn. Magn. Mater.* 344 (Oct. 2013), pp. 49–54. DOI: `10.1016/j.jmmm.2013.05.032`.

[21] A. Catalano, R. Arnott, and A. Wold. “Magnetic and crystallographic properties of the system $Fe_2P_{1-x}As_x$”. In: *J. Solid State Chem.* 7.3 (July 1973), pp. 262–268. DOI: `10.1016/0022-4596(73)90132-1`.

[22] L. Lundgren, G. Tarmohamed, O. Beckman, B. Carlsson, and S. Rundqvist. “First Order Magnetic Phase Transition in Fe_2P”. In: *Phys. Scr.* 17.1 (Jan. 1978), pp. 39–48. DOI: `10.1088/0031-8949/17/1/008`.

[23] M. Methfessel and A. T. Paxton. "High-precision sampling for Brillouin-zone integration in metals". In: *Phys. Rev. B* 40.6 (Aug. 1989), pp. 3616–3621. DOI: `10.1103/PhysRevB.40.3616`.

[24] B. Carlsson, M. Gölin, and S. Rundqvist. "Determination of the homogeneity range and refinement of the crystal structure of Fe_2P". In: *J. Solid State Chem.* 8.1 (Sept. 1973), pp. 57–67. DOI: `10.1016/0022-4596(73)90021-2`.

[25] Z. Ou. "Magnetic structure and phase formation of magnetocaloric Mn-Fe-P-X compounds". PhD thesis. TU Delft, 2013.

[26] N. H. Dung, L. Zhang, Z. Q. Ou, L. Zhao, L. van Eijck, A. M. Mulders, M. Avdeev, E. Suard, N. H. van Dijk, and E. Brück. "High/low-moment phase transition in hexagonal Mn-Fe-P-Si compounds". In: *Phys. Rev. B* 86.4 (July 2012), p. 045134. DOI: `10.1103/PhysRevB.86.045134`.

[27] H. Yibole, F. Guillou, L. Caron, E. Jiménez, F. M. F. de Groot, P. Roy, R. de Groot, N. H. van Dijk, and E. Brück. "Moment evolution across the ferromagnetic phase transition of giant magnetocaloric $(Mn,Fe)_2(P,Si,B)$". In: *Phys. Rev. B* 91.1 (Jan. 2015), p. 014429. DOI: `10.1103/PhysRevB.91.014429`.

[28] F. Guillou, G. Porcari, H. Yibole, N. van Dijk, and E. Brück. "Taming the First-Order Transition in Giant Magnetocaloric Materials". In: *Adv. Mater.* 26.17 (May 2014), pp. 2671–2675. DOI: `10.1002/adma.201304788`.

[29] X. You. "Design of efficient magnetocaloric materials for energy conversion." PhD thesis. TU Delft, 2020.

[30] S. P. Ong, L. Wang, B. Kang, and G. Ceder. "Li-Fe-P-O 2 Phase Diagram from First Principles Calculations". In: *Chem. Mater.* 20.5 (Mar. 2008), pp. 1798–1807. DOI: `10.1021/cm702327g`.

[31] F. Körmann, D. Ma, D. D. Belyea, M. S. Lucas, C. W. Miller, B. Grabowski, and M. H. F. Sluiter. ""Treasure maps" for magnetic high-entropy-alloys from theory and experiment". In: *Appl. Phys. Lett.* 107.14 (Oct. 2015), p. 142404. DOI: `10.1063/1.4932571`.

[32] K. Sato, L. Bergqvist, J. Kudrnovský, P. H. Dederichs, O. Eriksson, I. Turek, B. Sanyal, G. Bouzerar, H. Katayama-Yoshida, V. A. Dinh, T. Fukushima, H. Kizaki, and R. Zeller. "First-principles theory of dilute magnetic semiconductors". In: *Rev. Mod. Phys.* 82.2 (May 2010), pp. 1633–1690. DOI: `10.1103/RevModPhys.82.1633`.

[33] M. Ležaić, P. Mavropoulos, and S. Blügel. "First-principles prediction of high Curie temperature for ferromagnetic bcc-Co and bcc-FeCo alloys and its relevance to tunneling magnetoresistance". In: *Appl. Phys. Lett.* 90.8 (Feb. 2007), p. 082504. DOI: `10.1063/1.2710181`.

[34] K. Sato, W. Schweika, P. H. Dederichs, and H. Katayama-Yoshida. "Low-temperature ferromagnetism in (Ga, Mn)N: Ab initio calculations". In: *Phys. Rev. B* 70.20 (Nov. 2004), p. 201202. DOI: `10.1103/PhysRevB.70.201202`.

[35] Z. Gercsi, E. K. Delczeg-Czirjak, L. Vitos, A. S. Wills, A. Daoud-Aladine, and K. G. Sandeman. "Magnetoelastic effects in doped Fe_2P". In: *Phys. Rev. B* 88.2 (July 2013), p. 024417. DOI: `10.1103/PhysRevB.88.024417`.

[36] X. Liu, J. Ping Liu, Q. Zhang, and Z. Altounian. “Fe magnetic moment formation and exchange interaction in Fe_2P: A first-principles study”. In: *Phys. Lett. A* 377.9 (Mar. 2013), pp. 731–735. DOI: `10.1016/j.physleta.2013.01.019`.

5

Y-FE BASED MAGNETOCALORIC MATERIALS

"And now for something completely different."

— Christopher Trace

In this chapter, the Fe-Y material family is studied with the focus on two different Fe-Mn-Y systems: Y(Fe,Mn)$_3$ and Y$_6$(Fe,Mn,Co)$_{23}$. The influence of manganese and cobalt on both the structural and magnetic properties of Y$_6$(Fe,Mn,Co)$_{23}$ is demonstrated by the preparation and characterization of compounds with varying dopant contents. The possibility to control and shift the Curie temperature towards the room-temperature range by Mn and Co doping is demonstrated. The magnetocaloric performance is estimated through magnetic entropy change (ΔS_m) measurements. The Y(Fe,Mn)$_3$ system is synthesized for the first time and the viability of Mn doping is assessed.

5.1 Introduction

Intermetallic compounds with rare earth elements and transition metals are best known for their potential as functional materials, such as permanent magnets or hydrogen storage materials[1]. Since these compounds often demonstrate promising magnetic properties, they are also of interest for magnetocaloric applications. The main drawback of these rare-earth-based compounds is the price and availability. Still, among the RE elements, Y remains a suitable choice with somewhat lower cost, while Y-based compounds typically maintain a large magnetization. For this reason, the RE intermetallics consisting of Y and Fe as the transition metal are among the most intensively studied ones. The Y-Fe binary phase diagram [2, 3] offers a number of stable phases: Y_2Fe_{17}, Y_6Fe_{23}, YFe_3 and YFe_2. Some properties of these phases are presented in table 5.1.

Table 5.1: Structure and magnetic properties of Y-Fe binary compounds.

Compound	Structure	T_C, K	M_s, $\mathrm{A\,m^2\,kg^{-1}}$
Y_2Fe_{17}	$P63/mmc$	303 [4]	160 [5]
Y_6Fe_{23}	$Fm\bar{3}m$	485 [4]	125 [6]
YFe_3	$R\bar{3}m$	545 [4]	90 [7]
YFe_2	$Fd\bar{3}m$	519 [8]	77 [8]

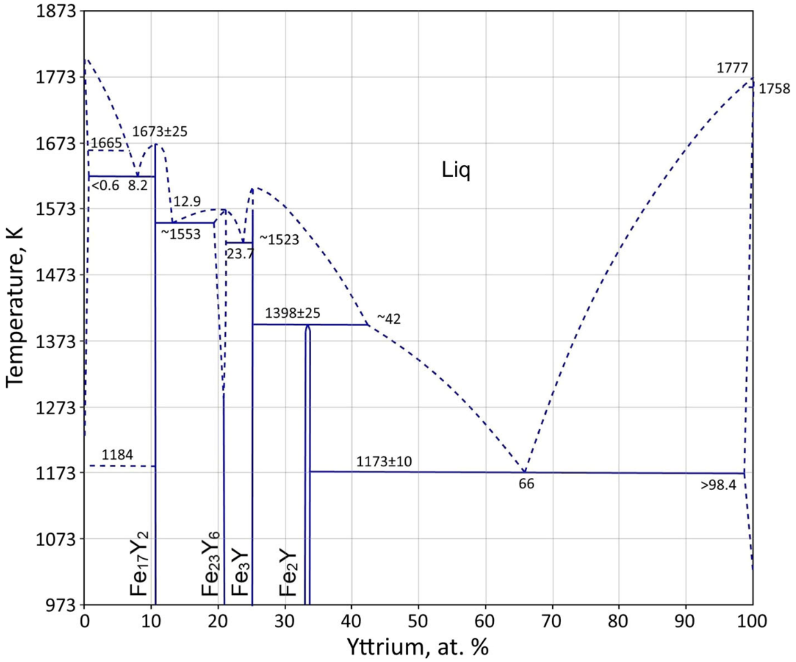

Figure 5.1: Fe-Y phase diagram [2].

Among them the most well studied is Y_2Fe_{17} with multiple reports describing its magnetocaloric properties [9–11]. The main advantage of this compound is a combination of rather high saturation magnetization and transition temperature of 303 K, suitable for room temperature refrigeration. This material exhibits a second-order transition with reported values of $-\Delta S$ ranging from 1.89 to 2.4 $\mathrm{J\,kg^{-1}\,K^{-1}}$ under an applied magnetic field change of 2 T, depending on the preparation method.

The other phases have not been extensively investigated for their MCE due to the much higher critical temperatures lying between 450 K and 550 K [4]. From the available reports [12, 13], YFe_2 appears to be far less suitable for magnetocaloric applications than other phases. The lower Fe to Y ratio, in this case, leads to an increase in price and a smaller saturation magnetization. An attempt has been made to tune down the transition temperature to RT range *via* Mn doping [8], yet the resulting entropy change of the compound with $T_C = 330\,\mathrm{K}$ is rather low at 0.8 $\mathrm{J\,kg^{-1}\,K^{-1}}$ for a 0–2 T field change.

Investigations into the various properties of Y_6Fe_{23} can be found in the literature, describing successful synthesis routes and magnetic properties [14–16]. Yet, its potential for room-temperature magnetic refrigeration has not been investigated. This compound has a cubic $Fm3m$ structure with lattice parameter $a = 12.084\,\mathrm{Å}$, as described by Kripyakevich *et al.*, [17] and undergoes a FM-PM transition close to 485 K [4]. Similar to the case of YFe_2, a significant decrease in T_C upon Mn doping has been observed in several works [18–21]. $Y_6(Fe_{1-x}Mn_x)_{23}$ has been confirmed to remain stable over the whole x range. The magnetic structure however undergoes a change with an increasing amount of Mn. First, it switches to a magnetic cluster glass and then to ferrimagnetic ordering. In the FM phase an increased Mn content leads to a gradual decrease in both magnetization and T_C [22]. Based on the magnetic phase diagram [19], the FM Fe-rich side, with an iron concentration in the range $0.8 \geq x \geq 0.9$, is of most interest for the MCE. The system can easily reach a Curie temperature around RT within this range, while the FM order is preserved. Therefore, additional research into the magnetization, Curie temperature and magnetocaloric properties of $Y_6(Fe_{1-x}Mn_x)_{23}$ compounds is warranted.

While the other intermediate compounds of the Fe-Y system have been studied frequently, research into YFe_3 is far less common. The studies performed to date do show some potential in terms of magnetic properties [23, 24]. Despite the lower Fe content, the FM YFe_3 phase still shows a saturation magnetization that is high enough to be considered as a potential magnetic refrigerant $M_s = 90\,\mathrm{A\,m^2\,kg^{-1}}$ [7]. YFe_3 has the $PuNi_3$-type structure, which corresponds to the rhombohedral lattice system with space group $R\bar{3}m$ ($a = 5.13\,\mathrm{Å}$, $c = 24.61\,\mathrm{Å}$). Similar to the other phases discussed above, there are indications that the high Curie temperature (545 K) may be lowered with dopants. One example is Ni doping, as investigated by Moskaitis *et al.* [25].

Focusing on the more promising of the previously unexplored phases, YFe_3 and Y_6Fe_{23} were selected for further study. In the following sections, the effects of Mn and Co co-doping on the magnetocaloric properties of $Y_6(Fe_{1-x-y}Mn_xCo_y)_{23}$ are investigated. The $YFe_{3-x}Mn_x$ series is studied for the first time. The main goal for both systems being the room temperature transition with a sufficiently large entropy change.

5.2 EXPERIMENTAL DETAILS

THE samples were prepared from stoichiometric amounts of pure elements. (chunks of 99.7 % Mn, 99.8% Co granules, 99.98% Fe granules and 99.9% Y pieces) All samples were prepared by arc melting. Mn chunks were first melted separately to remove any stress in the Mn pieces and reduce impurities. Pre-melted manganese and iron were then melted together before yttrium was added. Structural properties were obtained with XRD and for magnetization measurements, SQUID and VSM were utilized as described in 2.3. Previous reports [17, 20] suggest 2-10 days of annealing at 900 K followed by quenching. To test the effect of the annealing process, the phase composition of one sample was investigated with XRD and a subsequent Rietveld refinement before and after the suggested heat treatment. The results of this analysis are summarized in table 5.2. The annealing process has a low impact on final sample quality, as in both cases, the impurity is found to be negligible. In fact, the unannealed sample has a slightly higher purity. This indicates that the formation of the Y_6Fe_{23} phase is not affected by heat treatment. Therefore, the annealing process was skipped for all subsequent samples.

Table 5.2: Phase fractions for both the annealed and not annealed $(Fe_{2.9}Mn_{0.1})_{23}Y_6$ compound calculated by a Rietveld refinement along with the χ^2 values.

Compound	Main phase, %	Impurity phase, %	χ^2
annealed	98.04	1.96	2.26
not annealed	99.35	0.65	2.23

5.3 RESULTS AND DISCUSSION

5.3.1 $Y_6(Fe_{1-x}Mn_x)_{23}$

IN order to investigate the Fe-rich side of the $Y_6(Fe_{1-x-}Mn_x)_{23}$ system, samples were prepared in the range $0 \geq x \geq 0.25$ ($x = 0$, 0.10, 0.13, 0.15, 0.17, 0.20, 0.25) For the Mn-free sample, all measured peaks match the calculated fit for the Y_6Fe_{23} phase, and no secondary phases were observed (Fig. 5.2). For the other samples, the amount of secondary phases is also relatively low. The impurity content was identified as the YFe_2 phase. The degree of phase segregation does not correlate with Mn content and is determined by the preparation process. Furthermore, the structural parameters of each compound were also obtained to estimate the influence of manganese on the crystal structure (Fig. 5.3). The addition of Mn leads to a linear increase in the a parameter due to the substitution of Fe by the larger Mn atom. The value for the undoped compound ($x = 0$) is in a good agreement with the previously reported one (a =12.084 Å) [17].

Figure 5.4 shows the temperature dependence of the magnetization for the $Y_6(Fe_{1-x-}Mn_x)_{23}$ series. The saturation magnetization for the undoped Y_6Fe_{23} compound differs somewhat from previous values found in the literature (117 $\mathrm{A\,m^2\,kg^{-1}}$ in [26], 125 $\mathrm{A\,m^2\,kg^{-1}}$ in [6] and 152.8 $\mathrm{A\,m^2\,kg^{-1}}$ in [27]). The current result of 135 $\mathrm{A\,m^2\,kg^{-1}}$ lies close to the average value of these previous studies.

All doped samples, along with the parent compound, exhibit a second-order transition. The Curie temperatures, obtained from the measurements in 0.01 T, demonstrate a signif-

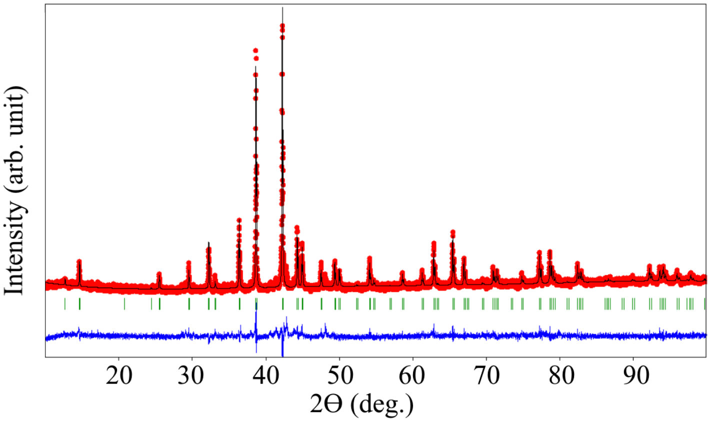

Figure 5.2: Powder XRD patterns of Y_6Fe_{23} (red line) measured at room temperature including a fit (black line). Vertical green lines indicate Bragg peak positions. The blue line represents the difference between data and fit.

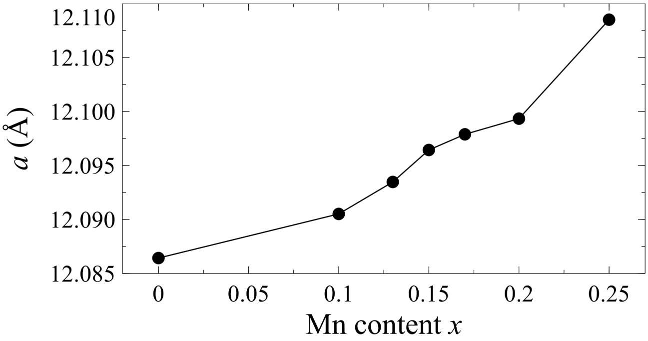

Figure 5.3: Lattice parameter a as a function of the manganese content.

icant decrease, which is accompanied by a decrease in magnetization. These data show that T_C can be easily shifted to the room temperature range by small ($x = 0.15$) amounts of Mn doping. For this sample with a RT transition, the saturation magnetization remains at a reasonably high value of 85 $\mathrm{A\,m^2\,kg^{-1}}$. Both T_C and M_s decrease linearly with Mn content, albeit the T_C shows a more rapid reduction than the magnetization. The main contribution to magnetization in these compounds comes from the magnetic moments of the Fe and Mn atoms. The large decrease in T_C with increasing Mn content can be attributed to the decrease in magnetization of the Fe sublattice and the weakened exchange interaction between the Fe atoms and the Mn substitutes. Additionally, since Y_6Mn_{23} is an antiferromagnet, a higher Mn content introduces a competition between the Mn–Mn AFM coupling and the original Fe–Fe FM coupling, thereby further affecting T_C.

To investigate the magnetocaloric performance the isothermal entropy change was calculated for the $Y_6(Fe_{0.85}Mn_{0.15})_{23}$ compound. For this, isothermal magnetization curves were measured at either side of the Curie temperature of the sample (T_C = 310 K). The Arrot plot produced from measurements in the temperature range from 280 to 360 K in

Table 5.3: Results of the structural refinement and magnetization measurements for the $Y_6(Fe_{1-x}Mn_x)_{23}$ series.

x	a, Å	V, Å^3	Impurity, %	χ^2	M_s, $\mathrm{A\,m^2\,kg^{-1}}$	T_C, K
0.00	12.086	1765.6	0.00	2.48	135	475
0.10	12.091	1767.4	0.65	2.23	98	357
0.13	12.093	1768.7	2.11	2.03	91	327
0.15	12.096	1760.0	1.31	2.51	85	310
0.17	12.098	1770.6	8.68	2.60	74	264
0.20	12.099	1771.3	0.72	2.16	69	249
0.25	12.109	1775.3	5.23	2.14	50	172

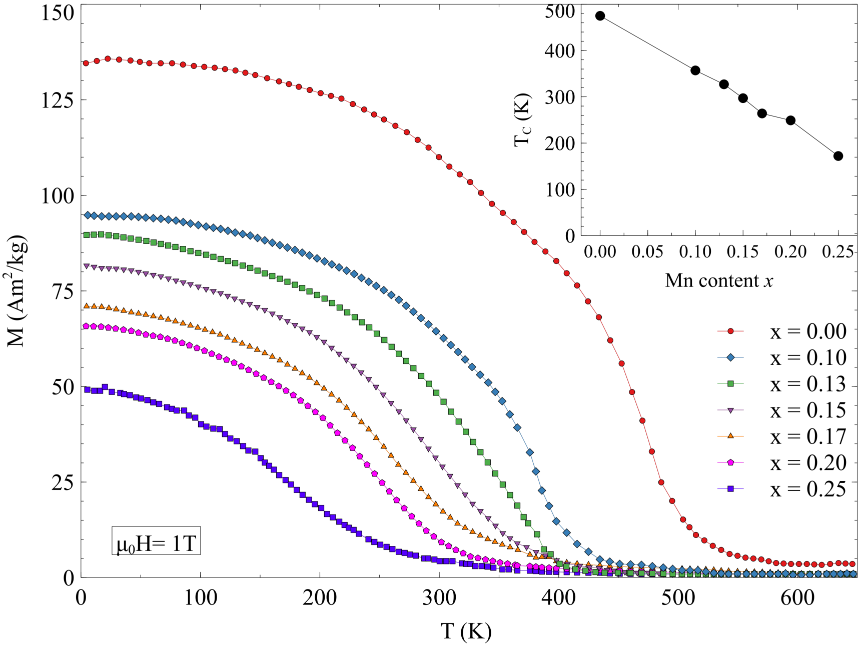

Figure 5.4: Magnetization as a function of temperature for $Y_6(Fe_{1-x}Mn_x)_{23}$ with a range of x values. The inset shows T_C as a function of the Mn content x.

steps of 2 K for a field change of 0–1.5 T is shown in Fig. 5.5(a). The linear relation near the transition temperature is a signature of the second-order transition [28]. No temperature or field hysteresis was observed near T_C. From the isothermal magnetization curves, $\Delta S(T)$ is obtained, as described in section 2.1. Figure 5.5(b) shows the calculated entropy change for a field change of 0–1.5 T. The sample displays a modest magnetocaloric effect, with a maximum value of $-\Delta S_m = 1.1\,\mathrm{J\,kg^{-1}\,K^{-1}}$.

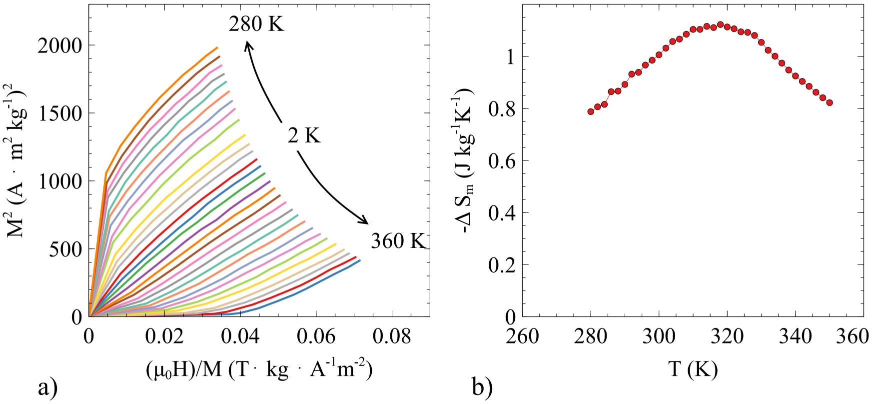

Figure 5.5: Arrott plot (a) and temperature dependence of the magnetic entropy change for the $Y_6(Fe_{0.85}Mn_{0.15})_{23}$ compound around T_C for a 0–1.5 T field change (b).

5.3.2 THE TUNING OF Y_6Fe_{23} COMPOUND BY MN-CO CO-DOPING

From the $Y_6(Fe_{1-x}Mn_x)_{23}$ series, two compounds ($x = 0.20, 0.25$) were selected for cobalt co-doping. Cobalt with its higher moment can potentially boost the magnetization, and by a combination of Co and Mn substitutions, a compound with a RT transition, but with a higher magnetization than in $Y_6(Fe_{1-x}Mn_x)_{23}$ could be found. To check the influence of cobalt on the system a series with varying Co content is studied ($y = 0, 0.03, 0.05, 0.07, 0.09$) for both starting compositions. The magnetization as a function of the temperature and as a function of the applied magnetic field can be seen in Figures 5.6 and 5.7, respectively. The Curie temperatures, along with other relevant properties can be found in table 5.4.

The addition of cobalt leads to an increase in T_C and a relatively large increase in magnetization. This is accompanied by a slow decrease of the unit cell volume. The maximum magnetization of this system at a temperature of 5 kelvin and a magnetic field of 1 T is 80 $A\,m^2\,kg^{-1}$ for $y = 0.09$, compared to 66 $A\,m^2\,kg^{-1}$ for $y = 0$. While a substantial 14% increase in saturation magnetization has been reached as intended, the rate of growth for T_C is higher at 33%. Mn-Co co-doping can nevertheless be used to accurately tune T_C and magnetization. Small amounts of Co doping allow for a finer adjustment of the transition temperature, in contrast to purely Mn doping. Samples with $y = 0.07$ from both series were selected to evaluate the entropy changes due to their transition near RT.

Figure 5.8 shows $\Delta S_m(T)$ curves in a field change of 0–1.5 T for the $Y_6(Fe_{0.93-x}Mn_xCo_0.07)_{23}$ ($x = 0.2, 0.25$) compounds. The maximum ΔS_m observed around the transition temperatures amounts to 0.61 $J\,kg^{-1}\,K^{-1}$ and 0.45 $J\,kg^{-1}\,K^{-1}$ for $x = 0.2$ and $x = 0.25$, respectively.

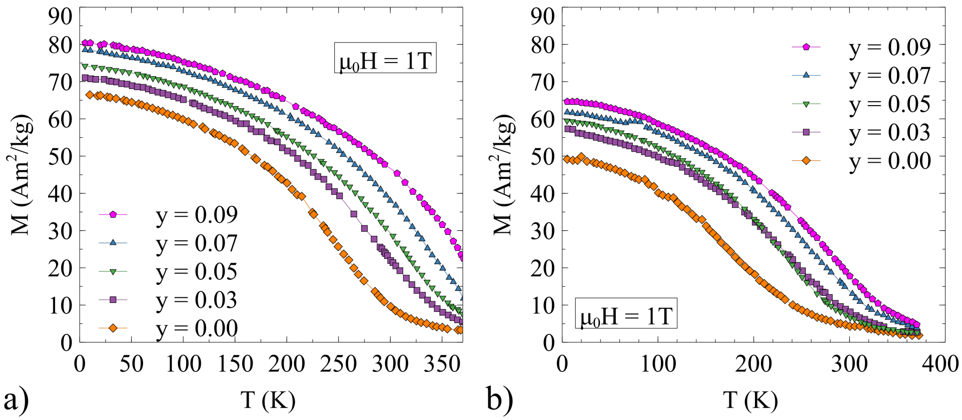

Figure 5.6: Magnetization as a function of temperature for the $Y_6(Fe_{1-x-y}Mn_xCo_y)_{23}$ system with $x = 0.25$(a) and $x = 0.20$(b) for a range of y values. The measurements were performed at a constant field of 1 T.

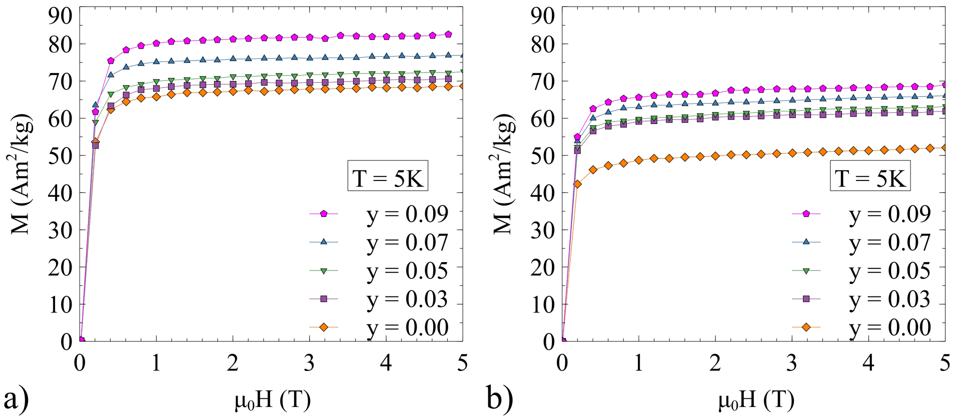

Figure 5.7: Magnetization as a function of applied magnetic field for the $Y_6(Fe_{1-x-y}Mn_xCo_y)_{23}$ system with $x = 0.25$(a) and $x = 0.20$(b) for a range of y values. The measurements were performed at a constant temperature of 5 K.

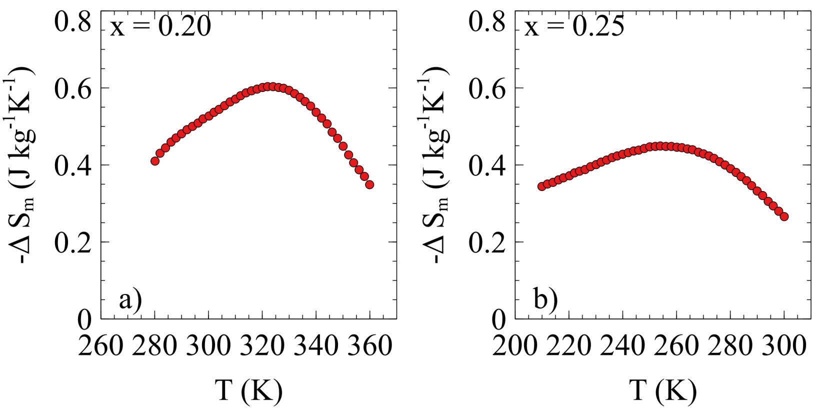

Figure 5.8: Magnetic entropy change as a function of temperature for $Y_6(Fe_{0.93-x}Mn_xCo_{0.07})_{23}$ with $x = 0.20$ (a) and $x = 0.25$ (b).

Table 5.4: Results of the structural refinement and magnetization measurements for $Y_6(Fe_{1-x-y}Mn_xCo_y)_{23}$ series.

	y	a, Å	V, Å^3	Impurity, %	χ^2	M_s, A m^2 kg^{-1}	T_C, K
$x = 0.20$	0.00	12.098	1770.6	7.94	2.25	66	249
	0.03	12.092	1768.1	5.99	1.46	66	289
	0.05	12.088	1766.4	4.76	2.96	71	313
	0.07	12.089	1766.6	7.32	1.70	79	340
	0.09	12.086	1765.3	2.40	1.70	80	370
$x = 0.25$	0.00	12.109	1775.3	5.23	2.14	50	172
	0.03	12.100	1771.5	2.42	1.60	59	232
	0.05	12.100	1771.5	2.47	1.60	60	240
	0.07	12.097	1770.1	2.59	3.30	63	259
	0.09	12.093	1768.7	2.77	2.83	66	280

5.3.3 $Y(Fe_{1-x}Mn_x)_3$

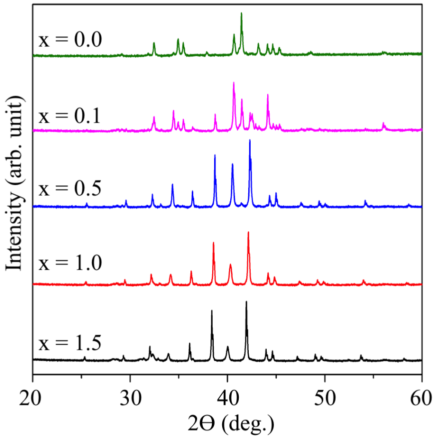

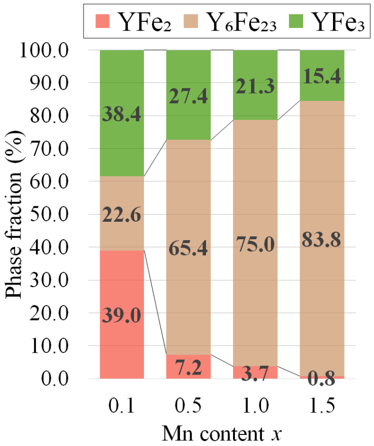

Figure 5.9: XRD patterns measured at room temperature for the $Y(Fe_{1-x}Mn_x)_3$ compounds.

Figure 5.10: Illustration of the correlation between the phase fraction and the Mn content.

To investigate the possibility and effect of Mn doping for YFe_3 phase a set of samples $Y(Fe_{1-x}Mn_x)_3$ ($x = 0.1, 0.5, 1, 1.5$) was prepared. To ensure the formation of the correct phase, the samples were annealed inside quartz ampules under argon and annealed for 14 days at 1100 °C. However, as with Y_6Fe_{23}, the heat treatment did not affect the phase formation in a significant way. Measured powder diffraction patterns are presented in Fig. 5.9. For the pure sample ($x = 0$) the refined crystal structure – a rhombohedral $PuNi_3$ type lattice with $a = 5.141$ and $c = 24.574$ – matches the previously reported data [29] ($a = 5.137$, $c = 24.61$). On the other hand, Mn doping is unsuccessful, even for a low Mn content. Figure 5.10 illustrates the development of the phase segregation for the Mn-doped samples. In the investigated range $0.1 \geq x \geq 1.5$ a coexistence of three phases is observed. Mn doping strongly increases the fraction of the Y_6Fe_{23} phase. At the same time, the fraction of the YFe_3 phase rapidly becomes negligible and eventually disappears completely. This suggests that the formation of the $Y(Fe_{1-x}Mn_x)_3$, compound belonging to the YFe_3 phase, is not possible. An explanation can be found by comparing the Y-Fe and Y-Mn phase diagrams. While the YFe_3 phase exists, the equivalent YMn_3 phase is absent in the binary Y-Mn phase diagram [30]. This results in strong segregation – both the Y_6Fe_{23} and the YFe_2 phases are formed instead.

5.4 CONCLUSIONS

In this chapter, the effect of substitution of Fe by Mn and Co on the structure, magnetization, T_C and ΔS_m of $Y_6(Fe_{1-x-y}Mn_xCo_x)_{23}$ compounds has been studied.

The results show that $Y_6(Fe_{1-x-y}Mn_xCo_x)_{23}$ ($0 \geq x \geq 0.25$ and $0 \geq y \geq 0.9$) compounds remain in the cubic $Fm\bar{3}m$ structure of Y_6Fe_{23} and form a continuous solid solution over the whole explored range of Mn and Co doping. The Curie temperature and magnetization of these compounds are very sensitive to the Mn concentration, and a small change in Mn concentration can lead to a drastic decrease in T_C. The introduction of AFM Mn seems to alters the ferromagnetic-antiferromagnetic exchange coupling interaction, leading to the observed effects. Co doping allows for a slower increase in T_C and boosts M_s. For a field change of 0–1.5 T, the value of $-\Delta S_m$ shows a wide span with peak value of 1.1 $\mathrm{J\,kg^{-1}\,K^{-1}}$ at 310 K for $x = 0.15$.

The fact that the Curie temperature can be accurately tuned over a wide temperature range by varying the cobalt and manganese contents is the main advantage for potential applications of $Y_6(Fe_{1-x-y}Mn_xCo_x)_{23}$, despite their modest magnetocaloric effect.

In the last part of this chapter, the previously unexplored YFe_3 system was investigated. Manganese was added to form compounds with a wide range of dopant content $0 \geq x \geq 1.5$. XRD results show a disappearance of the intended YFe_3 phase with increasing manganese content. Phase segregation is observed, with YFe_2 and Y_6Fe_{23} as impurity phases.

The present results may provide some clues for searching for novel MCE materials that are worth further exploration.

REFERENCES

[1] K. H. J. Buschow. “Intermetallic compounds of rare-earth and 3d transition metals”. In: *Reports Prog. Phys.* 40.10 (Oct. 1977), pp. 1179–1256. DOI: `10.1088/0034-4885/40/10/002`.

[2] I. Saenko, O. Fabrichnaya, and A. Udovsky. “New Thermodynamic Assessment of the Fe-Y System”. In: *J. Phase Equilibria Diffus.* 38.5 (Oct. 2017), pp. 684–699. DOI: `10.1007/s11669-017-0574-3`.

[3] O. Kubaschewski. *Iron—Binary phase diagrams.* Springer Science & BusinessMedia, 1982.

[4] H. Kirchmayr and C. Poldy. “Magnetism in rare earth—3d intermetallics”. In: *J. Magn. Magn. Mater.* 8.1 (Mar. 1978), pp. 1–42. DOI: `10.1016/0304-8853(78)90073-2`.

[5] J. L. Sánchez Llamazares, P. Álvarez-Alonso, C. F. Sánchez-Valdés, P. J. Ibarra-Gaytán, J. A. Blanco, and P. Gorria. “Investigating the magnetic entropy change in single-phase Y_2Fe_{17} melt-spun ribbons”. In: *Curr. Appl. Phys.* 16.9 (Sept. 2016), pp. 963–968. DOI: `10.1016/j.cap.2016.05.013`.

[6] C. Bechman, K. Narasimhan, W. Wallace, R. Craig, and R. Butera. “Electronic specific heat and high field magnetization studies on the $Y_6(Fe_{1-x}Mn_x)_{23}$ system”. In: *J. Phys. Chem. Solids* 37.2 (Jan. 1976), pp. 245–249. DOI: `10.1016/0022-3697(76)90168-2`.

[7] T. Futakata, M. Yamaguchi, I. Yamamoto, M. Bartashevich, T. Goto, A. Ito, and S. Morimoto. “Magnetic properties of the hydrides of YFe_3-related compounds”. In: *J. Magn. Magn. Mater.* 104-107 (Feb. 1992), pp. 729–730. DOI: `10.1016/0304-8853(92)91005-E`.

[8] D. Wang, L. Ma, Y. B. Guo, and X. Zhou. “Tunable Curie temperature around room temperature and wide temperature span of magnetic entropy change in $(Fe_{1-x}Mn_x)_2Y$ compounds”. In: *Mater. Res. Express* 4.12 (Dec. 2017), p. 126106. DOI: `10.1088/2053-1591/aa9e1f`.

[9] Y. K. Fang, C. W. Chang, C. C. Yeh, H. W. Chang, W. Li, and W. C. Chang. “Microstructure and magnetocaloric effect of melt-spun Y_2Fe_{17} ribbons”. In: *J. Appl. Phys.* 103.7 (Apr. 2008), 07B302. DOI: `10.1063/1.2829031`.

[10] J. Sánchez Llamazares, P. Álvarez-Alonso, C. Sánchez-Valdés, P. Ibarra-Gaytán, J. Blanco, and P. Gorria. “Investigating the magnetic entropy change in single-phase Y_2Fe_{17} melt-spun ribbons”. In: *Curr. Appl. Phys.* 16.9 (Sept. 2016), pp. 963–968. DOI: `10.1016/j.cap.2016.05.013`.

[11] K. Mandal, A. Yan, P. Kerschl, A. Handstein, O. Gutfleisch, and K.-H. Müller. "The study of magnetocaloric effect in R_2Fe_{17} (R = Y, Pr) alloys". In: *J. Phys. D. Appl. Phys.* 37.19 (Oct. 2004), pp. 2628–2631. DOI: `10.1088/0022-3727/37/19/002`.

[12] M. Koide, K. Kakizaki, and K. Kamishima. "Synthesis and magnetic properties of Fe_2W and Fe_2Y hexaferrites". In: *J. Magn. Soc. Japan* 39.4 (2015), pp. 147–150. DOI: `10.3379/msjmag.1506R003`.

[13] N. Moulay, H. Rached, M. Rabah, S. Benalia, D. Rached, A. H. Reshak, N. Benkhettou, and P. Ruterana. "First-principles calculations of the elastic, and electronic properties of YFe_2, $NiFe_2$ and $YNiFe_4$ intermetallic compounds". In: *Comput. Mater. Sci.* 73 (June 2013), pp. 56–64. DOI: `10.1016/j.commatsci.2013.02.010`.

[14] A. Andreev, M. Bartashevich, and V. Vasilkovsky. "Magnetocrystalline anisotropy in Y_6Fe_{23}". In: *J. Less Common Met.* 167.1 (Dec. 1990), pp. 101–106. DOI: `10.1016/0022-5088(90)90293-S`.

[15] J. Chaboy, L. M. Garciá, F. Bartolomé, H. Maruyama, S. Uemura, N. Kawamura, and A. S. Markosayan. "Fe K-edge x-ray magnetic circular dichroism study in R_6Fe_{23} (R=Ho and Y) compounds near compensation temperature". In: *J. Appl. Phys.* 88.1 (July 2000), pp. 336–338. DOI: `10.1063/1.373663`.

[16] R. Coehoorn. "Calculated electronic structure and magnetic properties of Y-Fe compounds". In: *Phys. Rev. B* 39.18 (June 1989), pp. 13072–13085. DOI: `10.1103/PhysRevB.39.13072`.

[17] P. I. Kripyakevich, D. P. Frankevich, and Y. V. Voroshilov. "Compounds with Th_6Mn_{23}-type structures in alloys of the rare-earth metals with manganese and iron". In: *Sov. Powder Metall. Met. Ceram.* 4.11 (Nov. 1965), pp. 915–919. DOI: `10.1007/BF00773697`.

[18] I. Dubenko, S. Granovskiy, E. Gratz, R. Levitin, A. Lindbaum, and A. Markosyan. "Enhanced paramagnetic thermal expansion of the intermetallic compounds $Y_6(Mn_{1-x}Fe_x)_{23}$". In: *J. Magn. Magn. Mater.* 157-158 (May 1996), pp. 629–630. DOI: `10.1016/0304-8853(95)00961-2`.

[19] S. Kilcoyne and M. Telling. "Magnetic order in $Y_6(Mn_{1-x}Fe_x)_{23}$". In: *J. Magn. Magn. Mater.* 140-144 (Feb. 1995), pp. 871–872. DOI: `10.1016/0304-8853(94)00838-8`.

[20] M. Ohta, A. Fujita, K. Fukamichi, E. Matsubara, and H. Takahashi. "Anti-invar behaviour due to spin fluctuations in $Y_6(Mn_{1-x}Fe_x)_{23}$ compounds". In: *J. Phys. Condens. Matter* 14.23 (June 2002), p. 310. DOI: `10.1088/0953-8984/14/23/310`.

[21] G. Hilscher, N. Buis, and J. Franse. "The transition from ferromagnetism to paramagnetism in $Ti(Fe_{1-x}Co_x)$, $Y_6(Fe_{1-x}Mn_x)_{23}$ and the effect of pressure". In: *Phys. B+C* 91 (July 1977), pp. 170–174. DOI: `10.1016/0378-4363(77)90181-4`.

[22] W. J. James, K. Hardman, W. Yelon, and B. Kebe. "Structural and magnetic properties of $Y_6(Fe_{1-x}Mn_x)_{23}$". In: *Le J. Phys. Colloq.* 40.C5 (May 1979), pp. C5–206–C5–208. DOI: `10.1051/jphyscol:1979577`.

[23] A. Bolyachkin, D. Neznakhin, T. Garaeva, A. Andreev, and M. Bartashevich. “Magnetic anisotropy of YFe_3 compound”. In: *J. Magn. Magn. Mater.* 426.March (Mar. 2017), pp. 740–743. DOI: `10.1016/j.jmmm.2016.10.133`.

[24] M. I. Bartashevich, F. Sugaya, M. Yamaguchi, I. Yamamoto, T. Goto, A. Ito, and S. Morimoto. “Magnetic Properties of YFe_3 Hydrides”. In: *Zeitschrift für Phys. Chemie* 179.1-2 (Jan. 1993), pp. 451–456. DOI: `10.1524/zpch.1993.179.Part_1_2.451`.

[25] R. J. Moskaitis and R. A. Butera. “An electronic heat capacity, magnetic and crystallographic study of the $YFe_{3-x}Ni_x$ system”. In: *J. Appl. Phys.* 49.3 (Mar. 1978), pp. 1443–1445. DOI: `10.1063/1.324968`.

[26] K. Buschow. “Hydrogen absorption and its effect on the magnetic properties of rare-earth iron intermetallics”. In: *Solid State Commun.* 19.5 (July 1976), pp. 421–423. DOI: `10.1016/0038-1098(76)91181-9`.

[27] J. D. Bocarsly, E. E. Levin, C. A. Garcia, K. Schwennicke, S. D. Wilson, and R. Seshadri. “A Simple Computational Proxy for Screening Magnetocaloric Compounds”. In: *Chem. Mater.* 29.4 (Feb. 2017), pp. 1613–1622. DOI: `10.1021/acs.chemmater.6b04729`.

[28] B. Banerjee. “On a generalised approach to first and second order magnetic transitions”. In: *Phys. Lett.* 12.1 (Sept. 1964), pp. 16–17. DOI: `10.1016/0031-9163(64)91158-8`.

[29] B. Predel. “Fe-Y (Iron-Yttrium)”. In: *Dy-Er-Fr-Mo.* Berlin/Heidelberg: Springer-Verlag, 1995, pp. 1–3. DOI: `10.1007/10474837_1355`.

[30] A. Palenzona and S. Cirafici. “The Mn-Y (Manganese-Yttrium) system”. In: *J. Phase Equilibria* 12.4 (Aug. 1991), pp. 474–478. DOI: `10.1007/BF02645974`.

6

STRUCTURAL AND MAGNETIC PROPERTIES OF $(\mathrm{FE}_{1-x}\mathrm{NI}_x)_5\mathrm{SN}_3$ SYSTEM

"The lesson here is not to expect anything dramatic."

— Nisio Isin

In this chapter, the Fe_5Sn_3 *binary compound is taken as a starting material with the aim to adjust its properties for magnetocaloric applications by Ni doping. The structural and magnetic properties of* $(Fe_{1-x}Ni_x)_5Sn_3$ *are studied from magnetization, X-ray diffraction experiments and DFT modelling for a wide range of substitutions. The effect of Ni on the transition temperature and the magnetic structure are discussed.*

6.1 INTRODUCTION

One of the potential uses of the magnetocaloric materials is thermomagnetic heat conversion, which would allow the recycling of waste heat (300 to 470 K) into electrical energy [1, 2]. The important feature of the working material for this application is the possibility to adjust its magnetic properties by modifying the elemental composition of the compound. This is due to a necessity to employ layered [3] and composite [4, 5] working materials to cover large temperature ranges. Transition metal alloys have demonstrated suitable behaviour in many cases, as reviewed in [6, 7], and have the added benefit of being cheap, abundant and non-toxic. For these reasons, Fe-Sn based compounds are of interest for an in-depth investigation.

Table 6.1: Structure and magnetic properties of Fe-Sn binary compounds.
Adapted from [8].

Compound	Type	Structure	T_t, K	moment, μ_B/Fe
FeSn	AF	$P6/mmm$	368	1.7
$FeSn_2$	AF	$I4/mcm$	380	1.6
Fe_3Sn	F	$R\bar{3}m$	743	2.3
Fe_3Sn_2	F	$P6_3/mmc$	612	2.2
Fe_5Sn_3	F	$P6_3/mmc$	588	2.1

A detailed characterization of the Fe-Sn system was given in [8, 9]. This system offers several stable phases with ferromagnetic ordering: Fe_3Sn_2 [10] Fe_5Sn_3 [11], Fe_3Sn [12]. Magnetic moments per iron atom are reasonably large and vary from 1.5 μ_B to 2.3 μ_B. Curie temperatures of these alloys however are relatively high, starting at 588 K (Tab. 6.1). Among these phases, Fe_5Sn_3 has the lowest Curie temperature along with a moderate magnetic moment and therefore is of the most interest. Fe_5Sn_3 has a hexagonal Ni_2In-type structure, as depicted in Fig. 6.1, with two distinct Fe sites. This non-stoichiometric phase is also occasionally labelled as $Fe_{2-x}Sn$ or $Fe_{65}Sn_{35}$ [13–15]. The $2a$ and $\sim 2/3$ of the $2d$ positions are occupied by iron atoms, while the $2c$ positions are fully occupied by tin atoms. In order to lower the transition temperature, a dopant element has to be introduced to the composition. As most of the binary Fe-Sn and Ni-Sn phases showed a considerable solubility of the third element, few choices are available for this role [16–18]. Previously, several investigations were carried out on $(Fe,Mn)_5Sn_3$, extensively studying the effect of manganese substitution on magnetocaloric properties of this compound [19, 20]. The authors report that the Curie temperature is easily tunable with the manganese content. The magnetization near room temperature however can be considered rather low, narrowing the operating range to higher temperatures. Reported values of $-\Delta S_M$ reach 1 $J kg^{-1} K^{-1}$ at the transition in an applied field change of 2 T.

In the current work, an assessment of the structural and magnetic properties of Ni-doped Fe_5Sn_3 was performed with the aim to tailor the magnetization and transition temperature to a range suitable for magnetocaloric applications.

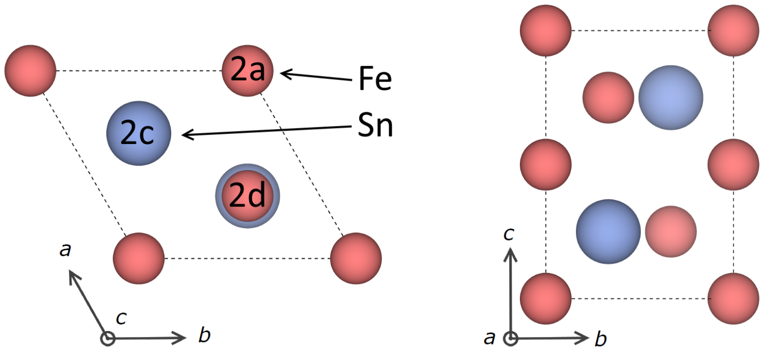

Figure 6.1: Schematic representation of the Fe_5Sn_3 unit cell.

6.2 EXPERIMENTAL AND COMPUTATIONAL DETAILS

SAMPLES were prepared from stoichiometric amounts of high purity elements (iron 99.98%, nickel 99.98% and tin 99.8%). Iron, nickel and tin were combined with the use of an arc-melting furnace under argon atmosphere. Each ingot was melted four times with flipping between each melt to ensure homogeneity. The samples were then sealed in quartz ampoules under a pure argon atmosphere (10 kPa) and annealed for 96 h at 1125 K with further quenching to room temperature in water. XRD was used to investigate structure and composition and for magnetization measurements, SQUID and VSM were utilized as described in 2.3.

For the first-principles calculations (as per section 2.4) a $2 \times 2 \times 1$ supercell was used. The k-space integrations were performed with the 2nd order Methfessel-Paxton method [21] and a smearing width of 0.2 eV. The kinetic energy cutoff was set at 350 eV. The structural degrees of freedom were fully relaxed on a gamma centred k-grid of $9 \times 9 \times 12$. Force convergence tolerance was set at 0.1 meV Å^{-1} and for total energies the tolerance was 1 µeV. The following electrons were treated as valence electrons: $4s$, $3d$ for Ni; $4d$, $5s$, $5p$ for Sn; $3d$ and $4s$ for Fe.

6.3 RESULTS AND DISCUSSION

THE XRD measurements (Fig. 6.2) show that $(Fe_{1-x}Ni_x)_5Sn_3$ crystalizes in the same Ni_2In structure as the base alloy. A few additional peaks are observed due to the superlattice structure of site ordered vacancies, resulting in orthorhombic superlattice reflections from an ordered distribution of vacancies on the $2d$ sites. The superlattice peaks are more pronounced in samples with a high iron content. They were also reported in earlier studies on compounds that share the same structure [20, 22, 23].

The refined lattice parameters show a slow linear decrease as Fe is replaced by Ni (Fig. 6.3). With substitution, the overall volume decreases, along with a moderate decrease in the c/a ratio, indicating a minor deformation of the unit cell. The same is observed for the results obtained from DFT modelling with both values being in good agreement with experimental measurements (Tab. 6.3). The calculation results also suggest a slight

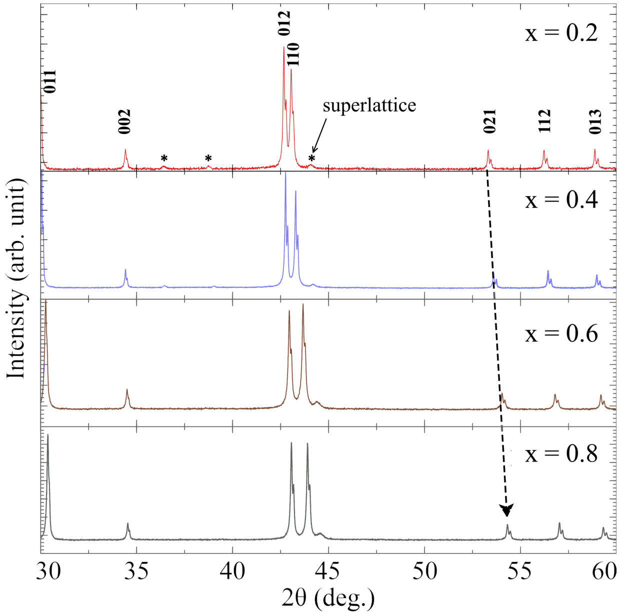

Figure 6.2: XRD patterns measured at room temperature for the $(\mathrm{Fe}_{1-x}\mathrm{Ni}_x)_5\mathrm{Sn}_3$ compounds.

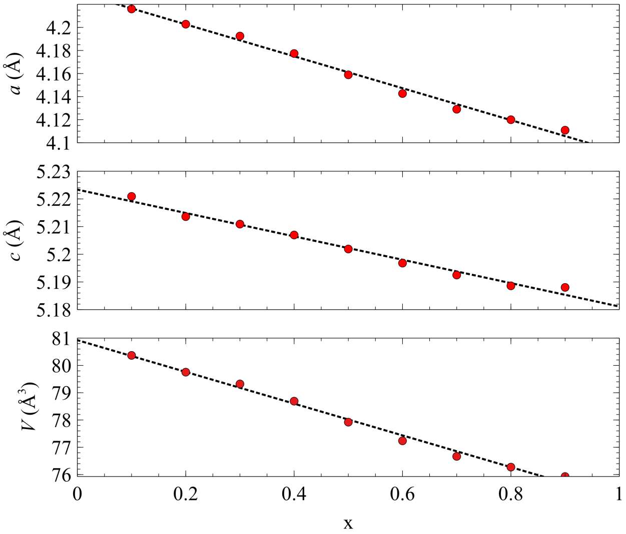

Figure 6.3: Dependence of structural parameters on the Ni content for the $(\mathrm{Fe}_{1-x}\mathrm{Ni}_x)_5\mathrm{Sn}_3$ series. The dotted lines are a guide to the eye.

preference for the 2*a* site for Ni substitution. This coincides with the neutron diffraction results of $(\mathrm{Fe}_{1-x}\mathrm{Mn}_x)_5\mathrm{Sn}_3$ compounds from [15], where Mn atoms show a preference for the 2*a* site for $x < 0.5$ and then occupy both the 2*a* and the 2*d* sites.

Table 6.2: Results of the structural refinement and magnetization measurements for the $(Fe_{1-x}Ni_x)_5Sn_3$ series.

x	a, Å	c, Å	c/a	V, Å^3	χ^2	M_s, A m^2 kg^{-1}	T_t, K
0.1	4.216	5.221	1.238	80.367	3.80	76.8	515
0.2	4.203	5.214	1.241	79.753	4.32	72.4	447
0.3	4.193	5.211	1.243	79.321	3.62	59.2	382
0.4	4.177	5.210	1.246	78.690	3.88	24.8	323
0.5	4.159	5.202	1.251	77.920	4.04	16.7	301
0.6	4.143	5.197	1.254	77.237	4.88	12.7	292
0.7	4.129	5.193	1.258	76.667	3.56	11.4	278
0.8	4.120	5.189	1.259	76.273	4.18	10.3	241
0.9	4.111	5.188	1.262	75.928	4.38	4.9	208

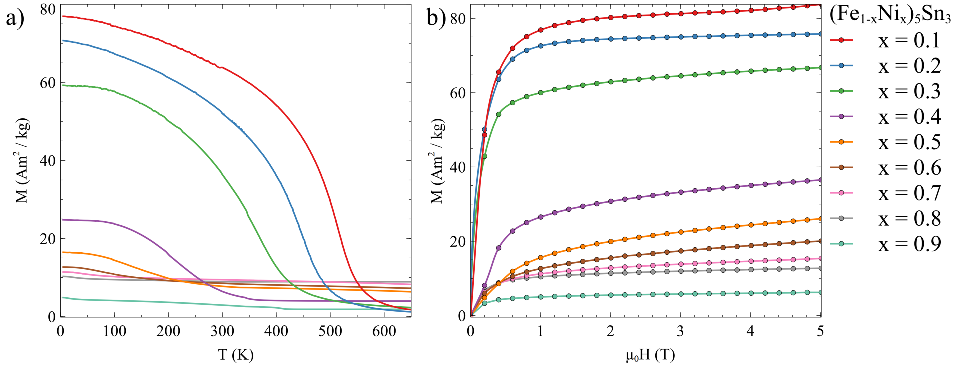

Figure 6.4: Magnetization as a function of temperature at a constant field of 1 T for the $(Fe_{1-x}Ni_x)_5Sn_3$ system (a). Magnetization as a function of applied magnetic field at a constant temperature of 5 K (b).

Substituting Fe for Ni leads to significant changes in magnetization and critical temperature. The isothermal magnetization curves obtained at 5 K under fields up to 5 T are shown in Fig. 6.4(b). For most of the compounds, an applied field of 1 T is sufficient to saturate the magnetization.

Figure 6.4(a) shows the temperature dependence of the magnetization for the $(Fe_{1-x}Ni_x)_5Sn_3$ series. All samples exhibit a second-order transition without hysteresis. The transition temperatures decrease along with the iron content from 515 K in $Fe_{4.5}Ni_{0.5}Sn_3$ down to 208 K in $Fe_{0.5}Ni_{4.5}Sn_3$. Fe-rich compounds ($x \leq 0.3$) have a simple FM behaviour in the whole temperature range. A small amount of Ni doping leads to a gradual decrease in magnetization and once the Ni content is high enough, it drops sharply. The highest obtained value in 1 T is 76.8 A m^2 kg^{-1} for $x = 0.1$. At $x = 0.5$ a room-temperature transition is observed, yet the maximum magnetization for this sample only reaches 16.7 A m^2 kg^{-1}. Compounds with $x > 0.4$, after the initial transition, still maintain some magnetization, which monotonously increases with Ni content. This, along with the slower saturation of the M-H curves for Ni-rich samples, points to the possibility of a noncollinear canted structure for at least one of the two sublattices. The only sample where a second transition to the PM state was observed in the measured temperature range is $x = 0.9$, where it happens around 400 K.

Table 6.3: Structural parameters, total magnetic moments per unit cell and average element- and site-specific moments for $(Fe_{1-x}Ni_x)_5Sn_3$ obtained from DFT calculations.

x	a, Å	c, Å	V, Å^3	μ_{tot}, μ_B	$\langle\mu_{Fe-2d}\rangle, \mu_B$	$\langle\mu_{Fe-2a}\rangle, \mu_B$	$\langle\mu_{Ni}\rangle, \mu_B$
0.08	4.345	5.185	84.775	6.98	2.10	2.55	0.38
0.16	4.343	5.182	84.653	6.50	2.10	2.58	0.36
0.24	4.341	5.180	84.513	6.00	2.10	2.60	0.36
0.32	4.337	5.175	84.308	5.49	2.10	2.64	0.36
0.40	4.331	5.168	83.960	4.87	2.09	2.63	0.33
0.48	4.323	5.158	83.468	4.08	2.03	2.59	0.24
0.56	4.312	5.146	82.870	3.17	1.92	2.55	0.14
0.64	4.304	5.136	82.383	2.39	1.85	-	0.09
0.72	4.287	5.115	81.415	0.99	0.95	-	0.05
0.80	4.275	5.101	80.740	0.01	0.01	-	0.00
0.88	4.269	5.091	80.328	0.00	0.00	-	0.00
0.96	4.261	5.082	79.896	0.00	0.00	-	0.00

DFT calculations provide some insight into how the two magnetic sublattices develop over the range of Ni contents in the FM regime. At first, both have magnetic moments with similar magnitudes (2.5 μ_B on the 2*a* site and 2.1 μ_B on the 2*d* site), which is often the case for binary T-X compounds (where T stands for Mn or Fe and X is a metalloid). During the doping process, Fe atoms maintain their moments and the overall magnetization is decreased due to the increasing amount of Ni carrying lower moment (~0.35 μ_B). At the point when Ni atoms start to occupy both the 2*a* and 2*d* sublattices, the number of Fe-Fe pairs is significantly reduced, thereby suppressing the FM interactions.

6.4 CONCLUSIONS

In summary, $(Fe_{1-x}Ni_x)_5Sn_3$ compounds have been synthesized for the first time and their crystal structures and magnetic properties were investigated. All samples are almost single phase and form in the Ni_2In-type structure over the whole range of substitutions. An increasing Ni content leads to a decrease in lattice parameters and volume. The substitution of Fe for Ni significantly affects the magnetic properties. Both the transition temperature and the magnetization drastically decrease with increasing Ni content. In addition, compounds with more than 30% Ni exhibit a more complicated magnetic behaviour, that likely results from the coexistence of FM and canted spin orientations.

For these Ni-rich samples, further research is necessary to fully describe the magnetic structure with neutron diffraction and subsequent confirmation via DFT modelling.

REFERENCES

[1] H. Jouhara, N. Khordehgah, S. Almahmoud, B. Delpech, A. Chauhan, and S. A. Tassou. "Waste heat recovery technologies and applications". In: *Therm. Sci. Eng. Prog.* 6 (June 2018), pp. 268–289. DOI: `10.1016/j.tsep.2018.04.017`.

[2] M. Trapanese, G. Cipriani, V. Di Dio, V. Franzitta, and A. Viola. "Optimization of a thermomagnetic motor". In: *J. Appl. Phys.* 117.17 (May 2015), 17A750. DOI: `10.1063/1.4919231`.

[3] A. Rowe and A. Tura. "Experimental investigation of a three-material layered active magnetic regenerator". In: *Int. J. Refrig.* 29.8 (Dec. 2006), pp. 1286–1293. DOI: `10.1016/j.ijrefrig.2006.07.012`.

[4] L. Zhou, Y. Tang, Y. Chen, H. Guo, W. Pang, and X. Zhao. "Table-like magnetocaloric effect and large refrigerant capacity of composite magnetic refrigerants based on $LaFe_{11.6}Si_{1.4}H$ alloys". In: *J. Rare Earths* 36.6 (June 2018), pp. 613–618. DOI: `10.1016/j.jre.2018.01.009`.

[5] X. Zhong, X. Shen, H. Mo, D. Jiao, Z. Liu, W. Qiu, H. Zhang, and R. Ramanujan. "Table-like magnetocaloric effect and large refrigerant capacity in $Gd_{65}Mn_{25}Si_{10}$-Gd composite materials for near room temperature refrigeration". In: *Mater. Today Commun.* 14 (Mar. 2018), pp. 22–26. DOI: `10.1016/j.mtcomm.2017.12.005`.

[6] E. Brück, O. Tegus, D. Cam Thanh, N. T. Trung, and K. Buschow. "A review on Mn based materials for magnetic refrigeration: Structure and properties". In: *Int. J. Refrig.* 31.5 (Aug. 2008), pp. 763–770. DOI: `10.1016/j.ijrefrig.2007.11.013`.

[7] J. Lyubina. "Magnetocaloric materials for energy efficient cooling". In: *J. Phys. D. Appl. Phys.* 50.5 (Feb. 2017), p. 053002. DOI: `10.1088/1361-6463/50/5/053002`.

[8] G. Trumpy, E. Both, C. Djéga-Mariadassou, and P. Lecocq. "Mössbauer-Effect Studies of Iron-Tin Alloys". In: *Phys. Rev. B* 2.9 (Nov. 1970), pp. 3477–3490. DOI: `10.1103/PhysRevB.2.3477`.

[9] H. Giefers and M. Nicol. "High pressure X-ray diffraction study of all Fe–Sn intermetallic compounds and one Fe–Sn solid solution". In: *J. Alloys Compd.* 422.1-2 (Sept. 2006), pp. 132–144. DOI: `10.1016/j.jallcom.2005.11.061`.

[10] B. Malaman, D. Fruchart, and G. L. Caer. "Magnetic properties of Fe_3Sn_2 . II. Neutron diffraction study (and Mossbauer effect)". In: *J. Phys. F Met. Phys.* 8.11 (Nov. 1978), pp. 2389–2399. DOI: `10.1088/0305-4608/8/11/022`.

[11] H. Li, B. Zhang, J. Liang, B. Ding, J. Chen, J. Shen, Z. Li, E. Liu, X. Xi, G. Wu, Y. Yao, H. Yang, and W. Wang. "Large anomalous Hall effect in a hexagonal ferromagnetic Fe_5Sn_3 single crystal." In: *Phys. Rev. B* 101.14 (Apr. 2020), p. 140409. DOI: `10.1103/PhysRevB.101.140409`.

[12] B. C. Sales, B. Saparov, M. A. McGuire, D. J. Singh, and D. S. Parker. “Ferromagnetism of Fe_3Sn and Alloys”. In: *Sci. Rep.* 4.1 (May 2015), p. 7024. DOI: `10.1038/srep07024`.

[13] M. Stange, H. Fjellvåg, S. Furuseth, and B. Hauback. “Crystal structure and phase relations for Mn_3Sn_2 and non-stoichiometric $Mn_{2-x}Sn$”. In: *J. Alloys Compd.* 259.1-2 (Aug. 1997), pp. 140–144. DOI: `10.1016/S0925-8388(97)00050-9`.

[14] N. Satya Murthy, R. Begum, B. Srinivasan, and M. Murthy. “Atomic and magnetic structure of $Mn_{1.74}Sn$”. In: *Phys. Lett.* 15.3 (Apr. 1965), pp. 225–227. DOI: `10.1016/0031-9163(65)91219-9`.

[15] H. Shiraishi, T. Hori, N. Ohkubo, and K. Ohoyama. “Magnetic and neutron diffraction study on Ni2In type $(Mn_{1-x}Fe_x)_65Sn_{35}$”. In: *Phys. status solidi* 1.12 (Dec. 2004), pp. 3660–3663. DOI: `10.1002/pssc.200405527`.

[16] Y. Liu, B. Zhou, C. Wu, H. Peng, J. Wang, and X. Su. “Experimental Investigation of the Isothermal Section of the Fe-Mn-Sn System at 723 K”. In: *J. Phase Equilibria Diffus.* 39.3 (June 2018), pp. 280–289. DOI: `10.1007/s11669-018-0630-7`.

[17] T.-T. Huang, S.-W. Lin, C.-M. Chen, P. Y. Chen, and Y.-W. Yen. “Phase Equilibria of the Fe-Ni-Sn Ternary System at 270°C”. In: *J. Electron. Mater.* 45.12 (Dec. 2016), pp. 6208–6213. DOI: `10.1007/s11664-016-4787-8`.

[18] P. Nash and A. Nash. “The Ni-Sn (Nickel-Tin) system”. In: *Bull. Alloy Phase Diagrams* 6.4 (Aug. 1985), pp. 350–359. DOI: `10.1007/BF02880521`.

[19] J. H. Xu, X. M. Liu, Y. H. Xia, W. Y. Yang, H. L. Du, J. B. Yang, Y. Zhang, and Y. C. Yang. “Magnetic properties and magnetocaloric effect of $(Mn_{1-x}Fe_x)_5Sn_3$ ($x = 0λ0.5$) compounds”. In: *J. Appl. Phys.* 113.17 (May 2013), 17A921. DOI: `10.1063/1.4798308`.

[20] A. Dianoux, B. Malaman, and T. Mazet. “Magnetic and magnetocaloric properties of $(Fe_{5-x}Mn_x)Sn_3$.” In: *Solid State Commun.* 260 (July 2017), pp. 40–44. DOI: `10.1016/j.ssc.2017.05.012`.

[21] M. Methfessel and A. T. Paxton. “High-precision sampling for Brillouin-zone integration in metals”. In: *Phys. Rev. B* 40.6 (Aug. 1989), pp. 3616–3621. DOI: `10.1103/PhysRevB.40.3616`.

[22] M. Elding-Pontén, L. Stenberg, A.-K. Larsson, S. Lidin, and K. Ståhl. “Three NiAs–Ni_2In Type Structures in the Mn–Sn System”. In: *J. Solid State Chem.* 129.2 (Mar. 1997), pp. 231–241. DOI: `10.1006/jssc.1996.7231`.

[23] A. Leineweber. “Incommensurately modulated LT"-$Ni_{1+\delta}Sn$ (δ=0.60, 0.63): Rietveld refinement, line-broadening analysis and structural relation with LT- and LT’-$Ni_{1+\delta}Sn$”. In: *J. Solid State Chem.* 182.7 (July 2009), pp. 1846–1855. DOI: `10.1016/j.jssc.2009.04.019`.

SUMMARY

The magnetocaloric effect (MCE) is a thermal response of a magnetic material to a change in an external magnetic field. With the discovery of materials exhibiting a giant magnetocaloric effect in the vicinity of room temperature, several applications of this phenomenon have been proposed. First is the magnetic refrigeration, which can serve as a more eco-friendly alternative to conventional vapour-compression cooling systems. The second is the magnetic energy conversion using thermomagnetic motors and generators. It allows to transfer waste heat – currently an untapped resource – into electricity, therefore, increasing the energy efficiency of various types of industries. The development of devices for these applications facilitated the need for an optimal material to fit all the practical requirements. To this date, only a handful of materials are considered viable for commercial implementation, among which $(Mn,Fe)_2(P,Si)$ alloys, Ni-Mn-based Heusler alloys and $La(Fe,Si)_{13}$ alloys are most prominent.

The goal of this thesis is to identify new promising magnetocaloric materials and improve known material systems using a combination of experimental techniques, *ab initio* modelling and database screening.

Chapter 3 explores the potential of a computer-assisted search for new magnetocaloric systems with high performance. Known magnetocaloric materials were analysed to derive what properties are necessary for a material to have a large magnetocaloric effect that can be successfully used in practical applications. Based on these, several screening parameters are proposed to identify previously unknown systems of interest. Factors such as price, availability and toxicity of candidate materials are taken into consideration along with magnetic properties. To model the latter, density functional theory (DFT) calculations were utilized. The internal field – a normalization of magnetization to volume, serves to compare and select materials with larger magnetic moments. To predict the magnetocaloric performance we introduce a new computational metric – the magneto-elastic response γ_M. It is obtained for each candidate material by modelling the changes in the magnetic moment of the material across a range of deformations. Large values of γ_M are expected for first order materials. This parameter showed a good correlation with the magnetic entropy change ΔS_m measured in known magnetocaloric materials, and can therefore serve as a computational proxy to estimate the performance of the candidate compounds. Several material databases are discussed and evaluated to select the most appropriate ones as the initial source of information about known inorganic materials. To find novel MCE materials, an efficient algorithm is suggested. A step-by-step application of initial screening parameters to sort out unsuitable materials before performing more accurate, computationally heavy assessments allows fast processing of a large number of candidates. The application of this workflow based on the information gathered from two crystallographic databases (Materials Project and Crystallography Open Database) resulted in a list of materials with properties suitable for room temperature refrigeration. This shortlist contains promising compounds ranked by their potential, which can serve as a guide for experimental research.

In **chapter 4** the well known (Mn,Fe)$_2$(P, Si) system is studied. First-principles calculations are used to investigate potential dopants for this materials family. The site preferences and optimal lattice parameters for the substitutions with elements from the 2nd, 3rd and 4th periods are determined. An overview of the changes in magnetization and structural parameters along with doping limits for each type of dopant is compiled. The case of Li doping in which it substitutes Fe atoms on $3g$ site is investigated in more detail. Upon Lithiation the Fe$_2$P unit cell is deformed, lowering the c/a ratio. Li shows clustering behaviour and upon introduction to the Fe$_2$P gradually disrupts the magnetic order. The change in lattice parameters is accompanied by a significant increase in Curie temperature and a loss in the total magnetic moment, which highlights the strong magneto-elastic coupling in this material.

In **chapter 5**, the Fe-Y system is studied with the focus on two previously unexplored compounds: Y(Fe,Mn)$_3$ and Y$_6$(Fe,Mn,Co)$_{23}$. The results show that Y$_6$(Fe$_{1-x-y}$Mn$_x$Co$_x$)$_{23}$ ($0 \geq x \geq 0.25$ and $0 \geq y \geq 0.9$) compounds form a continuous single-phase solid solution over the whole explored range of Mn and Co doping. The Curie temperature and magnetization of these compounds are very sensitive to the Mn concentration, and a small change in Mn content can lead to a drastic decrease in T_C accompanied by a decrease in magnetization, Co doping, on the other hand, allows for a slow increase in T_C and mildly boosts M_s. Despite a modest magnetocaloric effect with $-\Delta S_m$ around $1\,\mathrm{J\,kg^{-1}\,K^{-1}}$ for a field change of 0–1.5 T, the fact that the Curie temperature can be accurately tuned over a wide temperature range by varying the cobalt and manganese contents is an advantage for potential applications. The Y(Fe,Mn)$_3$ system is synthesized for the first time and the viability of Mn doping is assessed. Upon addition of even small amounts of Mn, powder diffraction measurements show the disappearance of the original YFe$_3$ phase and phase segregation in YFe$_2$ and Y$_6$Fe$_{23}$ phases is observed.

In the final chapter (**Chapter 6**) we investigate the structural and magnetic properties of Ni-doped Fe$_5$Sn$_3$ with the aim to adjust its properties for magnetocaloric applications. An increasing Ni content leads to a decrease in lattice parameters and volume. Both the transition temperature and the magnetization drastically decrease as Fe is substituted by Ni. A significant loss in magnetization for compounds with more than 30% Ni appears to be caused by a change in magnetic ordering, likely a coexistence of FM and canted spin orientations.

A search for new functional materials is most effective when multiple experimental and theoretical techniques are utilized. Strategically combining them can greatly hasten the research progress and give a wider outlook on the properties of the materials. This approach helps to cover the drawbacks of each method and capitalize on their stronger points as well as allows acquiring and comparing results from independent sources, thereby improving their credibility.

SAMENVATTING

Het magnetocalorische effect (MCE) is een temperatuurverandering van een magnetisch materiaal als gevolg van een verandering in een extern magnetisch veld. Met de ontdekking van materialen met een reusachtig magnetocalorisch effect in de buurt van kamertemperatuur, zijn er verschillende toepassingen van dit fenomeen voorgesteld. De eerste is magnetische koeling, welke kan fungeren als een meer eco-vriendelijk alternatief voor de conventionele gascompressie koelsystemen. De tweede is de magnetische energieconversie die gebruik maakt van thermomagnetische motoren en generatoren. Dit maakt het mogelijk om restwarmte – momenteel een ongebruikte bron – om te zetten in elektriciteit en daarmee de energie-efficiëntie van verschillende industrieën te verhogen. De ontwikkeling van installaties voor deze toepassingen heeft geleid tot een behoefte aan een optimaal materiaal dat voldoet aan alle praktische voorwaarden. Tot de dag van vandaag is er slechts een handvol materialen dat geschikt wordt geacht voor commerciële toepassingen, waaronder $(Mn,Fe)_2(P, Si)$ verbindingen, op Ni-Mn-gebaseerde Heusler legeringen en $La(Fe,Si)_{13}$ verbindingen de meest prominente zijn.

Het doel van dit proefschrift is om nieuwe veelbelovende magnetocalorische materialen te identificeren en om bestaande materiaalsystemen te verbeteren door het combineren van experimentele technieken, *ab initio* modelleren en het screenen van databases.

Hoofdstuk 3 onderzoekt de mogelijkheden van een computer-geassisteerde zoektocht naar nieuwe goed functionerende magnetocalorische systemen. Bekende magnetocalorische materialen warden geanalyseerd om uit te vinden welke eigenschappen noodzakelijk zijn om een materiaal een groot magnetocalorisch effect te geven dat kan succesvol worden gebruikt in praktische toepassingen. Op basis hiervan zijn verschillende screening parameters voorgesteld om interessante tot hiervoor onbekende systemen te identificeren. Factoren zoals de prijs, de beschikbaarheid en de toxiciteit van de kandidaat-materialen zijn hierin betrokken in combinatie met de magnetische eigenschappen. Om die laatste eigenschappen te modelleren zijn *density functional theory* (DFT) berekeningen gebruikt. Het interne magneetveld – een genormaliseerde magnetisatie, geeft een maat om de geselecteerde materialen met grotere magnetische momenten te selecteren. Om de magnetocalorische eigenschappen te voorspellen introduceren we een nieuwe rekengrootheid – de magnetoelastische responsparameter γ_M. Deze is verkregen door voor elk kandidaat-materiaal de verandering in magnetisch moment van het materiaal over een bereik van vervormingen te berekenen. Grote waarden voor γ_M worden verwacht voor materialen met een eerste-orde faseovergang. Deze parameter vertoont een goede correlatie met de magnetische entropieverandering ΔS_m gemeten voor de bekende magnetocalorische materialen, en kan daarom worden gebruikt als een rekenkundige proxy om de bruikbaarheid van de kandidaat-materialen in te schatten. Verschillende materiaal databases zijn bekeken en geëvalueerd om de meeste geschikten te selecteren als eerste bron van informatie over de bekende anorganische materialen. Om nieuwe MCE materialen te vinden, is een efficiënt algoritme voorgesteld. Een stap-voor-stap toepassing van de initiële screening parameters om ongeschikte materialen uit te filteren gevolgd door het uitvoeren van nauwkeuriger en rekenkundig zwaardere evaluaties, maakt het mogelijk om een groot aantal kandidaten snel te verwerken. Het toepassen van deze workflow die gebaseerd is op informatie die verzameld is uit twee kristallografische databases (*Materials Project* en *Crystallography Open Database*) resulteerde in een lijst van materialen met eigenschappen die geschikt zijn voor koeling bij kamertemperatuur. Deze shortlist bevat veelbelovende verbindingen die zijn gerangschikt naar hun potentie, welke vervolgens kan worden gebruikt als gids voor verder experimenteel onderzoek.

In **hoofdstuk 4** is het bekende $(Mn,Fe)_2(P, Si)$ systeem onderzocht. First-principles berekeningen zijn gebruikt om mogelijke doping elementen voor deze klasse van materialen te onderzoeken. De voorkeur voor een atoompositie en de optimale roosterparameters zijn bepaald voor deze substituties met elementen van de 2e, 3e en 4e perioden. Een overzicht van de veranderingen in de magnetisatie, de structurele parameters en de doping limiet is samengesteld voor elk type doping element. Li doping ter vervanging van Fe atomen op de $3g$ atoompositie site is in meer detail bestudeerd. Bij lithium substitutie wordt de eenheidscel van Fe_2P vervormd, resulterend in een verlaging van de c/a ratio. Li vertoont een clustering gedrag tijdens introductie in Fe_2P waardoor de magnetische ordening geleidelijk wordt verstoord. De verandering in roosterparameters gaat samen met een aanzienlijke toename in de Curie temperatuur en een afname in het totale magnetische moment. Dit gedrag illustreert de sterke magneto-elastische koppeling in dit materiaal.

In **hoofdstuk 5** is het Fe-Y system bestudeerd met een focus op twee niet eerder onderzochte verbindingen: $Y(Fe,Mn)_3$ en $Y_6(Fe,Mn,Co)_{23}$. De resultaten laten zien dat $Y_6(Fe_{1-x-y}Mn_xCo_x)_{23}$ ($0 \geq x \geq 0.25$ en $0 \geq y \geq 0.9$) verbindingen voor het volledige onderzochte bereik van Mn en Co doping een continue vaste legering vormen die uit een enkele fase bestaat. De Curie temperatuur en de magnetisatie van deze verbindingen zijn erg gevoelig voor de Mn concentratie. Een kleine verandering in de Mn concentratie kan leiden tot een drastische afname in T_C en een afname in magnetisatie. Co doping, aan de andere kant, leidt tot een langzame toename in T_C en een milde verhoging van M_s. Ondanks een beperkt magnetocalorisch effect met een $-\Delta S_m$ van ongeveer $1\,\mathrm{J\,kg^{-1}\,K^{-1}}$ voor een veldverandering van $0{-}1.5\,\mathrm{T}$, is het feit dat de Curie temperatuur nauwkeurig kan worden ingesteld over een breed bereik aan temperaturen door de kobalt en mangaan concentratie te variëren een voordeel voor potentiele toepassingen. Het $Y(Fe,Mn)_3$ system is voor het eerst gesynthetiseerd en de mogelijkheden voor Mn doping zijn geëvalueerd. Bij toevoeging van zelfs kleine hoeveelheden Mn laten poeder Röntgendiffractie metingen zien dat de originele YFe_3 fase verdwijnt en dat uitscheidingen van de YFe_2 en Y_6Fe_{23} fasen ontstaan.

In het laatste hoofdstuk (**hoofdstuk 6**) onderzoeken we de structurele en magnetische eigenschappen van Fe_5Sn_3 met Ni doping met het doel om de eigenschappen aan te passen voor magnetocalorische toepassingen. Een toename in Ni concentratie leidt tot een afname in roosterparameters en in volume. Zowel de overgangstemperatuur als de magnetisatie vertonen een drastische afname bij een substitutie van Fe door Ni. Een significante reductie in magnetisatie voor verbindingen met meer dan 30% Ni lijkt te worden veroorzaakt door een verandering in magnetische ordening, waarschijnlijk een co-existentie van ferromagnetisme met gedraaide spin oriëntaties.

Een zoektocht naar nieuwe functionele materialen is het meest effectief wanneer meerdere experimentele en theoretische technieken worden gebruikt. Strategisch combineren van deze technieken kan de voortgang van het onderzoek aanzienlijk versnellen en een breder overzicht van de eigenschappen van de materialen geven. Deze aanpak maakt het mogelijk om de beperkingen van elke methode te compenseren en de sterke punten uit te buiten. Dit maakt het mogelijk om de resultaten onderling te vergelijken en de betrouwbaarheid te verhogen.

A

Appendix A

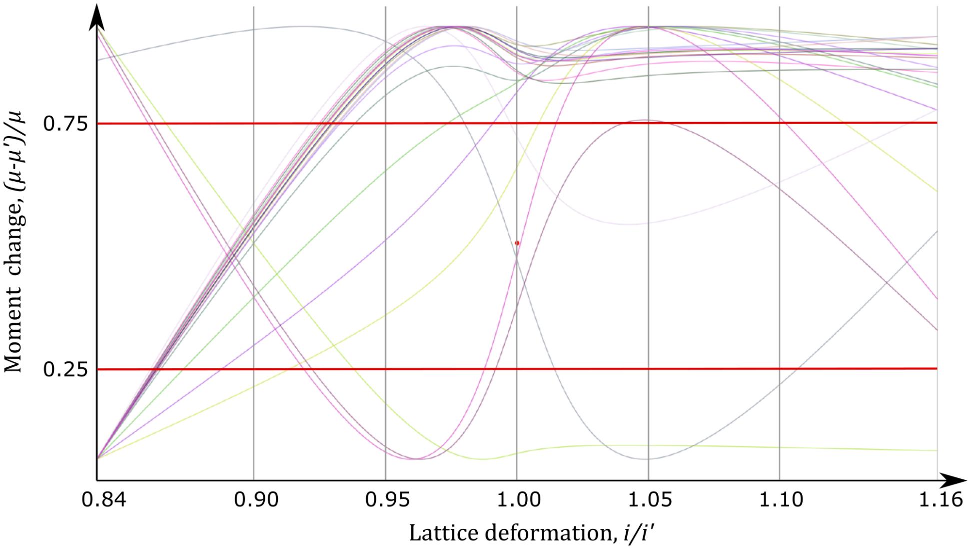

Figure A.1: Typical curves for the magneto-elastic response obtained, based on a random sample from Materials Project database. All the moment changes are scaled by their maximal value. Grey vertical lines indicate the calculated deformations. Red horizontal lines specify 25% and 75% of the maximal moment change values.

Formula 3.7 essentially describes the sharpness of the linear fit to the magnetization vs lattice parameter curve. However, as seen from Fig. 3.5, depending on the deformation range the real dependence may be far from linear. The practical problem is then the choice of the appropriate range and number of deformations to "capture" the step in magnetization we are interested in, with minimal possible computational effort. For the initial screening, in addition to the undeformed structure, four deformations were used for each independent lattice direction (±5% and ±10%). The independent lattice parameters for each symmetry type are listed in table A.1. This means that for each type of deformation we produce a curve of five points. From our tests this gives an optimal balance between the resulting quality and computational effort. If more data points are obtained γ_i can be calculated with higher accuracy.

Table A.1: List of independent lattice parameters for each symmetry type and the total number of calculations necessary to obtain the full γ_M value.

Lattice	Lattice parameters	Total number of calculations
Cubic	a	5
Rhombohedral	a	5
Hexagonal	a, c	9
Tetragonal	a, c	9
Ortorhombic	a, b, c	13
Triclinic	a, b, c	13
Monoclinic	a, b, c	13

In general, we can expect a certain level of smoothness from this curve. So points in-between computed ones are filled in by interpolation. This is done by fitting a Bezier curve of the third order. This step is necessary for further analysis. A set of typical curves for 30 random materials is shown in Fig. A.1. Roughly 3 types of magnetic response have been observed: a steep step between high magnetization and low magnetization plateaus; a slow gradual increase/decrease of magnetization; slanted s-shaped magnetic response centred on the undeformed lattice. To accurately find a linear region in all of these cases a simple algorithm is employed (Fig. A.2).

First, an attempt is made to simply perform a linear fit through all data points. If the fit quality is poor, an attempt is made to single out a smaller sub-region where a better estimate can be made. We expect the presence of maximal and minimal values with a linear step in between and we are only interested in the slope of the said step. In this case, after discarding the top and bottom 25% of the whole vertical range only the part where the linear transition between two states will remain as illustrated in Fig A.1. If this operation produces more than one linear part, the closest one to the undeformed structure is picked. For the curves with saddle-like behaviour, two linear parts will remain, with the only difference being the direction of the slope. In a rare case when fit quality is still unsatisfactory, the remaining segment can be yet again split, now by the position of extrema, again picking the linear segment closest to the undeformed structure. This should guarantee an accurate estimate of the linear part of the curve.

The python code for this calculation can be found below. The first code block describes the main function that is based on the logic shown in Fig. A.2

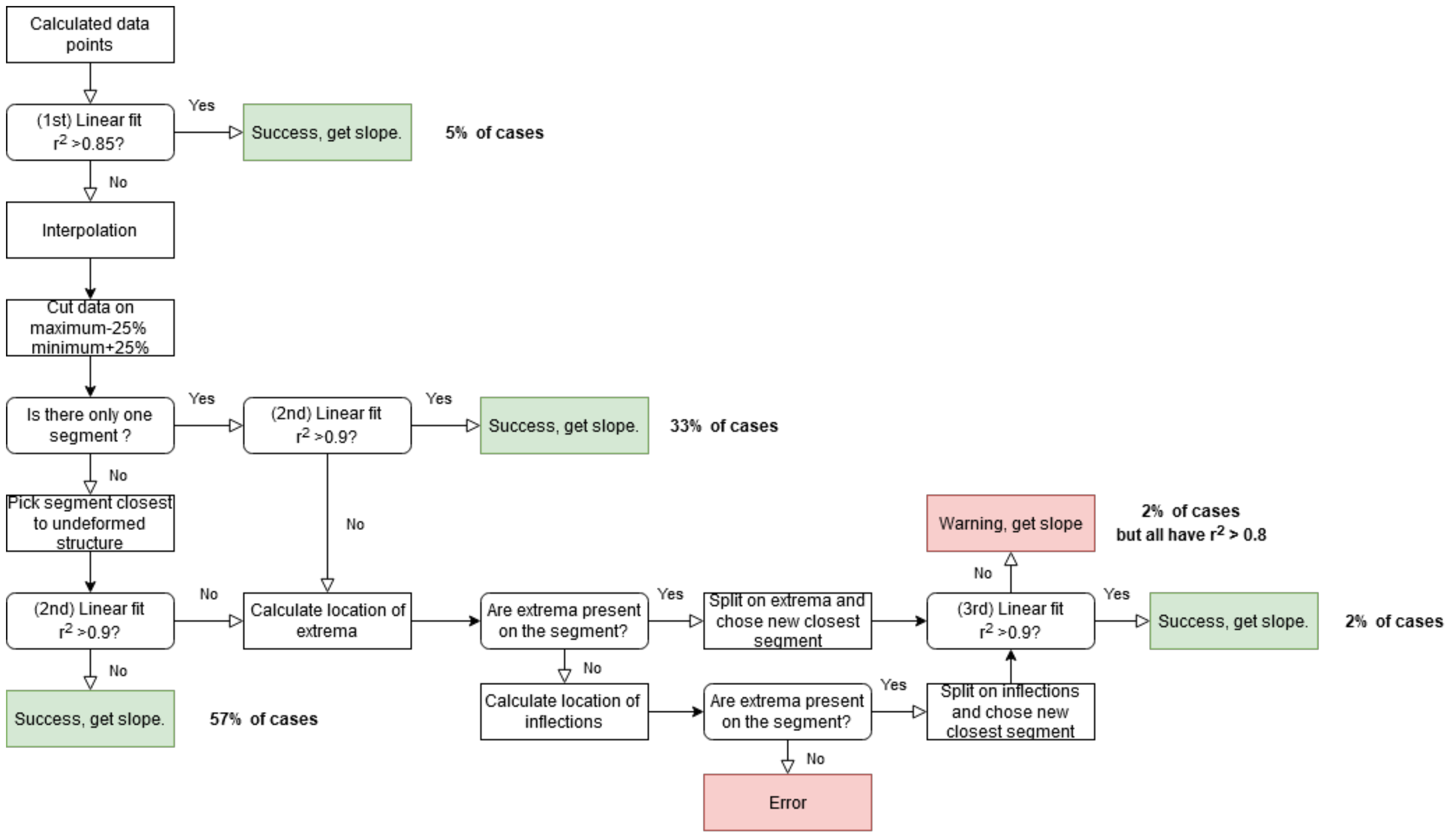

Figure A.2: Block diagram describing the calculation of the magneto-elastic response γ_i.

```
import numpy as np
from scipy import interpolate

def analyze(volumes, moments, volume_undeformed, moment_undeformed):
  """Function returns magneto-elastic response value and fit confidence
 when supplied with a list of magnetic moments and a corresponding list of
   deformed volumes, as well as moment and volume of the undeformed state."
 ""

  # normalizing moments and volumes
  x = list(np.array(volumes) / volume_undeformed)
  y = list(np.array(moments) / moment_undeformed)
  discretization = 50  # how many fitted points to add between measured
 points.
  points = np.column_stack([x, y])

# Case 1 linear fit
  Mag_el, fit_quality, path = linfit(x, y)

  if fit_quality < 0.85:
    # interpolating via a Bezier fit
    path = evaluate_bezier(points, discretization)
    path = np.unique(path, axis=0)
    path_x, path_y = path[:, 0], path[:, 1]
    b = interpolate.InterpolatedUnivariateSpline(path_x, path_y, k=4)
    b2 = interpolate.InterpolatedUnivariateSpline(path_x, path_y, k=5)
    # cutting top and bottom 25% of moment change range
    minimal = np.min(path_y)
    maximal = np.max(path_y)
    span = abs(maximal - minimal)
    mask_size = 0.25 * span
    mask_bottom = minimal + mask_size
    mask_top = maximal - mask_size
    masked_array = np.array(path)
    masked_array[masked_array[:, 1] < mask_bottom] = 0
    masked_array[masked_array[:, 1] > mask_top] = 0
    # gather and count the remaining parts of the curve
    segments_ids = np.where(masked_array[:, 0] != 0)[0]
    segments = np.split(masked_array[segments_ids], np.where(np.diff(
 segments_ids) != 1)[0]+1)
    number_of_segments = len(segments)

    if number_of_segments == 1:
  # Case 2 attempt linear fit on the only segment
      initial_segment = np.array(segments[0])
      Mag_el, fit_quality, path_line = linfit(initial_segment[:, 0],
 initial_segment[:, 1])
    elif number_of_segments > 1:
      # Chose which of the remaining segments is the closest to the
 undeformed structure
      distances_to_undeformed = []
      for seg in segments:
        closest = find_nearest(seg[:, 0], 1)
        distances_to_undeformed.append(closest)
      value_of_closest_one = find_nearest(distances_to_undeformed, 1)
      index_of_closest_one = int(np.where(distances_to_undeformed ==
```

```
 value_of_closest_one)[0])
   initial_segment = np.array(segments[index_of_closest_one])
 # Case 3 attempt linear fit on this segment
   Mag_el, fit_quality, path_line = linfit(initial_segment[:, 0],
 initial_segment[:, 1])

   # if first approach does not work well enough, attempt to further
 find the linear parts
   # break on special points (first try in maximums, then on inflections
 ) and take longest line (so pythogorus between edge points of new even
 smaller segments)
  if fit_quality < 0.9:
   seg_x_max = float(np.max(initial_segment[:, 0]))
   seg_x_min = float(np.min(initial_segment[:, 0]))

   extremum_xs = b.derivative(n=1).roots()
   extremum_ys = b(extremum_xs)
   extrema = np.column_stack((extremum_xs, extremum_ys))

   breakpoints = np.array(extrema)
   breakpoints = breakpoints[(seg_x_min < breakpoints[:, 0]) & (
 breakpoints[:, 0] < seg_x_max)]

   inflect = b2.derivative(n=2).roots()
   inflect_xs = inflect[1:-1]  # remove edge points
   inflect_ys = b(inflect_xs)
   inflections = np.column_stack((inflect_xs, inflect_ys))

   if len(breakpoints) == 0:
    breakpoints = np.array(inflections)
    breakpoints = breakpoints[(seg_x_min < breakpoints[:, 0]) & (
 breakpoints[:, 0] < seg_x_max)]
    if len(breakpoints) == 0:
    print('no special points, but linear fit is bad. Something went
 very wrong')

   split_at = initial_segment[:, 0].searchsorted(breakpoints[:, 0])
   secondary_segments = np.split(initial_segment, split_at)

   # Chose which of the remaining segments is the closest to the
 undeformed structure
   distances_to_undeformed = []
   for seg in secondary_segments:
    closest = find_nearest(seg[:, 0], 1)
    distances_to_undeformed.append(closest)
   value_of_closest_one = find_nearest(distances_to_undeformed, 1)
   index_of_closest_one = int(np.where(distances_to_undeformed ==
 value_of_closest_one)[0])
   # Case 4 attempt linear fit on this segment
   Mag_el, fit_quality_third, path_line = linfit(secondary_segments[
 index_of_closest_one][:, 0], secondary_segments[index_of_closest_one][:,
 1])

return Mag_el, fit_quality
```

For the code above to work additional helper functions shown in the second code block are necessary:

```
def evaluate_bezier(points, n):
  """Interpolation based on a cubic Bezier curve"""
  curves = get_bezier_cubic(points)
  return np.array([fun(t) for fun in curves for t in np.linspace(0, 1, n)])


def get_bezier_cubic(points):
  """Return one cubic curve for each consecutive points"""
  A, B = get_bezier_coef(points)
  return [
    get_cubic(points[i], A[i], B[i], points[i + 1])
    for i in range(len(points) - 1)]


def get_cubic(a, b, c, d):
  """Returns the general Bezier cubic formula given 4 control points"""
  return lambda t: np.power(1 - t, 3) * a + 3 * np.power(1 - t, 2) * t * b
 + 3 * (1 - t) * np.power(t, 2) * c + np.power(t, 3) * d


def get_bezier_coef(points):
  """Find the a & b points for Bezier fit"""
  n = len(points) - 1
  # build coefficents matrix
  C = 4 * np.identity(n)
  np.fill_diagonal(C[1:], 1)
  np.fill_diagonal(C[:, 1:], 1)
  C[0, 0] = 2
  C[n - 1, n - 1] = 7
  C[n - 1, n - 2] = 2
  # build points vector
  P = [2 * (2 * points[i] + points[i + 1]) for i in range(n)]
  P[0] = points[0] + 2 * points[1]
  P[n - 1] = 8 * points[n - 1] + points[n]
  # solve system, find a & b
  A = np.linalg.solve(C, P)
  B = [0] * n
  for i in range(n - 1):
    B[i] = 2 * points[i + 1] - A[i + 1]
  B[n - 1] = (A[n - 1] + points[n]) / 2
  return A, B


def linfit(x, y):
  """Function to perform a linear fit"""
  coeffs = np.polyfit(x, y, 1)
  poly1d_fn = np.poly1d(coeffs)
  yhat = poly1d_fn(x)
  ybar = np.sum(y) / len(y)
  ssreg = np.sum((yhat - ybar) ** 2)
  sstot = np.sum((y - ybar) ** 2)
  R_square = ssreg / sstot     # fit quality
  xp = np.linspace(min(x), max(x), 50)
  yp = poly1d_fn(xp)
  path = np.column_stack((xp, yp))
  return coeffs[0], R_square, path
```

```
def find_nearest(array, value):
    """Function for determining the which curve segment is closest to
   undeformed volume """
    array = np.asarray(array)
    idx = (np.abs(array - value)).argmin()
    return array[idx]
```

B

Appendix B

Table B.1: Element-specific parameters used in DFT calculations.

Element	Valence electroms	Default cutoff energy, (eV)	Initial moment, (μ_B)
Ag	$4d$, $5s$	250	1
Al	$3s$, $3p$	240	1
At	$5d$, $6s$, $6p$	266	1
B	$2s$, $2p$	319	1
Bi	$5d$, $6s$, $6p$	243	1
Br	$4s$, $4p$	216	1
C	$2p$	400	1
Ca	$3s$, $3p$, $4s$	267	1
Cl	$3s$, $3p$	262	1
Co	$3d$, $4s$	268	2
Cr	$3p$, $3d$, $4s$	266	1
Cs	$5s$, $5p$, $6s$	220	1
Cu	$3d$, $4s$	295	1
Dy	$5p$, $5d$, $6s$	156	10
Er	$5p$, $5d$, $6s$	155	10
Eu	$5p$, $6s$	99	1
F	$2s$, $2p$	400	1
Fe	$3d$, $4s$	268	2
Ga	$3d$, $4s$, $4p$	283	1
Gd	$5p$, $5d$, $6s$	154	7
Ge	$3d$, $4s$,$4p$	310	1
H	$1s$	250	1
Hf	$5p$, $5d$, $6s$	220	1
Ho	$5s$, $5p$	154	10
I	$5s$, $5p$	176	1

(continued on next page)

Element	Valence electroms	Default cutoff energy, (eV)	Initial moment, (μ_B)
K	$3s$, $3p$, $4s$	259	1
La	$4d$, $5s$, $5p$, $5d$, $6s$	219	1
Li	$1s$, $2s$	499	1
Lu	$5p$, $5d$, $6s$	155	1
Mg	$3s$	200	1
Mn	$3p$, $3d$, $4s$	270	2
Mo	$4p$, $4d$, $5s$	243	1
N	$2s$, $2p$	400	1
Na	$2p$, $3s$	260	1
Nb	$4s$, $4p$, $4d$, $5s$	293	1
Nd	$5s$, $5p$, $5d$, $6s$	183	3
Ni	$3d$, $4s$	270	1
O	$2s$, $2p$	400	1
P	$3s$, $3p$	255	1
Pd	$4d$, $5s$	251	1
Pm	$5s$, $5p$, $5d$, $6s$	177	2
Pr	$5s$, $5p$, $5d$, $6s$	182	3
Rb	$4s$, $4p$, $4d$, $5s$	220	1
Rh	$4p$, $4d$, $5s$	247	1
Ru	$4p$, $4d$, $5s$	240	1
S	$3s$, $3p$	259	1
Sb	$5s$, $5p$	172	1
Sc	$3s$, $3p$, $3d$, $4s$	223	1
Se	$4s$, $4p$	212	1
Si	$3s$, $3p$	245	1
Sm	$5s$, $5p$, $5d$, $6s$	177	1
Sn	$4d$, $5s$, $5p$	241	1
Sr	$4s$, $4p$, $4d$, $5s$	229	1
Ta	$5p$, $5d$, $6s$	224	1
Tb	$5p$, $5d$, $6s$	156	9
Tc	$4p$, $4d$, $5s$	264	1
Te	$5s$, $5p$	175	1
Ti	$3s$, $3p$, $3d$, $4s$	275	1
Tm	$5p$, $5d$, $6s$	149	7
V	$3p$, $3d$, $4s$	264	1
W	$5s$, $5p$, $5d$, $6s$	223	1
Y	$4s$, $4p$, $4d$, $5s$	203	1
Yb	$5p$, $6s$	113	4
Zn	$3d$, $4s$	277	1
Zr	$4s$, $4p$, $4d$, $5s$	230	1

C

Appendix C

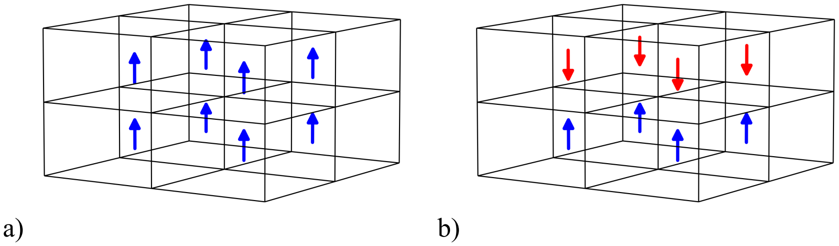

Figure C.1: Schematic diagrams of the FM supercell (a) and the AFM supercell (b) used to obtain the Curie temperatures. Atoms within each unit cell all have the same direction of the magnetic moment. Spin up and spin down cells are represented by blue and red arrows respectively.

Table C.1: Formation energies (in eV) for each possible Wyckoff position for all dopants for Fe_2P. Calculated based on chemical potentials (μ_{dopant}). Lowest negative formation energies are highlighted with **bold**.

	μ_{dopant}	3f	3g	1b	2c	2d	6j	6k
Al	−3.653	0.024	**−0.001**	0.061	0.043	0.073	0.123	0.215
As	−2.936	0.044	0.014	−0.004	**−0.013**	0.057	0.078	0.182
B	−4.220	0.000	−0.002	**−0.038**	−0.033	−0.028	−0.012	−0.028
C	−8.394	0.095	0.098	0.054	0.056	0.046	0.045	0.046
Ca	−2.000	0.082	0.035	0.202	0.144	0.131	0.163	0.130
Co	−4.659	**−0.073**	−0.067	0.017	0.001	−0.008	0.046	−0.002
Cr	−5.992	−0.083	**−0.094**	−0.022	−0.031	−0.024	0.013	−0.024
Cu	−4.099	0.039	0.027	0.113	0.088	0.091	0.142	0.097
F	−1.794	0.041	0.009	0.087	0.044	0.029	0.056	0.029
Ga	0.628	−0.043	−0.070	−0.028	**−0.079**	0.007	0.152	0.098
Ge	−1.235	−0.013	−0.042	−0.035	**−0.048**	0.018	0.257	0.141
K	−1.101	−0.219	**−0.230**	−0.158	−0.167	−0.156	−0.119	−0.156
Li	−1.869	0.356	**−0.334**	3.125	3.125	1.612	1.715	1.608
Mg	−1.575	0.047	0.008	0.131	0.093	0.110	0.150	0.128
N	−5.805	0.023	0.014	0.021	0.003	0.018	−0.008	**−0.009**
Na	−1.310	0.094	0.050	0.199	0.145	0.149	0.170	0.144
Ni	−1.284	**−0.121**	−0.120	−0.033	−0.052	−0.057	−0.005	7.588
S	−2.487	0.048	0.018	−0.016	**−0.023**	0.033	7.620	0.158
Sc	−6.285	0.026	**−0.035**	0.124	0.089	0.086	0.241	0.046
Se	−3.489	0.106	0.078	0.059	0.047	0.253	0.136	0.105
Ti	−5.096	−0.073	**−0.121**	0.008	−0.010	−0.002	7.691	0.001
V	−8.837	−0.026	**−0.027**	0.070	0.057	0.057	0.096	0.066
Zn	2.247	−0.048	**−0.071**	0.000	−0.027	0.003	0.047	0.146

Table C.2: Formation energies (in eV) for each possible Wyckoff position for all dopants for $\mathrm{FeMnP_{0.66}Si_{0.33}}$. Calculated based on chemical potentials (μ_{dopant}). Lowest negative formation energies are highlighted with **bold**.

	μ_{dopant}	3f	3g	1b	2c	2d	6j	6k
Al	−3.653	0.081	0.005	7.999	8.003	7.930	7.930	7.930
As	−2.936	7.901	7.882	**−0.026**	−0.020	7.910	7.910	7.910
B	−4.220	7.936	7.918	**−0.058**	−0.026	−0.024	−0.005	−0.024
C	−8.394	8.052	8.034	8.131	8.135	−0.048	−0.047	**−0.048**
Ca	−2.000	7.875	0.043	7.953	7.957	7.885	7.885	7.885
Co	−4.659	0.052	**−0.049**	8.027	8.031	7.957	7.957	7.957
Cr	−5.992	0.025	**−0.085**	8.064	8.068	7.993	7.993	7.993
Cu	−4.099	0.136	0.117	8.012	8.016	7.942	7.942	7.942
F	−1.794	0.101	0.021	**−0.072**	0.047	0.027	0.045	0.027
Ga	0.628	−0.010	−0.066	−0.071	**−0.049**	7.814	7.814	7.814
Ge	−1.235	−0.009	−0.039	−0.060	**−0.062**	7.864	7.864	7.864
K	−1.101	0.258	0.147	7.928	0.203	7.861	7.861	7.861
Li	−1.869	0.567	**−0.256**	4.146	4.158	2.123	2.356	2.045
Mg	−1.575	7.863	7.845	7.941	7.946	7.873	7.873	7.873
N	−5.805	7.981	7.962	−0.004	0.010	0.019	**−0.020**	−0.019
Na	−1.310	7.856	7.837	7.934	7.938	7.866	7.866	7.866
Ni	−1.284	−0.001	**−0.103**	7.933	7.937	7.866	7.866	7.866
S	−2.487	7.888	7.870	−0.031	**−0.035**	7.898	7.898	7.898
Sc	−6.285	0.131	**−0.026**	8.072	8.076	8.001	8.001	8.001
Se	−3.489	7.916	7.898	7.995	7.999	7.925	7.925	7.925
Ti	−5.096	0.032	**−0.105**	8.039	8.043	7.969	7.969	7.969
V	−8.837	0.105	**−0.009**	8.143	8.147	8.070	8.070	8.070
Zn	2.247	0.017	**−0.063**	7.835	7.839	7.770	7.770	7.770

ACKNOWLEDGEMENTS

My PhD life was an unforgettable experience and I truly enjoyed every moment of it. This was only possible due to the many people who supported me during every step of this journey. I owe gratitude to everyone involved for their help.

First and foremost my heartfelt gratitude goes to my supervisor and promotor prof. dr. Ekkes Brück. His energy and enthusiasm for science greatly inspired and motivated me. His vast knowledge and insight helped me to overcome the challenges I faced and guided my research. He always had time to offer me advice and support despite his incredibly busy agenda and overflowing mailbox. I appreciate his easygoing attitude, optimism and the ideal balance between guiding me and providing me with independence. Thank you for giving me an opportunity to pursue my PhD in such a wonderful environment — the FAME group.

I would like to give my special thanks to my co-promoter Niels van Dijk. His scientific conduct and approach to research motivated me to strive to become a better scientist. You instilled the importance of prudence and care for the details in preparing and presenting my work. I extremely appreciate the comments and suggestions you offered in our discussions as well as your help with my manuscripts. I also enjoyed listening to your various stories and the amusing titbits of information.

I am very thankful to Gilles de Wijs who introduced me to the density functional theory and the VASP code. His patience in teaching me and his cheerful eagerness to face the everchanging challenges we encountered immensely helped me as I embarked into the curious world of the first-principles calculations. I remain astounded by your in-depth knowledge of the computational physics and I am grateful to you for sharing it with me.

My colleagues in the FAME group and Reactor Institute were the sources of help, support and motivation throughout my PhD project. I greatly enjoyed working under the same roof as you.

I warmly thank Anton Lefering. You were always ready to help, both with any misbehaving equipment and any other troubles. Thank you for imparting some of your knowledge about all the various experimental devices. Your kind care was greatly appreciated and I thoroughly enjoyed each and every one of our talks. I thank Ilse van der Kraaij-Quick and Nicole Banga for providing support with all the administrative and organizational matters. Your work made my PhD life easier. I thank Jouke Heringa for helping me with the computer-related stuff on multiple occasions and for some nice and enjoyable talks we shared. I thank Kees Goubitz and Michel Steenvoorden for their assistance in the XRD lab and for sharing useful knowledge on the process of diffraction measurements. I thank Lambert van Eijck and Michel Thijs for their help and guidance during my first attempts at the neutron diffraction measurements. I thank Bert Zwart for preparing countless quartz tubes for me, without which the experimental part of my research would be impossible. I also thank you for the amusing stories that I occasionally had the opportunity to enjoy.

My gratitude also extends to Ben Harrison whose skills were paramount for keeping the arc-melter functional.

I thank Michael Mascheck for helping me and providing me with much-appreciated guidance at the beginning of my PhD project. You made me feel truly welcome at the RID. Your company in Nijmegen for your brief venture into the theoretical modelling, made digesting the first concepts of DFT easier for me. I thank Bowei Huang for giving some insights into the workings of the thermomagnetic motor. I am grateful for being able to share interesting stories and discussions with you and for broadening my understanding of the Chinese culture. I am thankful to Fengqi Zhang, Qi Shen and Anika Kiecana. Your requests stimulated the growth of my knowledge in the computational physics. I profoundly enjoyed our discussions and small talk. I am grateful to Xinmin You, Hamutu, Hanggai, Jun Liu, Jaiwei Lai and Diego Pineda Quijano for offering me useful advice and friendly chats. I thoroughly appreciated and enjoyed working with you and learning from you. I am thankful to my office mates Kasper Versteylen and Maxim Ariens, whose company brightened my day to day routine. I would like to thank my fellow PhDs or postdocs with whom I shared my days at RID: Tomas Verhallen, Niek de Klerk, Violetta Arszelewska, Evgenii Velichko, Alexandros Vasileiadis, Yifan Fu, Viviam Marques Pereira, Lars Bannenberg, Hanan Al-Kutubi, Remco van der Jagt, Tammo Schwietert and anyone who I may have forgotten. I thank Dimitros Besas for the opportunity to take part in the synchrotron measurements in Japan with him and for sharing his knowledge on the subject with me. I greatly enjoyed every part of the trip, and even the endless technical problems we faced now seem like a nice experience.

I would like to thank Casimir Research School and personally Marije Boonstra who was the first to introduce me to TU Delft and facilitate my first meeting with Ekkes. The courses and events organized by the school were invaluable during my PhD.

I extend my sincere gratitude to my former teacher Ludmila Koroleva. Her unwaning thirst for knowledge and the warm support she offered to her students were an inspiration during my masters and bachelors studies.

I thank my friend Alexey Syromyatnikov who provided ever so useful occasional distractions from work and on several occasions gave incredible advice about my research, despite having only a vague idea of the topic.

Finally, I want to thank my family for their love, comfort and unwavering belief in my abilities. I am grateful to my grandfather, as I firmly believe that his educating stories during my childhood were the very first push that eventually caused me to develop my passion for science. I am greatly indebted to my parents. Their counsel and support always help me to become a better version of myself. Their advice always serves as a reliable guide in my endeavours. My achievements were only possible through their encouragement and are dedicated to them.

List of Publications

8. A. Kiecana, I. **Batashev**, A. I. Dugulan, C. Kwakernaak, L. Pieter, F. Zhang, N. van Dijk, and E. Brück. *Effect of Co and Ni doping on the structure, magnetic and magnetocaloric properties of Fe-rich (Mn,Fe)*$_2$*(P,Si) compounds.* in preparation

7. F. Zhang, I. **Batashev**, Q. Shen, Z. Wu, R. I. Smith, G. de Wijs, N. van Dijk, and E. Brück. *Impact of F and S doping on (Mn,Fe)*$_2$*(P,Si) giant magnetocaloric materials.* in preparation

6. F. Zhang, K. Westra, Q. Shen, I. **Batashev**, A. Kiecana, N. van Dijk, and E. Brück. "The second-order magnetic phase transition and magnetocaloric effect in all-d-metal NiCoMnTi-based Heusler alloys". In: *J. Alloys Compd.* 906 (June 2022), p. 164337. DOI: 10.1016/j.jallcom.2022.164337

5. I. **Batashev**, G. A. de Wijs, and E. Brück. *Computational screening of the magnetocaloric materials.* Vol. 30. Handbook of Magnetic Materials, 2021, pp. 1–39. DOI: 10.1016/bs.hmm.2021.10.001

4. I. **Batashev**, G. de Wijs, N. van Dijk, and E. Brück. "Lithiation of the Fe$_2$P-based magnetocaloric materials: A first-principles study". In: *J. Magn. Magn. Mater.* 537 (Nov. 2021), p. 168179. DOI: 10.1016/j.jmmm.2021.168179

3. Q. Shen, I. **Batashev**, F. Zhang, H. Ojiyed, N. van Dijk, and E. Brück. "The antiferromagnetic to ferrimagnetic phase transition in Mn$_2$Sb$_{1-x}$Bi$_x$ compounds". In: *J. Alloys Compd.* 866 (June 2021), p. 158963. DOI: 10.1016/j.jallcom.2021.158963

2. J. Liu, Y. You, I. **Batashev**, Y. Gong, X. You, B. Huang, F. Zhang, X. Miao, F. Xu, N. van Dijk, and E. Brück. "Design of Reversible Low-Field Magnetocaloric Effect at Room Temperature in Hexagonal Mn*MX* Ferromagnets". In: *Phys. Rev. Appl.* 13.5 (May 2020), p. 054003. DOI: 10.1103/PhysRevApplied.13.054003

1. J. Liu, X. You, B. Huang, I. **Batashev**, M. Maschek, Y. Gong, X. Miao, F. Xu, N. van Dijk, and E. Brück. "Reversible low-field magnetocaloric effect in Ni-Mn-In-based Heusler alloys". In: *Phys. Rev. Mater.* 3.8 (Aug. 2019), p. 084409. DOI: 10.1103/PhysRevMaterials.3.084409

CURRICULUM VITÆ

Ivan BATASHEV

Ivan Batashev was born on November 18th, 1993 in Moscow, Russia. In 2015 he obtained his bachelor's degree in Moscow State University in the Faculty of Physics. In the same year, he started the master's program in condensed matter physics at the same university. During these years he worked in the group of prof. dr. Ludmila Koroleva studying the thermoelectric and thermomagnetic properties of the rare-earth manganites. He graduated with honours in 2017.

In February of 2017 during a short visit to TU Delft as a part of the Casimir program, he met prof. dr. Ekkes Brück, this meeting eventually led to the start of his PhD in physics at the Reactor Institute Delft in August of 2017.

At the section of Fundamental Aspects and Materials under the supervision of dr. ir. Niels van Dijk and prof. dr. Ekkes Brück his research was aimed at the discovery and improvement of materials with the giant magnetocaloric effect using a variety of experimental techniques. In the second half of his PhD, under the guidance of dr. ir. Gilles de Wijs, his focus shifted to utilizing the theoretical and computational methods to search for the novel materials and complement the experimental findings of the research group. The results obtained during his PhD are presented in this thesis.